

UNIVERSITÉ DE LIÈGE - FACULTÉ DES SCIENCES APPLIQUÉES

Université
de Liège



FIRE RESISTANCE OF STAINLESS STEEL HOLLOW SECTION COLUMNS

TRAVAIL DE FIN D'ÉTUDES RÉALISÉ EN VUE DE L'OBTENTION DU GRADE DE MASTER INGÉNIEUR
CIVIL DES CONSTRUCTION PAR SCIFO ANTHONY

ANNÉE ACADÉMIQUE 2012-2013

UNIVERSITÉ DE LIÈGE – FACULTÉ DES SCIENCES APPLIQUÉES

MEMBRES DU JURY :

- PROF. JEAN-MARC FRANSSEN
- DR. BARBARA ROSSI
- DR. JEAN-FRANÇOIS DEMONCEAU
- DR. THOMAS GERNAY

Aknowledgements

I would like take this opportunity to thank Ms Barbara Rossi and Mr Thibault Fohn who supervised and mentored my work, for their attention, for all the time they awarded to me and for their advices and explanations which were useful.

My thanks also go to Mr Thomas Gernay and Mr Baptise Cowez, who were always ready to help me.

Then, I would like to thank Mr Jean-Marc Franssen and Mr Jean-François Demonceau for their availability and their explanations.

Finally, I would like to thank my family for their patience during the past-five years.

Abstract

This work aims to improve the knowledge about the behaviour of ferritic stainless steel hollow section columns.

In this work, three fire tests performed at the University of Liege have been used to calibrate finite element models. The three columns have been modelled in SAFIR, a software which is able to solve mechanical and thermal problems using finite elements. In order to obtain a reliable finite element model, several parameters have been studied. The parameters which had the most significant influence on the results were kept, and the others were neglected.

After validating the models against the tests results, those finite element models have been used to generate numerical results. Then, the results have been compared to the bearing capacity calculated at elevated temperatures with the current design standards and other new predictive models.

Finally, the ability of the model proposed by the European code to safely predict the strength of columns at temperature below 600°C has been concluded, as well as the well-adapted shape of the buckling curve proposed by Lopes for temperatures above 600°C. The influence of the enhanced material properties on the bearing capacity of columns has also been highlighted.

Contents

Contents	4
1 State of the art	8
1.1 Material behavior	8
1.1.1 Material properties at high temperature	8
1.1.2 Strength and stiffness reduction factors at elevated temperature	10
1.1.3 Behaviour laws	14
1.1.4 Strength enhancements in cold-formed structural sections	18
1.2 Finite element modelling of ferritic stainless steel cross-section columns	20
1.3 Design rules	21
1.3.1 Design rules at ambient temperature - EC 1993-1-4	21
1.3.2 Design rules at elevated temperature - EC 1993-1-2	23
1.3.3 New predictive models	24
2 Experimental investigation on ferritic stainless steel columns in fire	29
2.1 Specimen geometry	29
2.2 Material behaviour at room temperature	30
2.3 Column tests at room temperature	32
2.4 Column tests in fire	33
2.4.1 Test results - RHS (2500mm) column	33
2.4.2 Test results - SHS (3000mm) column	38
2.4.3 Test results - SHS (2500mm) column	42
2.4.4 Conclusion	46
3 Numerical model of hollow section columns in fire	47
3.1 Geometry and boundary conditions	47
3.1.1 Finite element used in the model	47
3.1.2 Discretization of the column	47
3.1.3 Boundary conditions	49
3.2 Material modelling	50
3.2.1 Mechanical properties	50
3.2.2 Thermal properties	53
3.3 Initial geometrical imperfections	53
3.3.1 Global imperfection	53
3.3.2 Local imperfection	54
3.4 Residual stresses	55
3.5 Temperature development in the cross-section	57
3.6 Loading conditions	62
3.7 Numerical results	63
3.7.1 RHS 2500mm	63
3.7.2 SHS 3000mm	72

3.7.3	SHS 2500mm	74
3.7.4	Conclusions	76
4	Buckling curve - parametric analysis	77
4.1	Comparison of both types of simulation	77
4.1.1	Constant load and varying temperature	77
4.1.2	Varying load and constant temperature	78
4.1.3	Conclusion	79
4.2	Finite element model for the parametric analysis	79
4.2.1	Boundary conditions	79
4.2.2	Geometrical properties	80
4.2.3	Material properties	80
4.2.4	Initial geometrical imperfections	81
4.2.5	Temperature distribution and evolution	81
4.2.6	Cross-section classification	81
4.2.7	Tests results	82
4.2.8	Buckling curves	92
4.2.9	Enhanced material properties	97
4.2.10	Comparison of the models	98
5	Conclusions	106
6	Annexes	108
6.1	Design rules	108
6.2	Experimental investigation on ferritic stainless steel columns in fire	111
6.2.1	Column tests in fire	111
6.3	Numerical model of tubular columns in fire	114
6.3.1	FEMs results	114
	List of Figures	125
	List of Tables	128
	Bibliography	130

Notation

In this paper, several parameters will be used. A description of those parameters is given in the beginning of this document and FIGURE 0.1 illustrates some of them.

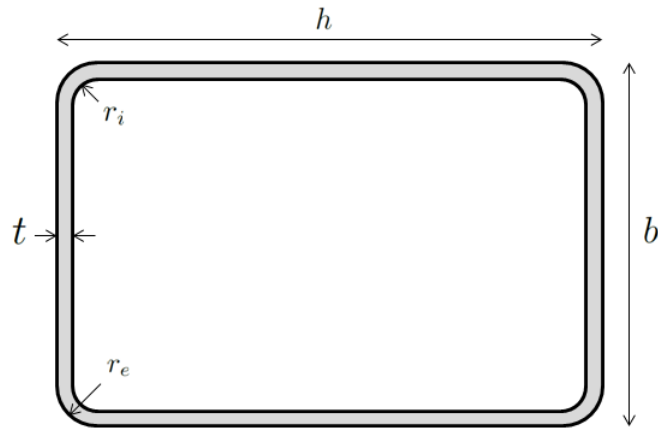


Figure 0.1: Geometrical properties of the cross-section

- b is the width of the cross-section;
- h is the height of the cross-section;
- L is the length of the column;
- t is the thickness of the sheet metal;
- E_0 is the Young modulus at the origin point;
- $f_{y,flat}$ is the 0.2% proof strength in the flat;
- $f_{y,corner}$ is the 0.2% proof strength in the corner region;
- f_u is the ultimate strength;
- r_i is the internal radius of the corner;
- r_e is the external radius of the corner;
- Δ is the global imperfection;
- δ is the local imperfection;
- NG is the number of integration points in each finite element;

- NL is the number of elements across the length of the column;
- Nb is the number of elements across the width of the cross-section;
- Nh is the number of elements across the height of the cross-section;
- Nc is the number of elements across each corner of the cross-section;
- N_{axial} is the load applied axially to the tested element.
- $R - O$ is the abbreviation of the Ramberg-Osgood model recommended by the European code EN 1993-1-2 in order to model the stainless steel material behavior.

Chapter 1

State of the art

In the field of construction, the choice to use a material rather than another is almost always based on the financial aspect. However, in some cases, it is interesting to use a more efficient material in order to obtain a structure which has a better resistance to the external environment and which is lighter. Thus it can be interesting to use stainless steel rather than carbon steel in order to reduce the weight of a structure and to improve its corrosion resistance even if stainless steel is more expensive than carbon steel, due to the alloying elements and the low volume of production. Stainless steels are also characterized by a better retention of strength and stiffness at elevated temperature, in comparison to carbon steel. Moreover, the retention of stiffness is better than that of strength, making the stainless steel elements less prone to buckling at elevated temperature. There are several grades of stainless steel and the most common is the austenitic stainless steel which has the best combination of elevated temperature properties, corrosion resistance and strength. The disadvantage of the austenitic grade is its high nickel content leading to highly variable prices. The advantage of the ferritic grade, which will be studied in this work, is its low nickel content which results in a more cost-stable and economic material compared to austenitic stainless steel. The chemical composition of the ferritic grade 1.4003 is given in TABLE 1.1.

<i>C</i> <i>max.</i>	<i>Si</i> <i>max.</i>	<i>Mn</i> <i>max.</i>	<i>P</i> <i>max.</i>	<i>S</i> <i>max.</i>
0.030	1.00	1.50	0.040	0.015
<i>N</i> <i>max.</i>	<i>Cr</i>	<i>Mo</i>	<i>Ni</i>	<i>Others</i>
0.030	10.5 to 12.5	-	0.30 to 1.00	-

Table 1.1: Chemical composition of stainless steel 1.4003 grade - [% by mass]

1.1 Material behavior

The *stress – strain* curve of stainless steel does not exhibit a sharply defined yield point as that of carbon steel. Thus the 0.2% proof stress (i.e. the stress corresponding to a plastic strain of 0.2%) is used to define the limit between the elastic and the plastic domains. Stainless steels have also a greater ductility and a higher ratio of ultimate-to-yield stress.

1.1.1 Material properties at high temperature

The assessment of the fire resistance of stainless steel structures depends on the ability to predict the material behavior at elevated temperature. The thermal and mechanical parameters to assess the

structural performance in fire are the following, but they do not have the same significance on the fire resistance of the structure.

- Ability to retain the strength and stiffness at elevated temperature
- Unit mass
- Thermal expansion
- Thermal conductivity
- Specific heat
- Emissivity
- Heat transfer coefficient

The thermal and mechanical properties of stainless steel differ from those of carbon steel due to the alloys content of the material. The European code EN 1993-1-2 recommends to use the physical properties presented hereafter for the stainless steel material.

Unit mass of stainless steel is considered to be independent of the steel temperature. The value $\rho_a = 7850 \text{ kg/m}^3$ is recommended by the code.

Thermal expansion is characterized by EQUATION 1.1.

$$\frac{\Delta l}{l} = (16 + 4.79 \times 10^{-3} \theta_a - 1.243 \times 10^{-6} \theta_a^2) \times (\theta_a - 20) 10^{-6} \quad [-] \quad (1.1)$$

where :

- l is the length at 20°C;
- Δl is the temperature induced expansion;
- θ_a is the steel temperature [°C].

Thermal conductivity is determined by EQUATION 1.2.

$$\lambda_a = 14.6 + 1.27 \times 10^{-2} \theta_a \quad [W/mK] \quad (1.2)$$

Specific heat can be determined with EQUATION 1.3.

$$c_a = 450 + 0.8 \times \theta_a - 2.91 \times 10^{-4} \theta_a^2 + 1.34 \times 10^{-7} \theta_a^3 \quad [J/kgK] \quad (1.3)$$

In the thermal numerical model, the values of the emissivity and the heat transfer coefficient used are those recommended by the European codes EN 1993-1-2 and EN 10088-1. They are presented in TABLE 1.2.

ε [-]	α $\frac{W}{m^2K}$
0.4	25

Table 1.2: Thermal material properties

The temperature development in structural stainless steel sections exposed to fire has been studied by Gardner (Gardner and Ng [2006]). The two main parameters in order to determine the temperature development in structural member are the convective heat transfer coefficient and the emissivity. Gardner has proposed new values for the emissivity and heat transfer coefficient of structural stainless steel members exposed to fire. Values of 0.2 (in place of 0.4) for the emissivity and of $35 \frac{W}{m^2K}$ (in place of $25 \frac{W}{m^2K}$) for the heat transfer coefficient are proposed. This new set of value results in average enhancements of 10% of the fire resistance.

However, this study has been performed for austenitic stainless steel. Due to the difference between the chemical composition of austenitic and ferritic grades, these values can not be considered for ferritic stainless steel material. Therefore, the thermal material properties recommended in the European code will be used in this work.

1.1.2 Strength and stiffness reduction factors at elevated temperature

Reductions factors are used to define the material mechanical properties at elevated temperature from the material properties at ambient temperature.

- The stiffness reduction factor ($k_{E,\theta}$) is defined as the elevated temperature initial tangent modulus (E_θ) normalised by the initial tangent modulus at room temperature (E).
- The ultimate strength reduction factor $k_{u,\theta}$ is defined as the elevated temperature ultimate strength ($f_{u,\theta}$) normalised by the room temperature ultimate strength (f_u).
- $k_{y,\theta} = \frac{f_{y,\theta}}{f_y}$ is the reduction factor for the yield strength of steel at the steel temperature θ_a reached at time t . The strength at the steel temperature θ_a for Class 1-3 cross-sections is given by $f_{y,\theta} = f_{0.2p,\theta} + k_{2\%,\theta} (f_{u,\theta} - f_{0.2p,\theta})$. For Class 4 cross-sections, it is given by $f_{y,\theta} = f_{0.2p,\theta}$.

The values recommended by the European code EN 1993-1-2 are presented in TABLE 1.3. The stiffness and strength reduction factors are plotted in FIGURE 1.1, which illustrates that the stainless steel material loses almost all its strength for temperature above 800°C. This scheme shows also that the strength properties decreases faster than the stiffness properties, as mentioned at the beginning of this chapter.

Steel temperature	$k_{E,\theta} = \frac{E_{a,\theta}}{E_a}$	$k_{0.2p} = \frac{f_{0.2p,\theta}}{f_y}$	$k_u = \frac{f_{u,\theta}}{f_u}$	$k_{2\%,\theta}$	$k_{Ect,\theta} = \frac{E_{ct,\theta}}{E_a}$
20	1.00	1.00	1.00	0.37	0.055
100	0.96	1.00	0.94	0.37	0.030
200	0.92	1.00	0.88	0.37	0.030
300	0.88	0.98	0.86	0.37	0.030
400	0.84	0.91	0.83	0.42	0.030
500	0.80	0.80	0.81	0.40	0.030
600	0.76	0.45	0.42	0.45	0.030
700	0.71	0.19	0.21	0.46	0.030
800	0.63	0.13	0.12	0.47	0.030
900	0.45	0.10	0.11	0.47	0.030
1000	0.20	0.07	0.09	0.47	0.030
1100	0.10	0.035	0.045	0.47	0.030
1200	0.00	0.00	0.00	0.47	0.030

Table 1.3: Strength and stiffness reduction factors at elevated temperature - EC1993-1-2 - Annex C

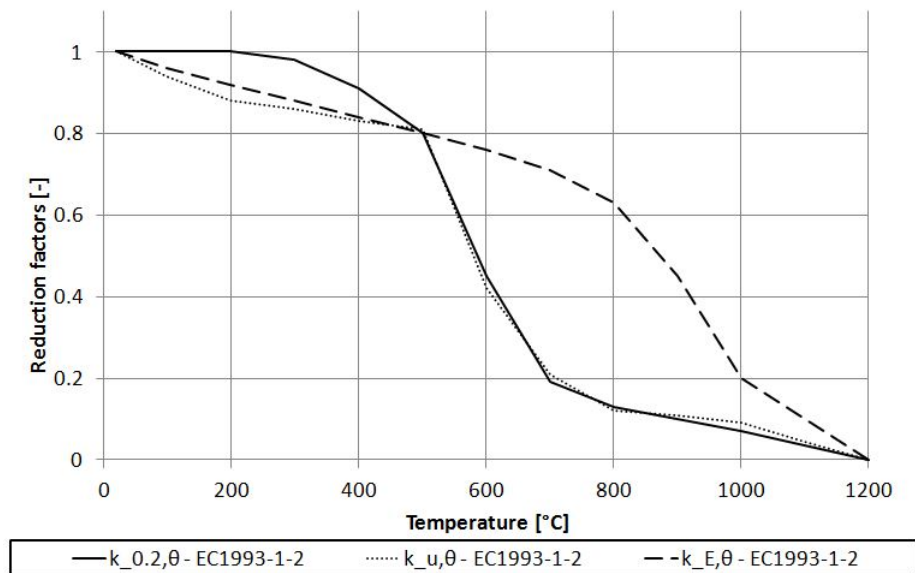
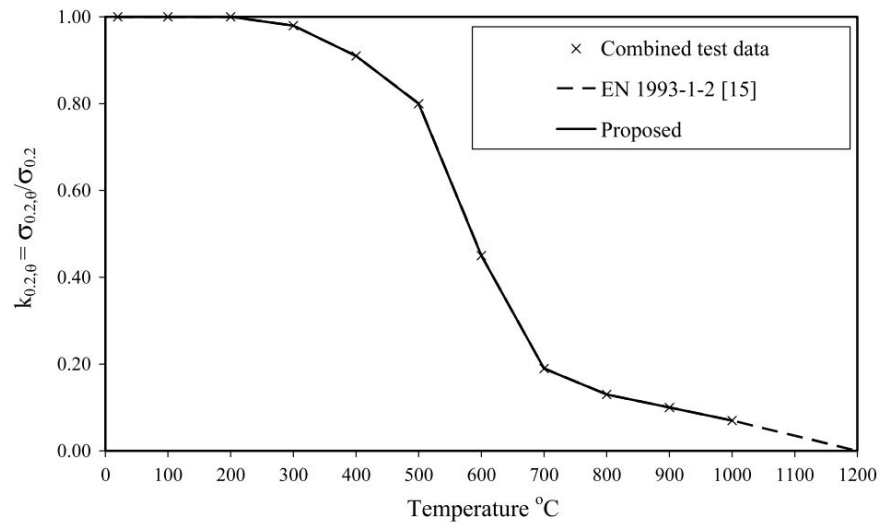


Figure 1.1: Strength and stiffness reduction factors at elevated temperature - EC1993-1-2 - Annex C

Gardner (Gardner et al. [2010]) and Manninen (Manninen and Saynajakangas [2013]) have performed studies and proposed values of elevated temperature reduction factors for the grade 1.4003 of ferritic stainless steel. These proposed values are compared to those provided by the code EN 1993-1-2.

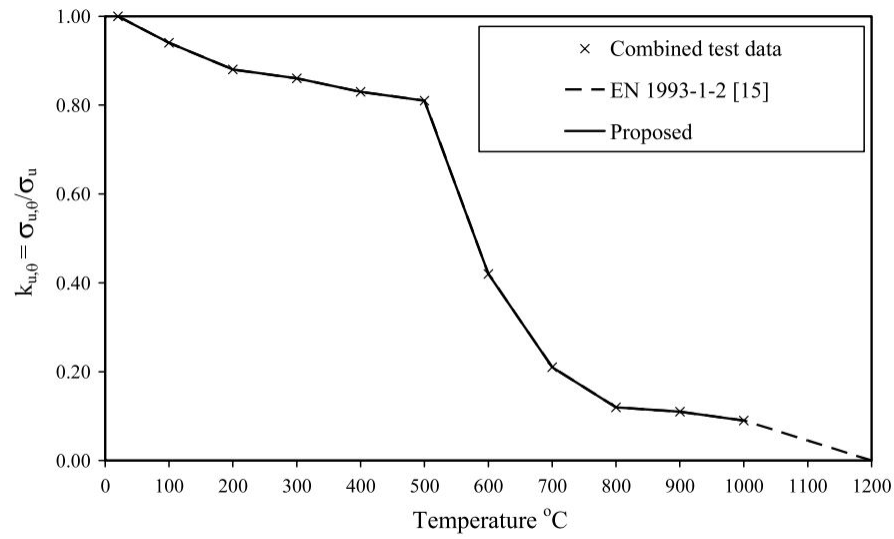
Gardner used all the isothermal and anisothermal tests results available for several stainless steel grades and proposed a new set of elevated temperature reduction factors for each grade. The elevated temperature reduction factors proposed by Gardner for the 1.4003 grade stainless steel are represented in FIGURE 1.2. It shows that the reduction factors proposed by Gardner are the same than those recommended by the European code.

Manninen has performed several isothermal tests. Two tests were performed at each temperature. He obtained somewhat different values of elevated temperature reduction factors than those recommended in the European code (see FIGURE 1.3). This mismatch can be explained by the fact that Manninen used only 2 tests to determine those reduction factors, whereas Gardner used all the available results to determine them.



(i) Grade 1.4003.

(a) $k_{0.2,\theta}$



(i) Grade 1.4003.

(b) $k_{u,\theta}$

Figure 1.2: Strength reduction factors at elevated temperature - Gardner et al. [2010]

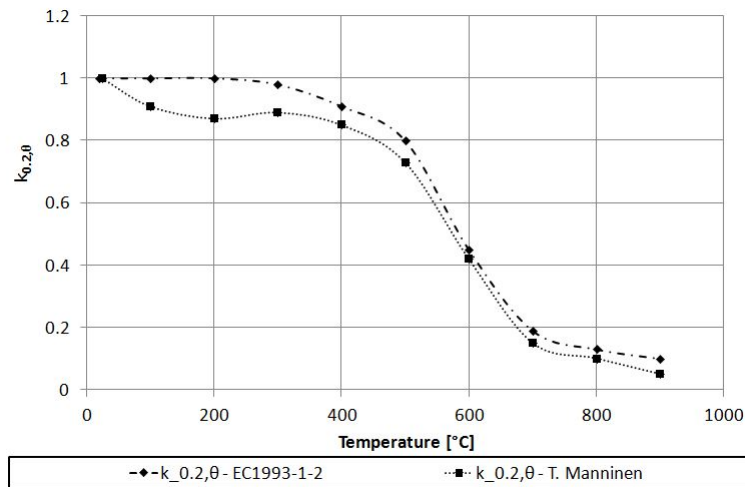
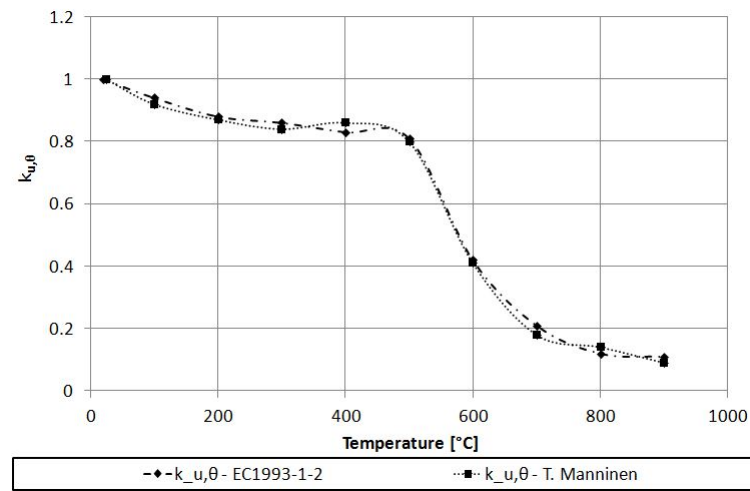
(a) $k_{0.2,\theta}$ (b) $k_{u,\theta}$

Figure 1.3: Strength reduction factors at elevated temperature - Manninen and Saynajakangas [2013]

For the stiffness reduction factors, common reduction factors are used for all the grades, in opposition to the number of grades used to define the strength reduction factors. Two proposals have been done (see FIGURE 1.4) in order to determine the stiffness reduction factor at elevated temperature. The model proposed by Chen and Young (Chen and Young [2006]) is very safe, while that proposed by Ala-Outinen and Oksanen (Ala-Outinen and Oksanen [1997]) is quite close to the curve recommended by the European code EN 1993-1-2. However, due to the uncertainties and scatter of the test data, it is recommended to maintain the use of current codified values.

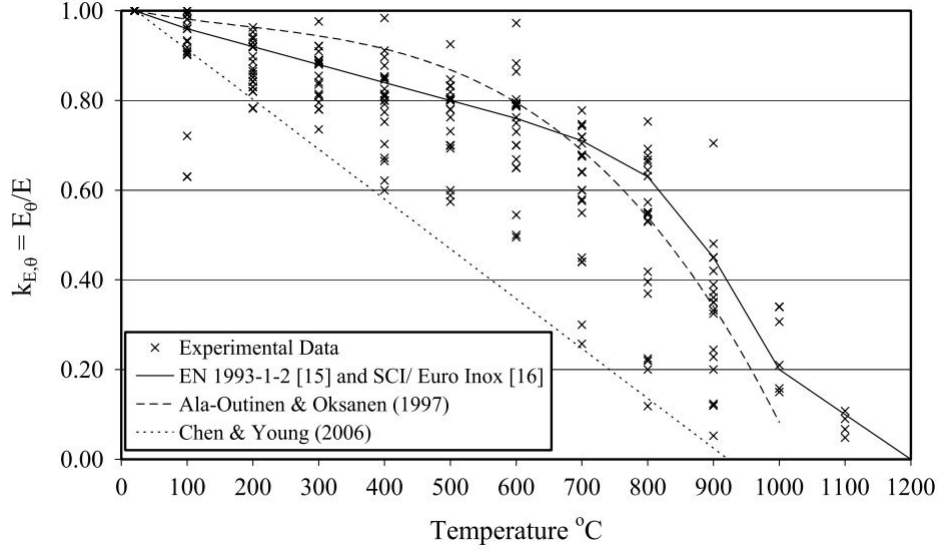
(a) $k_{E,\theta}$

Figure 1.4: Stiffness reduction factors at elevated temperature - Gardner et al. [2010]

In the current work, the elevated temperature reduction factors recommended by the European code EN 1993-1-2 are used.

1.1.3 Behaviour laws

Ramberg-Osgood model

This law is determined by three main parameters (see EQUATION 1.4) : the Young modulus E_0 which determines the slope of the curve at the origin, the 0.2% proof stress $f_{0.2}$ which sets the second point through which the curve passes and the exponent n which determines the degree of non-linearity of the curve.

This model fits well the $\sigma - \varepsilon$ behaviour up to the 0.2% proof stress $f_{0.2}$. Beyond that level, this model over-predicts the stresses. This model has then been modified by Rasmussen (Rasmussen [2003]) and Gardner (Gardner and Ashraf [2006]) in order to fit as well as possible the real stainless steel $\sigma - \varepsilon$ behaviour. Those improvements are presented in the following sections.

$$\varepsilon = \frac{\sigma}{E_0} + 0.002 \left(\frac{\sigma}{f_{0.2}} \right)^n \quad \forall \sigma \quad (1.4)$$

where :

- E_0 is the Young modulus;
- $f_{0.2}$ is the 0.2% proof stress;
- $n = \frac{\ln(20)}{\ln(\frac{f_{0.2}}{f_{0.01}})}$ is a factor of non-linearity;
- σ is the stress;
- ε is the total strain.

Material modeling at room temperature - Eurocode 1993-1-4 - Annex C

Rasmussen (Rasmussen [2003]) proposed a modified compound Ramberg-Osgood model, which contains 2 stages. This model depends on five main parameters : the Young modulus E_0 which determines the slope of the curve at the origin, the 0.2% proof stress $f_{0.2}$ which sets the second point through which the curve passes, the ultimate strength which determines the third point through which passes the curve and the exponents n and m which determine the degree of non-linearity respectively of the first stage and the second stage of the curve.

This model is used in the European code EN 1993-1-4 - Annex C. Thus, for stainless steel at ambient temperature, the stress-strain curve with strain hardening can be modelled using EQUATION 1.5.

$$\varepsilon = \begin{cases} \frac{\sigma}{E_0} + 0.002 \left(\frac{\sigma}{f_{0.2}} \right)^n & \text{for } \sigma \leq f_{0.2} \\ 0.002 + \frac{f_{0.2}}{E_0} + \frac{\sigma - f_{0.2}}{E_{0.2}} + \varepsilon_u \left(\frac{\sigma - f_{0.2}}{f_u - f_{0.2}} \right)^m & \text{for } f_{0.2} < \sigma \leq f_u \end{cases} \quad (1.5)$$

where :

- E_0 is the Young modulus;
- $E_{0.2} = \frac{E_0}{1 + 0.002n \left(\frac{E_0}{f_{0.2}} \right)}$ is the tangent modulus corresponding to a plastic strain of 0.2%;
- $f_{0.2}$ is the 0.2% proof stress;
- f_u is the ultimate strength;
- $\varepsilon_u = 1 - \frac{f_{0.2}}{f_u}$ but $\leq A^1$
- $n = \frac{\ln(20)}{\ln\left(\frac{f_{0.2}}{f_{0.01}}\right)}$ is a factor of non-linearity for the first stage;
- $m = 1 + 3.5 \frac{f_{0.2}}{f_u}$ is a factor of non-linearity for the second stage;

Material modeling at room temperature - Modified compound Ramberg-Osgood proposed by Gardner and Ashraf

A modified compound Ramberg-Osgood expression has been proposed by Gardner and Ashraf (Gardner and Ashraf [2006]). This model proposes to use the 1% proof stress $f_{1.0}$ and the corresponding strain $\varepsilon_{t1.0}$ in place of the ultimate stress f_u and the corresponding strain ε_u . This model is presented hereafter :

$$\varepsilon = \begin{cases} \frac{\sigma}{E} + 0.002 \left(\frac{\sigma}{f_{0.2}} \right)^n & \text{for } \sigma \leq f_{0.2} \\ \varepsilon_{t0.2} + \frac{\sigma - f_{0.2}}{E_{0.2}} + \left(\varepsilon_{t1.0} - \varepsilon_{t0.2} - \frac{\sigma_{1.0} - f_{0.2}}{E_{0.2}} \right) \left(\frac{\sigma - f_{0.2}}{f_{1.0} - f_{0.2}} \right)^{n'_{0.2,1.0}} & \text{for } f_{0.2} < \sigma \leq f_u \end{cases} \quad (1.6)$$

where :

- $f_{0.2}$ is the 0.2% proof stress at ambient temperature;
- $f_{1.0}$ is the stress corresponding to a plastic strain of 1.0% at ambient temperature;
- E_0 is the Young modulus at ambient temperature;

¹A is minimum value of elongation after fracture, according to EN 10088-4.

- $E_{0.2} = \frac{E_0}{1+0.002 n \left(\frac{E_0}{f_{0.2}}\right)}$ is the tangent modulus corresponding to a plastic strain of 0.2% at ambient temperature;
- $\varepsilon_{t0.2}$ is the total strain corresponding to a plastic strain of 0.2% at ambient temperature;
- $\varepsilon_{t1.0}$ is the total strain corresponding to a plastic strain of 1.0% at ambient temperature;
- n is a factor of non-linearity for the first stage of the curve;
- $n'_{0.2;1.0}$ is a factor of non-linearity for the second stage of the curve;

Specific values are proposed for n , $n'_{0.2,1.0}$ and $\frac{f_{1.0}}{f_{0.2}}$ for different stainless steel grades. For the ferritic stainless steel 1.4003 grade, the values proposed by Ashraf are presented in TABLE 1.4.

Grade	n	$n'_{0.2,1.0}$	$\frac{f_{1.0}}{f_{0.2}}$
1.4003	7.3	3.3	1.14

Table 1.4: Compound Ramberg-Osgood's parameters - Ashraf et al. [2006]

Afshan et al. (Afshan et al. [2013b]) proposed a new set of values to model the material law of the ferritic stainless steel 1.4003 grade. The proposed values are provided in TABLE 1.5.

Grade	n	$n'_{0.2,u}$	$n'_{0.2,1.0}$	$\frac{f_{1.0}}{f_{0.2}}$	
1.4003	Tensile	8.4	2.9	—	1.107
	Compressive	6.1	—	3.0	1.107

Table 1.5: Compound Ramberg-Osgood's parameters - Afshan et al. [2013b]

Material modeling at elevated temperature - Eurocode 1993-1-2 - Annex C

FIGURE 1.5 shows the material law proposed by EC1993-1-2 for stainless steel material at elevated temperature. For this model, a number of interdependent coefficients (a , b , c^2 , d^2 and e) have to be determined. This model depends on five reductions factors in order to take the elevated temperature into account. The model is based on the following four parameters which define three points of the curve (the origin, the point corresponding to the 0.2% plastic strain and that associated to the ultimate strain) and the slope at the origin of the curve.

- $f_y = f_{0.2}$ is the 0.2% proof stress at ambient temperature;
- f_u is the ultimate strength at ambient temperature;
- E_0 is the Young modulus at ambient temperature;
- ε_u is the total ultimate strain.

Strain range	Stress σ	Tangent modulus E_t
$\varepsilon \leq \varepsilon_{c,\theta}$	$\frac{E \cdot \varepsilon}{1 + a \cdot \varepsilon^b}$	$\frac{E(1 + a \cdot \varepsilon^b - a \cdot b \cdot \varepsilon^b)}{(1 + a \cdot \varepsilon^b)^2}$
$\varepsilon_{c,\theta} < \varepsilon \leq \varepsilon_{u,\theta}$	$f_{0.2p,\theta} - e + (d/c) \sqrt{c^2 - (\varepsilon_{u,\theta} - \varepsilon)^2}$	$\frac{d + (\varepsilon_{u,\theta} - \varepsilon)}{c \sqrt{c^2 - (\varepsilon_{u,\theta} - \varepsilon)^2}}$
Parameters	$\varepsilon_{c,\theta} = f_{0.2p,\theta}/E_{a,\theta} + 0.002$	
Functions	$a = \frac{E_{a,\theta} \varepsilon_{c,\theta} - f_{0.2p,\theta}}{f_{0.2p,\theta} \varepsilon_{c,\theta}^b} \quad b = \frac{(1 - \varepsilon_{c,\theta} E_{a,\theta} / f_{0.2p,\theta}) E_{a,\theta} \varepsilon_{c,\theta}}{(E_{a,\theta} \varepsilon_{c,\theta} / f_{0.2p,\theta} - 1) f_{0.2p,\theta}}$ $c^2 = (\varepsilon_{u,\theta} - \varepsilon_{c,\theta}) \left(\varepsilon_{u,\theta} - \varepsilon_{c,\theta} + \frac{e}{E_{ct,\theta}} \right) \quad d^2 = e(\varepsilon_{u,\theta} - \varepsilon_{c,\theta}) E_{ct,\theta} + e^2$ $e = \frac{(f_{u,\theta} - f_{0.2p,\theta})^2}{(\varepsilon_{u,\theta} - \varepsilon_{c,\theta}) E_{ct,\theta} - 2(f_{u,\theta} - f_{0.2p,\theta})}$	

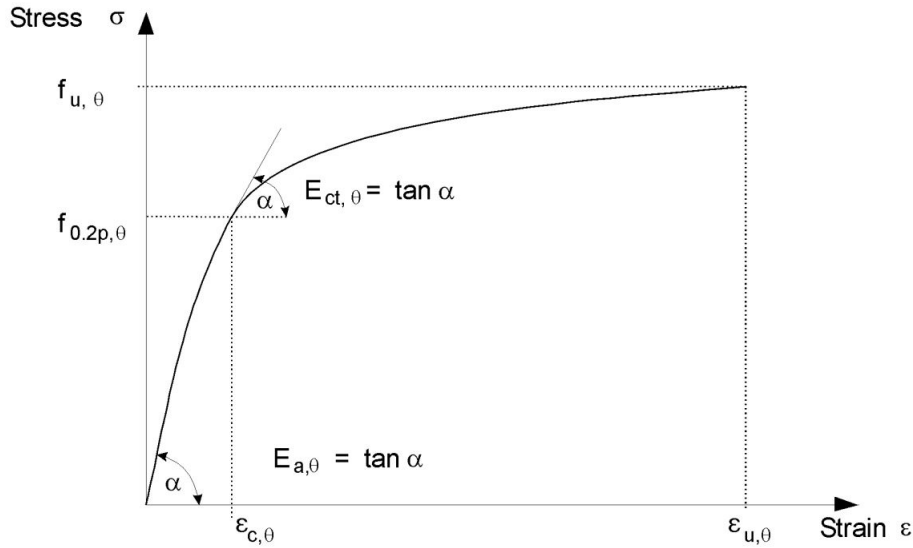


Figure 1.5: Material behavior of stainless steel at elevated temperature - EC1993-1-2-Annex C

Comparison of the models

In this section, the models presented in the previous sections will be compared. The parameters presented in TABLE 1.6 are used in order to compare the behaviour laws.

FIGURE 1.6 illustrates that the models are quite different. The simple Ramberg-Osgood model overrates the strength for plastic deformations higher than 0.2%. The models proposed by the European code at ambient temperature and at elevated temperature pass through the same key points which correspond to the 0.2% plastic strain and the ultimate strain, but between those points, there are small deviations. The modified compound Ramberg-Osgood model proposed by Gardner is closer to the horizontal than the others models, whatever the set of value used.

f_y [MPa]	280
f_u [MPa]	450
$f_{0.01}$ [MPa]	185.7525
E_0 [MPa]	220000
ε_u [-]	0.2
$n'_{0.2,1.0}$ [-]	3.3
$\frac{\sigma_{1.0}}{\sigma_{0.2}}$	1.14

Table 1.6: Parameters used for the comparison

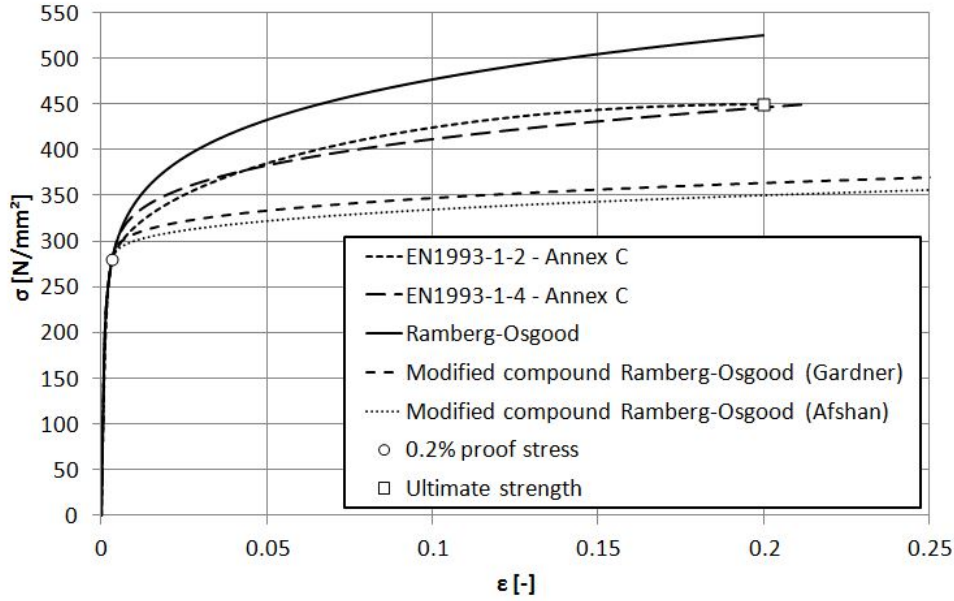


Figure 1.6: Comparison of the models

1.1.4 Strength enhancements in cold-formed structural sections

The rectangular and square hollow section studied in this report are cold-formed. Therefore, plastic strains are induced during both the coiling and the uncoiling of the sheet material and the cross-section forming processes, due to the cold working. Those plastic strains contribute to the overall strength enhancement of the flat faces. For corners of cold-rolled sections, the magnitude of the plastic strains induced during the formation of the corner is much larger than those induced during the previous steps.

A power law model has been proposed (Rossi et al. [2013]). This model provides the strength enhancement of material due to the cold forming of the section.

According to this article, “with the assumption of a linearly varying strain distribution through the material thickness and a bending neutral axis that coincides with the material’s mid thickness, the through thickness averaged plastic strain is given as half of the maximum surface strain. Hence, the through thickness averaged plastic strains for the flat faces $\varepsilon_{f,av}$ and corner regions $\varepsilon_{c,av}$ to be used in the new predictive model are” :

$$\varepsilon_{f,av} = \left[\frac{\frac{t}{2}}{R_{coiling}} \right] + \left[\frac{\frac{t}{2}}{R_f} \right] \quad (1.7)$$

$$\varepsilon_{c,av} = 0.5 \left[\frac{\frac{t}{2}}{R_c} \right] \quad (1.8)$$

where :

- $R_f = \frac{b+h-2t}{\pi}$ is the radius of the circular hollow section prior to forming (see FIGURE 1.7);
- $R_c = r_i + \frac{t}{2}$ is the mean radius of the corners (see FIGURE 1.7) ;
- $R_{coiling} = 450mm$ is the coiling radius².

Finally, the EQUATIONS 1.7 and 1.8, which are proposed to determine the enhancement of the 0.2% proof stress of cold formed structural sections for flats and corner regions are presented here below.

$$\sigma_{0.2,f,pred} = 0.85 [p(\varepsilon_{f,av} + \varepsilon_{t,av})^q] \quad \text{but} \leq \sigma_{u,mill} \quad (1.9)$$

$$\sigma_{0.2,c,pred} = 0.85 [p(\varepsilon_{c,av} + \varepsilon_{t,av})^q] \quad \text{but} \leq \sigma_{u,mill} \quad (1.10)$$

where :

$$p = \frac{\sigma_{0.2,mill}}{\varepsilon_{t,0.2}^q} \quad (1.11)$$

$$q = \frac{\ln\left(\frac{\sigma_{0.2,mill}}{\sigma_{u,mill}}\right)}{\ln\left(\frac{\varepsilon_{t,0.2}}{\varepsilon_u}\right)} \quad (1.12)$$

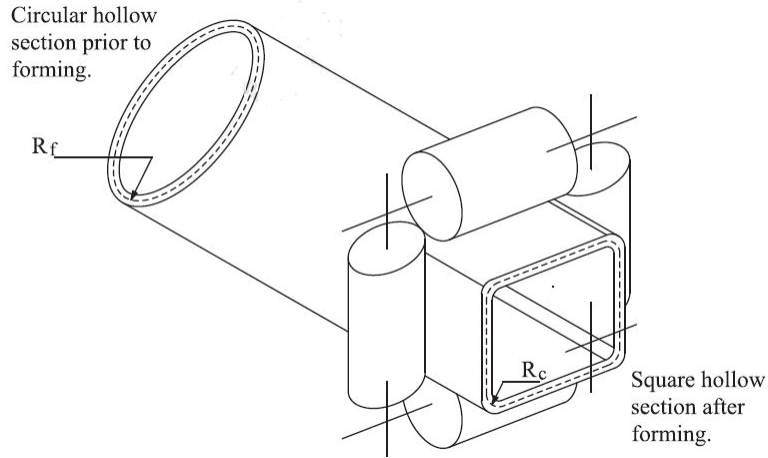


Figure 1.7: Cold-rolling fabrication of tubular box sections - Rossi et al. [2013]

It is important to notice that, according to Gardner (Gardner, 2012), “if the strength enhancements associated with section forming are utilised in design, then the 0.2% proof strength reduction factors for 800 °C and above should be reduced by 20% in relation to those used for sheet material (i.e. $k_{0.2}$ for cold-formed material = $0.8 \times k_{0.2,\theta}$ for sheet material)”.

²Average coil radius recommended (Rossi et al. [2013])

1.2 Finite element modelling of ferritic stainless steel cross-section columns

Several studies have been performed on the finite element modelling of structural ferritic stainless steel cross-section in order to predict the fire resistance of those columns. In this section, the main properties of each developed numerical model are summarized.

Uppfeldt's article (Uppfeldt et al. [2008]) goes over the finite element modeling of columns made of stainless steel grade EN 1.4301 Class 4 square hollow sections. This research has been performed in order to investigate the effect of local buckling. Therefore short columns were used (slenderness smaller than 0.2) in order to avoid global flexural buckling. The finite element model was validated against 6 tests. Finite elements used are four-node elements with six degree of freedom per node. Based on the results obtained from the mesh sensitivity study, an element size of $b/6$ was chosen, where b is the side width. This mesh corresponds to an element size of $25mm$. In order to take into account the strength enhancement of the material due to the amount of cold-working, the FORMULA 1.13, due to Ashraf (Ashraf [2006]), is used to predict the yield strength increase of cold-formed corner regions. This material property is extended up to $2t$ beyond the curved portions of the cross-section, as illustrated in FIGURE 1.8. After performing a sensitivity analysis in order to evaluate the influence of geometrical imperfections on the bearing capacity of the column, only the measured local imperfections were used to model the columns, and the global imperfections were ignored. Similarly the residual stresses were not used to model the columns, due to the little influence on the bearing capacity of the columns.

$$\sigma_{0.2,corner} = \frac{1.881 \sigma_{0.2,virgin\ sheet}}{\left(\frac{r_i}{t}\right)^{0.194}} \quad (1.13)$$

Ashraf (Ashraf et al. [2006]) has performed a finite element modeling of structural stainless steel cross-section and has compared the numerical results to 136 stub columns obtained from 8 different testing programmes. Those tests involve 4 different grades and 6 different cross-sections (Angles, Channels, Lipped channels, I sections, SHS and RHS). The modified Ramberg-Osgood model proposed by Gardner and Ashraf, which is described in SECTION 1.1.3, was used. The parameters n , $n'_{0.2,1.0}$ and $\frac{\sigma_{1.0}}{\sigma_{0.2}}$ used were obtained from coupon test results and have been provided in TABLE 1.4. The modelling of corner material is the same than in Uppfeldt's article and is given by EQUATION 1.13. It was extended up to $2t$ beyond the corner for roll-formed sections. However, the parameters n , $n'_{0.2,1.0}$ and $\frac{\sigma_{1.0}}{\sigma_{0.2}}$ were not known for corner material, and the values used were the same than those used for flat material. At both ends of the columns, all degrees of freedom were fixed except the vertical displacement at the loaded end. After a comparison which has shown that there was no significant difference between the results obtained with the two different shells, it has been chosen to use 9-nodes finite element, because it requires less time to converge to a solution. The column's initial geometrical imperfections is modelled using a deformed shape obtained from elastic buckling analysis. The first eigenmode is used with an amplitude given by EQUATION 1.14. Bending residual stresses are ignored if the material properties used in the finite element model are taken from the coupons cut from the finished cross-section. Thermal residual stresses are ignored too because it has a insignificant effect on the bearing load of the column.

$$w_0 = 0.023 \left(\frac{\sigma_{0.2}}{\sigma_{cr}} \right) t \quad (1.14)$$

where :

- w_0 is the amplitude of the initial local geometrical imperfection;
- $\sigma_{0.2}$ is the 0.2% proof stress;
- σ_{cr} is the elastic critical buckling stress;

- t is the thickness of the plate.

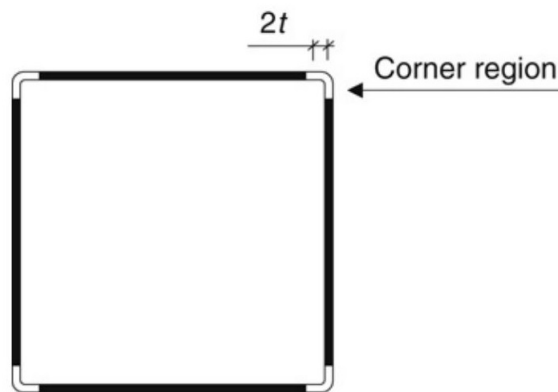


Figure 1.8: Corner regions - Uppfeldt, 2008

Afshan, Gardner and Baddoo write a paper talking about the buckling response of ferritic stainless steel columns at elevated temperatures (Afshan et al. [2013a]). The numerical model developed is validated against nine austenitic and three ferritic³ stainless steel column tests. The studied cross-sections are rectangular and square hollow sections. Four-nodes doubly curved shell element were used for the structural model, while D4S elements were used for the thermal model. Measured geometrical properties were used. The modified compound Ramberg-Osgood material model defined in SECTION 1.1.3 was used to predict the stress-strain response continuously. A uniform strength enhancement, due to the section cold-working, was introduced in corner regions, with an extension of $2t$ beyond the corner radius. This corner material properties had been measured and those measured values were used. For temperatures of 800°C and above, the k_y reduction factor was reduced by 20%. The analysis procedure was made of three steps. The first step did consist in a linear elastic buckling analysis to determine the buckling mode shapes to use. The second step was the heat transfer analysis to obtain the temperature development in the columns and finally the third step made of a mechanical loading to the top of the column which was maintained constant and a thermal loading according to the ISO-834 heating curve. Imperfection shapes used were those of the lowest global and local buckling modes obtained though the linear elastic eigenvalue buckling analysis. Measured amplitudes were used for global imperfections and the amplitude given by EQUATION 1.14 was used for local imperfections.

All tests were performed on columns with a free ends, in order to let the structural members free to expand against the applied load.

In that paper, failure temperatures have been obtained, but nothing is said about the failure mode shape obtained numerically. Conversely, in the present work, the actual test conditions will be modelled in order to represent the real behaviour of the column during the fire test.

1.3 Design rules

In the following sections, the design rules recommended by the European code will be presented for both ambient and elevated temperatures. Then, new predictive models will be presented.

1.3.1 Design rules at ambient temperature - EC 1993-1-4

According to EC1993-1-4, the design buckling resistance of a compression member with a Class 1, 2 or 3 cross section at ambient temperature is determined from :

³The same than that used to calibrate the finite element model in this work.

$$N_{b,Rd} = \frac{\chi A f_y}{\gamma_{M,0}} \quad (1.15)$$

where :

χ is the reduction factor for flexural buckling :

$$\chi = \frac{1}{\varphi + \sqrt{\varphi^2 - \bar{\lambda}^2}} \quad (1.16)$$

with

$$\varphi = \frac{1}{2} [1 + \alpha (\bar{\lambda} - \bar{\lambda}_0) + \bar{\lambda}^2] \quad (1.17)$$

The non-dimensional slenderness $\bar{\lambda}$ is given by :

$$\bar{\lambda} = \sqrt{\frac{A f_y}{N_{cr}}} \quad (1.18)$$

where :

- α is an imperfection factor
- N_{cr} is the elastic critical force for the relevant buckling mode based on the gross cross sectional properties
- $\bar{\lambda}_0$ is the limiting slenderness

For hollow sections submitted to flexural buckling, the values of α and $\bar{\lambda}_0$ are those shown in TABLE 1.7

α	λ_0
0.49	0.40

Table 1.7: Values of α and $\bar{\lambda}_0$ for flexural buckling

The reduction factor in order to determine the effective widths in Class 4 cross-sections is given in EN1993-1-4 as follows, for cold formed internal elements :

$$\rho = \frac{0.772}{\bar{\lambda}_p} - \frac{0.125}{\bar{\lambda}_p^2} \text{ but } \leq 1 \quad (1.19)$$

where $\bar{\lambda}_p$ is the element slenderness defined as :

$$\bar{\lambda}_p = \frac{\bar{b}}{28.4 \varepsilon \sqrt{k_\sigma}} \quad (1.20)$$

where :

- t is the thickness
- k_σ is the buckling factor corresponding to the stress rasion ψ and boundary conditions from TABLE 4.1 or TABLE 4.2 in EN1993-1-5.
- \bar{b} is the flat element width for webs of RHS ($h - 2t$ can conservatively be taken)
- ε is the material factor : $\varepsilon = \left[\frac{235}{f_y} \frac{E}{210000} \right]^{0.5}$ at ambient temperature

1.3.2 Design rules at elevated temperature - EC 1993-1-2

According to EC1993-1-2, the design buckling resistance at time t of a compression member with a Class 1, 2 or 3 cross section with a uniform temperature θ_a is determined from :

$$N_{b,fi,t,Rd} = \frac{\chi_{fi} A k_{y,\theta} f_y}{\gamma_{M,fi}} \quad (1.21)$$

where :

- χ_{fi} is the reduction factor for flexural buckling in the fire design situation;
- $k_{y,\theta} = \frac{f_{y,\theta}}{f_y}$ is the reduction factor for the yield strength of steel at the steel temperature θ_a reached at time t . The strength at the steel temperature θ_a for Class 1-3 cross-sections is given by $f_{y,\theta} = f_{0.2p,\theta} + k_{2\%,\theta} (f_{u,\theta} - f_{0.2p,\theta})$. For Class 4 cross-sections, it is given by $f_{y,\theta} = f_{0.2p,\theta}$.

$$\chi_{fi} = \frac{1}{\varphi_\theta + \sqrt{\varphi_\theta^2 - \bar{\lambda}_\theta^2}} \quad (1.22)$$

with

$$\varphi_\theta = \frac{1}{2} [1 + \alpha \bar{\lambda}_\theta + \bar{\lambda}_\theta^2] \quad (1.23)$$

where :

$$\alpha = 0.65 \sqrt{\frac{235}{f_y}} \quad (1.24)$$

The non-dimensional slenderness $\bar{\lambda}_\theta$ for the temperature θ_a , is given by :

$$\bar{\lambda}_\theta = \bar{\lambda} \left[\frac{k_{y,\theta}}{k_{E,\theta}} \right]^{0.5} \quad (1.25)$$

According to the informative Annex E of EN1993-1-2, the resistance of compression members with a Class 4 cross-section should be verified with the equations given in this section, considering the effective section area (A_{eff}) instead of the gross cross-section (A) and with $f_{y,\theta} = f_{0.2p,\theta}$.

The reduction factor used in order to determine the effective widths in Class 4 cross-sections at elevated temperature is determined using the formulas provided by the European code EN 1993-1-5.

For internal compression elements, the reduction factor ρ is determined using FORMULA 1.26.

$$\rho = \frac{\bar{\lambda}_p - 0.055 (3 + \psi)}{\bar{\lambda}_p^2} \leq 1 \quad (1.26)$$

where $\bar{\lambda}_p$ is determined with the same formula than at ambient temperature (FORMULA 1.20).

In order to take into account the influences due to increasing temperature, the material factor at elevated temperature is calculated with FORMULA 1.27, where f_y is the yield strength at 20°C, .

$$\varepsilon = 0.85 \left[\frac{235}{f_y} \right]^{0.5} \quad (1.27)$$

1.3.3 New predictive models

Stainless steel structures present a relationship between strength and stiffness which is favorable, and it makes stainless steel less prone to buckling in fire. It is due to the fact that reduction factor of the strength decreases faster than that of stiffness with increasing temperature. Therefore, several proposals have been made in order to take this favorable effect into account.

Modification of the material factor expression

FORMULA 1.27 is used in the European code EN 1993-1-2 to determine the material factor ε at elevated temperature. This material factor is used to determine the cross-section classification and the effective cross-section of Class 4 cross-section. The general expression of this material factor for carbon steel at elevated temperature is that presented in FORMULA 1.28. FIGURE 1.9 illustrates the evolution of the ratio $\left(\frac{k_{E,\theta}}{k_{y,\theta}}\right)^{0.5}$ in regard with the temperature. When the value of this ratio is less than unity, it means that the reduction factor associated to the Young modulus decreases faster than the reduction factor associated to the strength. Therefore, if the ratio $\left(\frac{k_{E,\theta}}{k_{y,\theta}}\right)^{0.5}$ is less than unity, it means that the element has a greater susceptibility to buckling. Hence, the 0.85 factor used in EN1993-1-2 is justified for carbon steel, but it is not for stainless steel because the ratio $\left(\frac{k_{E,\theta}}{k_{y,\theta}}\right)^{0.5}$ increases continuously with the temperature for stainless steel. Therefore, as written in Gardner's article, for stainless steel, "the cross-section classification based on room temperature design remains acceptable for fire design".

$$\varepsilon = \left[\left(\frac{235}{f_y} \right) \left(\frac{k_{E,\theta}}{k_{y,\theta}} \right) \right]^{0.5} \quad (1.28)$$

Considering the difference between carbon steel and stainless steel, several proposals have been made in order to take this into account. The proposal are presented in the following sections, in which only the modified parameters and formulas are mentioned.

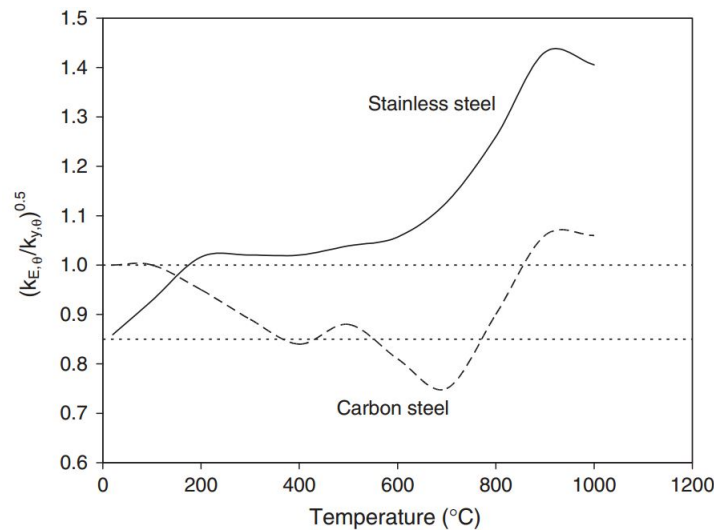


Figure 1.9: Variation of the modification factor $\left(\frac{k_{E,\theta}}{k_{y,\theta}}\right)^{0.5}$ with temperature

Design rules at elevated temperature proposed by Euro Inox (Euro-Inox [2002])

The first proposal is made by Euro Inox and consists in changing the way to calculate the material factor. FORMULA 1.29 is proposed in order to determine the cross-section classification of stainless

steel material at room temperature. The rest of the design rules was not modified in this proposal.

$$\varepsilon = \left[\frac{235}{f_y} \frac{E}{210000} \right]^{0.5} \quad (1.29)$$

Design rules at elevated temperature proposed by CTICM/CSM (CTICM/CSM [2005])

CTICM/CMS has proposed a number of modifications to the EN 1993-1-2 approach :

- Firstly, it proposes to determine the cross-section classification at room temperature, according to FORMULA 1.29.
- Secondly, it is proposed to use the room temperature buckling curves from EN 1993-1-4, given in FORMULA 1.30, where α is the imperfection factor and $\bar{\lambda}_0$ is the limiting slenderness. The values of these parameters are that presented in TABLE 1.8.

$$\varphi_\theta = \frac{1}{2} [1 + \alpha (\bar{\lambda}_\theta - \bar{\lambda}_0) + \bar{\lambda}_\theta^2] \quad (1.30)$$

α	$\bar{\lambda}_0$
0.49	0.20

Table 1.8: Values of α and $\bar{\lambda}_0$ for flexural buckling - CTICM/CSM

- Finally, it is proposed that for all classes of cross-section, the strength reduction factor is based upon the elevated temperature 0.2% proof strength.

The full proposed design model is given in Annex.

Design rules at elevated temperature proposed by Ng and Gardner (Ng and Gardner [2007])

Due to the better retention of stiffness than strength of stainless steel, it would be interesting to take into account this ratio between the stiffness reduction factor and the strength reduction factor at elevated temperature. Thus, Ng and Gardner proposed to determine the cross-section classification of stainless steel elements at elevated temperature, with FORMULA 1.31⁴. It means that the true variation of stiffness and strength at elevated temperature is used in cross-section classification and in the determination of the effective cross-section properties.

The modifications proposed by Ng and Gardner are presented hereafter :

- Firstly, Ng and Gardner proposes to determine the cross-section classification at elevated temperature according to FORMULA 1.31.
- Secondly, they propose to adopt the general form of the room temperature buckling curves, given by FORMULA 1.30, with the parameters given in TABLE 1.9.

α	$\bar{\lambda}_0$
0.55	0.20

Table 1.9: Values of α and $\bar{\lambda}_0$ for flexural buckling - Ng and Gardner

⁴In order to never over-predict the resistance of an element, it is recommended that cross-section that are Class 4 at room temperature cannot be promoted beyond Class 3 at elevated temperature.

- Finally, they propose to use the strength reduction factor based on the 2% strain limit ($k_{2,\theta}$) for Class 1 and 2 cross-section and the 0.2% plastic strain limit ($k_{0.2p,\theta}$) for Class 3 and 4 cross-sections in order to determine the fire resistance of cross-section and members.

$$\varepsilon_{\theta} = \left[\frac{235}{f_y} \frac{E}{210000} \frac{k_{E,\theta}}{k_{y,\theta}} \right]^{0.5} \quad (1.31)$$

where

- $k_{y,\theta} = k_{2,\theta}$ for Class 1 and 2 cross section at room temperature;
- $k_{y,\theta} = k_{0.2p,\theta}$ for Class 3 and 4 cross section at room temperature;

The full proposed design model is given in Annex.

Design rules at elevated temperature proposed by Uppfeldt et al. (Uppfeldt et al. [2008])

Uppfeldt has proposed a new design rule which takes into account the temperature-dependent relationship between strength and stiffness for the local buckling as well as for global buckling. He has performed a research which has been done for cold rolled box columns and the material studied was the grade 1.4301 of stainless steel. The proposal made by Uppfeldt to improve the design model for Class 4 cross-sections is presented in the following. It is a design model for elevated temperature which is also valid for ambient temperature.

- Firstly and similarly to the previous design model, the basic form of the buckling curves (EQUATIONS 1.32 and 1.33), the imperfection factor ($\alpha = 0.49$ for hollow sections) and the limiting slenderness ($\bar{\lambda}_0 = 0.4$) given in the European norms EN 1993-1-4 are used.

$$\chi_{fi} = \frac{1}{\varphi_{\theta} + \sqrt{\varphi_{\theta}^2 - \bar{\lambda}_{\theta}^2}} \quad (1.32)$$

$$\varphi_{\theta} = \frac{1}{2} [1 + \alpha (\bar{\lambda}_{\theta} - \bar{\lambda}_{0,\theta}) + \bar{\lambda}_{\theta}^2] \quad (1.33)$$

- Secondly and still similarly to the previous design model, both the local and the global slenderness depend on the temperature. The difference with the previous model is that in this one, the limiting slenderness is also suggested to be temperature dependent (and therefore strength-stiffness ratio dependent) according to EQUATION 1.34.

$$\bar{\lambda}_{0,\theta} = \bar{\lambda}_0 \left[\frac{k_{y,\theta}}{k_{E,\theta}} \right]^{0.5} \quad (1.34)$$

- Thirdly, the strength reduction factor used are the same than in the previous design model : $k_{2,\theta}$ for Class 1 and 2 cross-section and $k_{0.2p,\theta}$ for Class 3 and 4 cross-section.
- Finally, Uppfeldt proposes also to determine the cross-section classification at elevated temperature according to FORMULA 1.31.

The full proposed design model is given in Annex.

Design rules at elevated temperature proposed by Lopes, Vila Real et al. (Lopes et al. [2012])

Lopes and the others performed a research on HE cross-section columns, and several stainless steel grades were studied, including the 1.4003 ferritic grade. The modifications of the design model recommended by the European code EN 1993-1-2 are presented hereafter.

- Firstly, Lopes modified the expression of χ_{fi} by introducing a β factor, which depends on the axis considered (see TABLE 1.10). The new expression is given by FORMULA 1.35.

$$\chi_{fi} = \frac{1}{\varphi_{\theta} + \sqrt{\varphi_{\theta}^2 - \beta \bar{\lambda}_{\theta}^2}} \tag{1.35}$$

- Secondly, the expression of φ_{θ} is also modified, according to EQUATION 1.36, where the imperfection factor α considers the different behaviors at high temperature of the different stainless steel grades and is given by FORMULA 1.37. α is described by Lopes as a function of the material factor (ε) and the severity factor (η) which depends on the stainless steel grade. TABLES 1.10 and 1.11 give the values of coefficients β and η .

$$\varphi_{\theta} = \frac{1}{2} [1 + \alpha \bar{\lambda}_{\theta} + \beta \bar{\lambda}_{\theta}^2] \tag{1.36}$$

$$\alpha = \eta \varepsilon = \eta \sqrt{\frac{235}{f_y} \frac{E}{210000}} \sqrt{\frac{k_{E,\theta}}{k_{y,\theta}}} \tag{1.37}$$

- Lopes proposes also to determine the cross-section classification at elevated temperature according to FORMULA 1.38.

$$\varepsilon = 0.85 \left(\frac{235}{f_y} \frac{E}{210000} \right) \tag{1.38}$$

	β
Strong axis	1.0
Weak axis	1.5

Table 1.10: Coefficient for determining the reduction factor

	1.4301, 1.4401, 1.4404, 1.4571, 1.4003	1.4462
η	1.3	0.9

Table 1.11: Severity factor for the flexural buckling of stainless steel members in case of fire

To conclude this section, the TABLE 1.12 summarizes the limits of the proposed models. For example, it can be seen that the model proposed by Ng and Gardner and that proposed by Uppfeldt have been calibrated on austenitic stainless steel columns. It can also be seen that the model proposed by Lopes et al. has been proposed for welded I-section columns. The last row of the table gives the type of data used to calibrate the model.

Author	Geometry		Class	Grade	Test/FEM
	Slenderness	Cross-section			
Ng and Gardner	$0.4 \leq \lambda \leq 1.2$	<i>RHS</i> and <i>CHS</i>	1 \rightarrow 4	1.4301	<i>FEM</i>
Uppfeldt et al.	$\lambda \leq 0.1$	<i>SHS</i>	4	1.4301	<i>FEM</i>
Lopes et al.	Variable	<i>HE200A</i> <i>HE280B</i> <i>HE200B</i>	1 \rightarrow 2	Several (including 1.4003)	<i>FEM</i>

Table 1.12: Summary of the new predictive models

Chapter 2

Experimental investigation on ferritic stainless steel columns in fire

A series of tests has been performed in the vertical wall furnace at the Fire Testing Laboratory of the University of Liege in the framework of the RFCS project named Structural Applications of Ferritic Stainless Steels (SAFSS, RFSR-CT-2010-00026). This furnace is certified to the ISO 17025 standard by the Belgian accreditation body BELAC. Three fire tests on square (SHS) and rectangular (RHS) hollow section columns were carried under constant compressive load and subject to the standard ISO fire curve (given in the European code EN 1991-1-2). Identical columns were tested at room temperature in order to fully identify the effects of fire loading. Material coupons extracted from members were used to establish the mechanical properties at room temperature. Note that this description of the fire tests is partially inspired from Tondini et al. [2013].

2.1 Specimen geometry

Two SHS $80 \times 80 \times 3 \text{ mm}$ having nominal lengths of 3000 mm and 2500 mm and a RHS $120 \times 80 \times 3 \text{ mm}$ having a nominal length of 2500 mm were tested. Due to the fact that small variations in the geometry may highly influence the response of thin-walled members, the actual dimensions of the specimens were measured before each test and they are reported in TABLE 2.1.

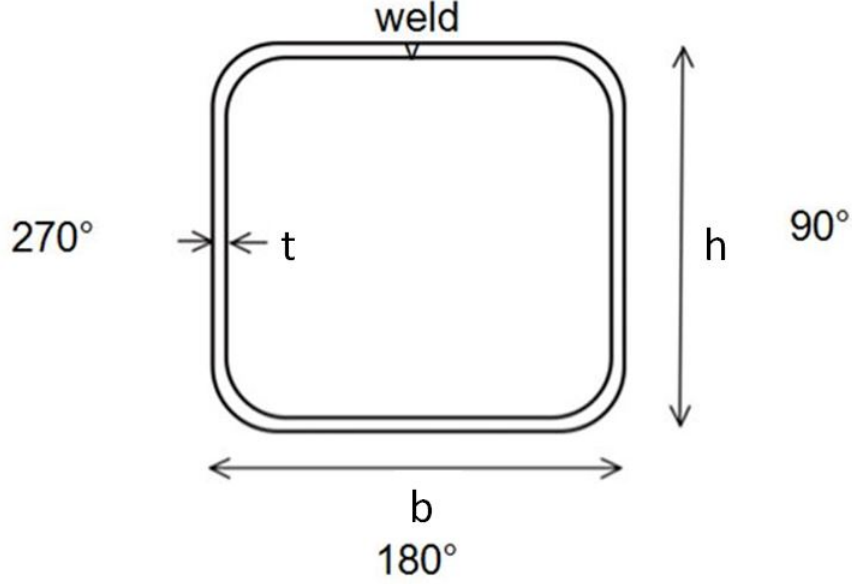


Figure 2.1: Notations for the cross-section dimensions

	C1	C2	C3
Section [mm]	80 × 80 × 3	80 × 80 × 3	120 × 80 × 3
Nominal length [mm]	3000	2500	2500
$t_{av,measured}$ [mm]	2.87	2.82	2.97
$B_{measured}$ [mm]	79.6	79.2	79.4
$H_{measured}$ [mm]	79.2	79.8	119.5
A [cm ²]	8.51	8.38	11.19
Massivity factor [m^{-1}]	360	365	345

Table 2.1: Cross-section dimensions

2.2 Material behaviour at room temperature

The 1.4003 ferritic stainless steel grade was employed. The specimens were supplied by the steelwork company Stalatube and the mill certificates, that present virgin material properties according to EN 10088-2, are provided for both sections (see TABLE 2.2). Tensile tests at room temperature on material coupons cut from the members were also carried out by the steelwork company Aperam in order to establish the true values of the mechanical properties. Coupons were extracted from all the faces except that including welding. The average results of tensile coupon tests are provided in TABLE 2.3. However, the values given in TABLE 2.3 are the conventional properties. Those stresses do not take into account the reduction of the cross-section area during the test. Thus, it under-estimates the stresses into the tested material. The true stresses and strains are determined using FORMULAS 2.1 and 2.2. The measured $\sigma_{true} - \varepsilon_{ln}$ curves for both RHS and SHS are illustrated in FIGURE 2.2 and FIGURE 2.3

$$\sigma_{true} = \sigma_{nom} (1 + \varepsilon_{nom}) \quad (2.1)$$

$$\varepsilon_{ln}^p = \ln(1 + \varepsilon_{nom}) - \frac{\sigma_{true}}{E} \quad (2.2)$$

Section [mm]	80 × 80 × 3	120 × 80 × 3
$\sigma_{0.2}$ [MPa]	336.0	329.0
$\sigma_{1.0}$ [MPa]	360.5	350.0
σ_{ult} [MPa]	484.5	468.0
ε_{ult} [%]	42.5	37

Table 2.2: Mill certificate data (from Stalatube)

Section [mm]	80 × 80 × 3	120 × 80 × 3
$\sigma_{0.2}$ [MPa]	458.7	437.2
$\sigma_{1.0}$ [MPa]	485.8	462.8
σ_{ult} [MPa]	505.4	490.1
ε_{ult} [%]	25.6	24.2
E_0 [MPa]	193	194

Table 2.3: Average tensile coupon tests results (from Aperam)

It is known that plastic deformation due to the manufacturing at ambient temperature results in an increase of the yield stress and a reduction of ductility. Hence, values obtained in TABLE 2.4 are in accord with the expected trend. Face named 180° has undergone more plastic deformations than faces 90° and 270°. Hence, that face has a higher yield stress and a smaller ductility. The face which contains the weld has undergone less plastic deformations than faces 90° and 270°.

Section [mm]	80 × 80 × 3			120 × 80 × 3		
	90°	180°	270°	90°	180°	270°
$\sigma_{0.2}$ [MPa]	439.6	496.2	440.2	411.8	498.2	408.4
$\sigma_{1.0}$ [MPa]	466.8	524.5	466.8	434.7	538.6	433.5
σ_{ult} [MPa]	588.4	577.5	590.5	562.8	552.2	559.0
ε_{ult} [%]	24.2	19.2	25.5	26.1	13.8	25.3
E_0 [MPa]	207646	198089	173496	168971	182585	230930

Table 2.4: True material properties

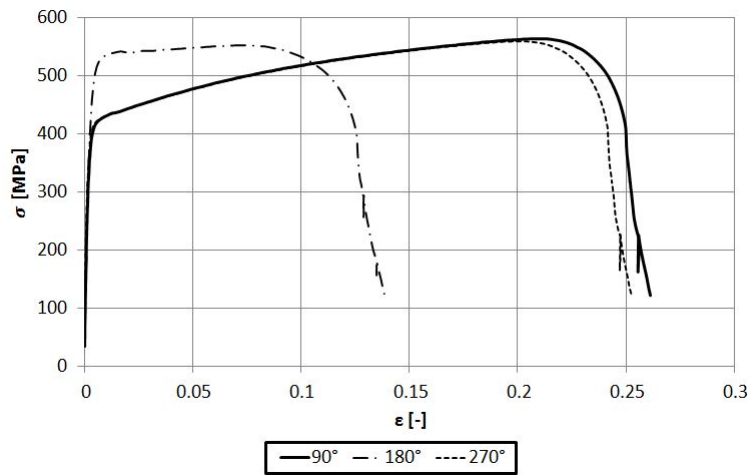


Figure 2.2: $\sigma_{true} - \varepsilon_{ln}$ curve - RHS

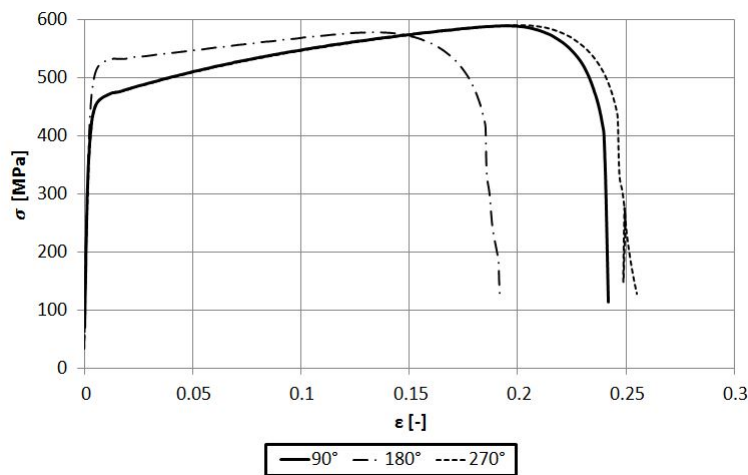


Figure 2.3: $\sigma_{true} - \varepsilon_{ln}$ curve - SHS

2.3 Column tests at room temperature

Tests at ambient temperature have been performed on the same column specimens than those tested at elevated temperature. The boundary conditions were the same than for the fire test (i.e. full restrained rotation at both supports). The loading was displacement-controlled and the transverse displacements in two perpendicular directions were measured.

The three columns failed in the same way, by combination of local buckling and global flexural buckling. Initially, elastic buckling did occur with a mode shape relative to fixed boundary conditions. Then, plastic hinging appeared at midspan and at both column ends.

The recorded displacements have shown that the rectangular hollow section column failed about the weak axis and conversely, the square hollow section columns failed with a combined flexural buckling about the two axes.

The column tests results at ambient temperature are presented in TABLE 2.5.

	SHS 3000mm	SHS 2500mm	RHS 2500mm
Length [mm]	2962.5	2473.5	2475.0
Maximum out-of-straightness amplitude [mm]	$< L/3000$	$< L/2500$	$< L/2500$
Boundary conditions	Fixed	Fixed	Fixed
Ultimate axial capacity [kN]	314.7	343.6	417.9

Table 2.5: Column tests results at ambient temperature

2.4 Column tests in fire

The fire resistance is characterized by the time elapsed between the beginning and the end of heating, or until failure. A column has reached the failure point when there is a rapid rate of increase of vertical and lateral deflection. According to EN1363-1, it is said that a column reached the failure point when both the following criteria have been exceeded :

- vertical contraction of $C = \frac{h}{100}$ [mm]
- rate of vertical contraction of $\frac{dC}{dt} = \frac{3h}{1000} \frac{mm}{min}$

where h is the initial column height in mm .

The test set-up and the loading protocol are available in Annex (SECTION 6.2.1) and are derived from Tondini et al. [2013].

2.4.1 Test results - RHS (2500mm) column

FIGURE 2.4 illustrates the failure mode of the third column. As expected, it failed about its weak axis. The failure mode is also characterised by the formation of two plastic hinges and occurs 711s after the beginning of the heating loading.

Time [s]	711
Mean temperature [°C]	712.2
Number of plastic hinge [-]	2

Table 2.6: RHS 2500mm - Failure characteristics



Figure 2.4: Column C3 - Failure mode

A thermal gradient has been observed during the test. This gradient was mainly vertical but also horizontal. The temperature has been recorded at each pyrometers¹ and through a linear interpolation, the vertical temperature distribution in the furnace can be determined. For example, at time $t = 711s$, the temperature distribution at both sides of the column in the furnace is the one presented in FIGURE 2.5. Both horizontal and vertical thermal gradient are obvious on this graph where it can be seen that the temperature variation between two zones can reach $30^{\circ}C$ and more. Let's note that the side of the furnace near the burners is called the front side, and the side of the furnace near the closing device is called the back side.

In order to introduce this thermal gradient into the numerical model, this temperature distribution is discretized into two times five zones of $500mm$ length, as illustrated in FIGURE 2.6, which is a lateral view and which illustrates the ten zones distribution, with five zones in the front side and five zones in the back side of the column. The temperature of each zone is defined as the mean of the linear temperature distribution in this zone. This is done for both the front and the back side of the column, because there is also a horizontal thermal gradient. In the front side of the column, there are two altitudes where there are several pyrometers (pyrometers 6,9 and 11 near the bottom and pyrometers 2,3 and 12 near the top of the column, see FIGURES 6.1 and 6.5b in Annex). The temperature at those points is taken as the mean of the temperature recorded by the three pyrometers.

The temperature distribution in the ten zones at time $t = 711s$ is plotted in FIGURE 2.7 and can be compared to the linear interpolation made between the temperatures recorded by the pyrometers.

¹Pyrometers were located at a distance of $100mm$ from the steel surface.

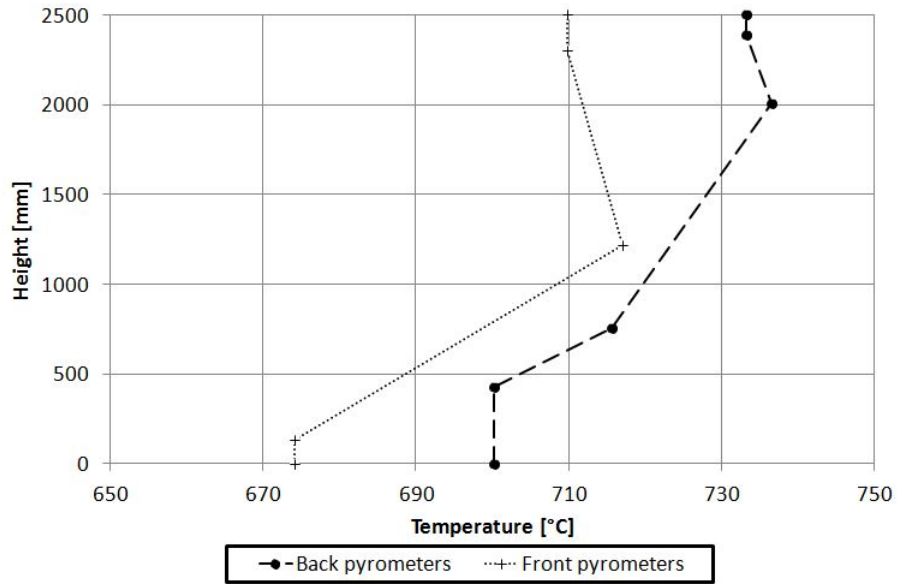


Figure 2.5: Temperature distribution at failure time ($t = 711s$) - Measured with the pyrometers

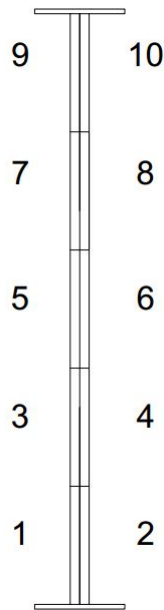


Figure 2.6: Ten zones

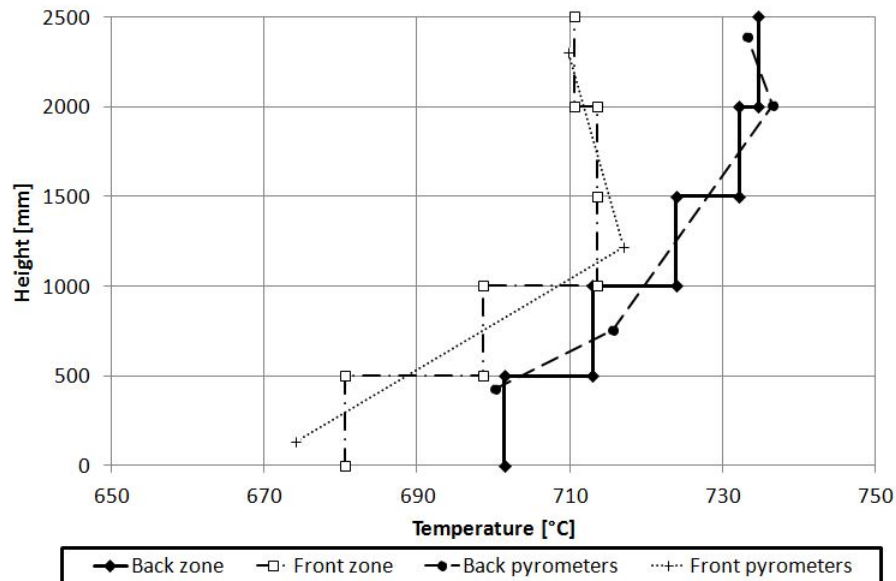


Figure 2.7: Temperature distribution at failure time ($t = 711s$) - Temperature discretization

FIGURES 2.8 and 2.9 show the *temperature – time* curves for the ten zones, and the curve that was followed during the tests (i.e. the ISO 834 heating curve, recommended in EN 1991-1-2). It can be seen in FIGURE 37 that the temperature in all the back zones is higher than the ISO 834 heating curve. In the front zones (see FIGURE 37), the temperature in zone 10 is smaller than the temperature of the ISO 834 heating curve, but the temperature in the others front zones is rather close to the temperature of this ISO 834 heating curve. This analysis illustrates also the horizontal thermal gradient between the front and the back zones.

Given the previous comments, it can be said that the applied temperature during the test was not exactly the same than that of the ISO 834 heating curve. However, the percentage of deviation of the temperature from the required temperature stays below the tolerance limit, as shown in FIGURE 2.10.

This thermal analysis of the fire tests has highlighted the presence of both vertical and horizontal thermal gradients. In several zones, the temperature at a time t is higher than that of the ISO 834 heating curve at the same time.

Therefore, after this thermal analysis, it can be concluded that the fire conditions were more severe than if the ISO 834 heating curve had been exactly followed in each zone.

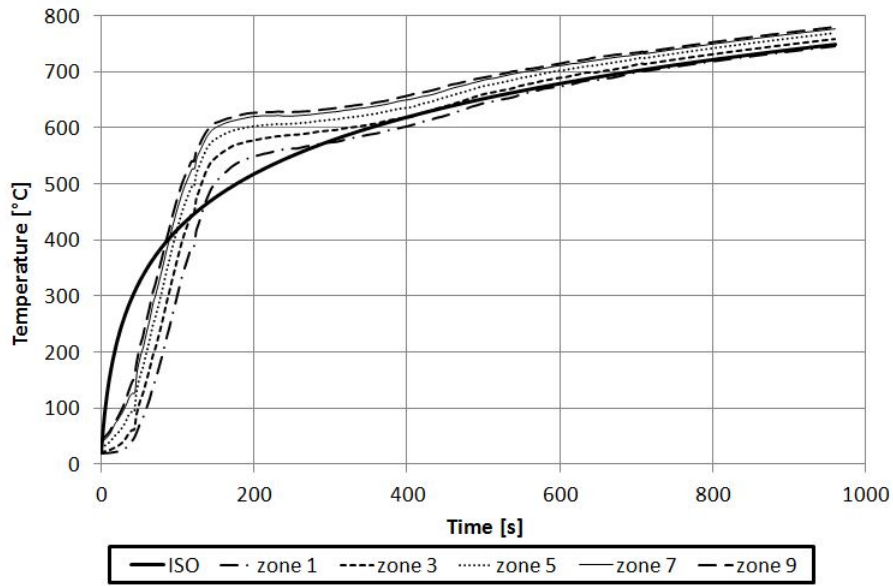


Figure 2.8: Temperature evolution in the back side of the furnace

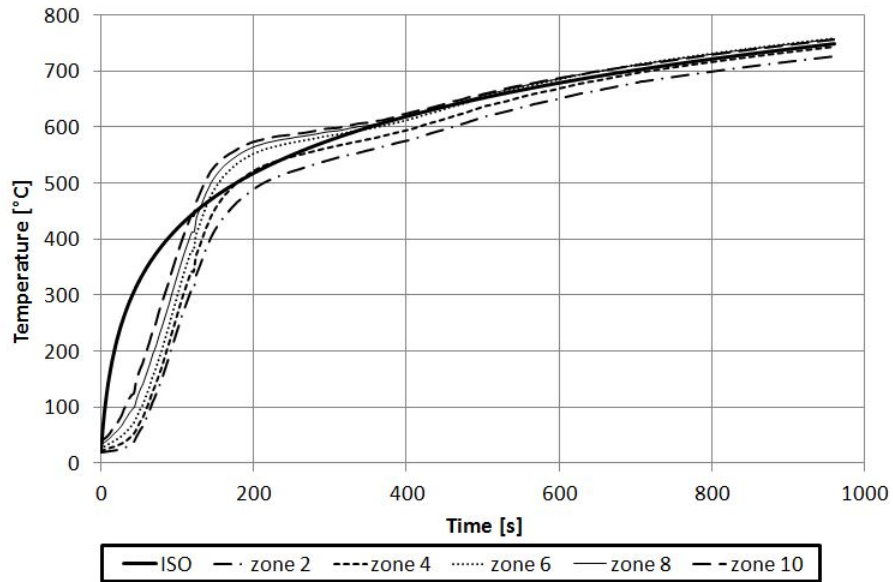


Figure 2.9: Temperature evolution in the front side of the furnace

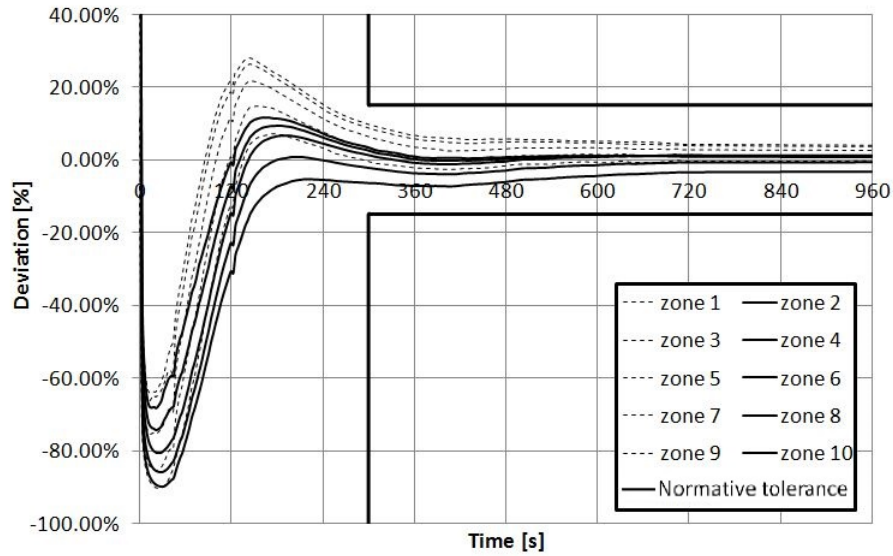


Figure 2.10: Deviation of temperature from the temperature of the ISO 834 curve

2.4.2 Test results - SHS (3000mm) column

FIGURE 2.11 illustrates the failure mode of the 3000mm height square hollow section column. The failure mode is characterized by the formation of two plastic hinges and occurs 729s after the beginning of the heating loading. The failure mode is quite close to the one observed during the fire test on the rectangular hollow section column.

Time [s]	729
Mean temperature [°C]	715.6
Number of plastic hinge [-]	2

Table 2.7: SHS 3000mm column - Failure characteristics



Figure 2.11: SHS 3000mm column - Failure mode

Similarly to the test on the rectangular hollow section column, a thermal gradient has been detected by the pyrometer's records during the test. FIGURE 2.12 illustrates the temperature distribution in the furnace at time $t = 729s$, based on a linear interpolation between the temperatures recorded by the pyrometers. A difference of $\pm 40^{\circ}C$ is observed in the back zone, between the temperature of the pyrometer located at a height of nearly $500mm$ and the one located at a height of nearly $2100mm$. There is also a horizontal thermal gradient of $\pm 20^{\circ}C$ at a height of $\pm 2100mm$ between the back and the front zones.

Then, in order to introduce this vertical and horizontal thermal gradients in the finite element model, the column is discretized into two times six zones of $500mm$. The temperature of each zone is calculated as the mean of the linear interpolation distribution of the temperature. This temperature discretization is illustrated in FIGURE 2.13 at time $t = 729s$.

The temperature evolution of the twelve zones is illustrated in FIGURES 2.14 and 2.15. Those graphs illustrate that in the back zones, the temperature of almost all the zones is higher than that of the ISO 834 heating curve, whereas in the front zones, the temperature of almost all the zones is smaller than that of the ISO 834 heating curve.

FIGURE 2.16 shows the deviation of all the zones in comparison to the temperature of the ISO 834 heating curve. It shows that the test respected the normative tolerance on the temperature evolution.

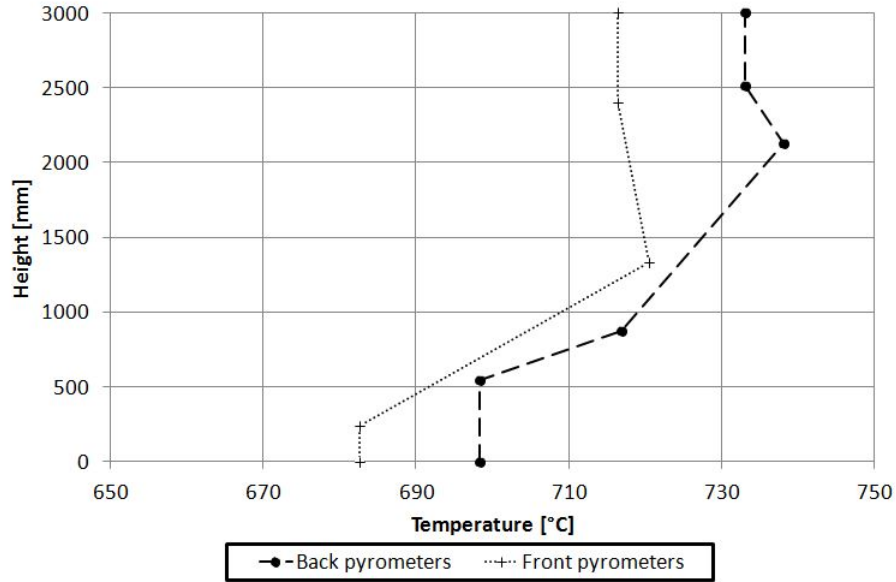


Figure 2.12: Temperature distribution at failure time ($t = 729s$) - Measured with the pyrometers

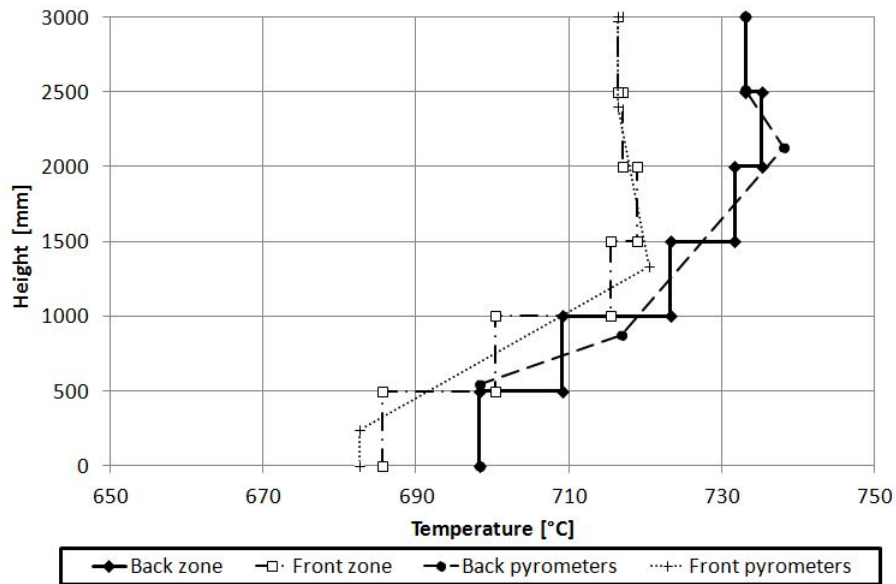


Figure 2.13: Temperature distribution at failure time ($t = 729s$) - Temperature discretization

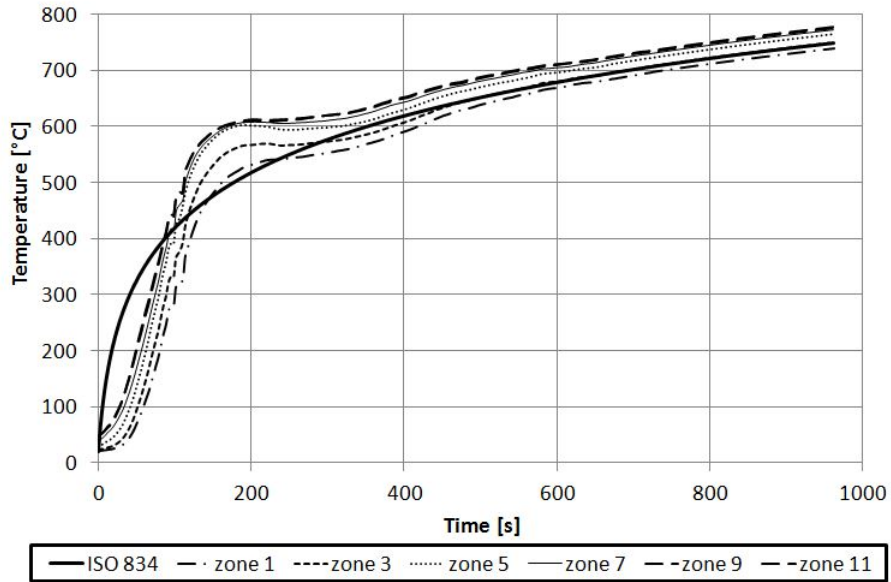


Figure 2.14: Temperature evolution in the back side of the furnace

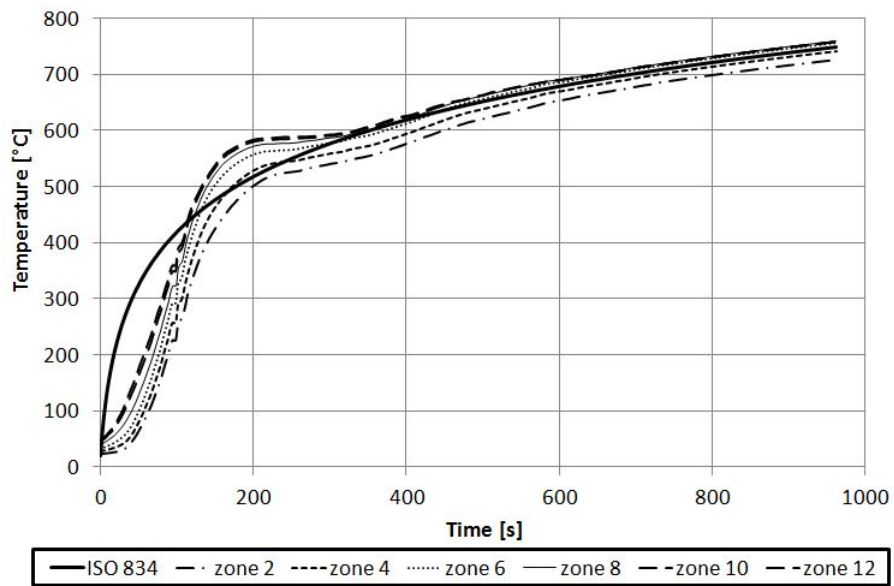


Figure 2.15: Temperature evolution in the front side of the furnace

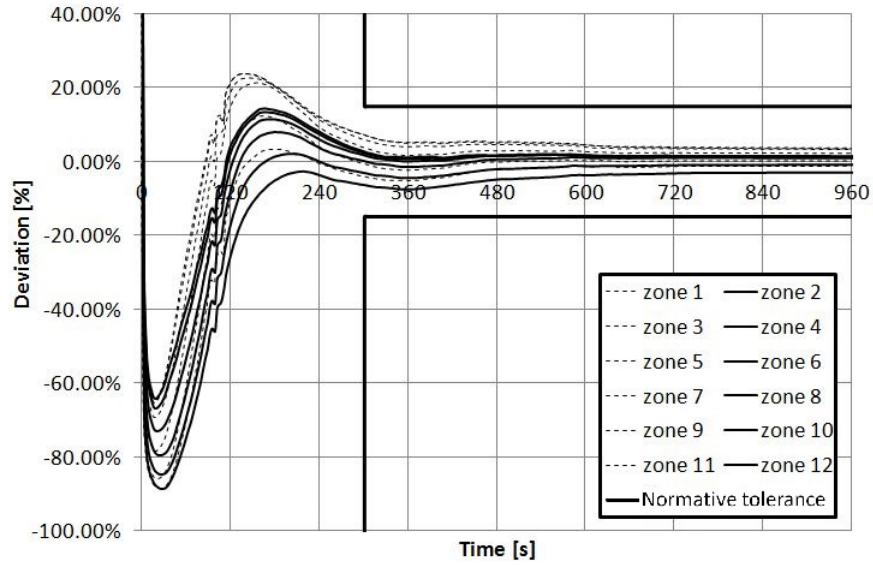


Figure 2.16: Deviation of temperature from the temperature of the ISO 834 curve

2.4.3 Test results - SHS (2500mm) column

FIGURE 2.17 illustrates the failure mode of the 2500mm height square hollow section column. The failure mode is the same than for the two previous tests and it occurs 720s after the beginning of the heating loading.

Time [s]	720
Mean temperature [°C]	714.19
Number of plastic hinge [-]	2

Table 2.8: SHS 2500mm column - Failure characteristics

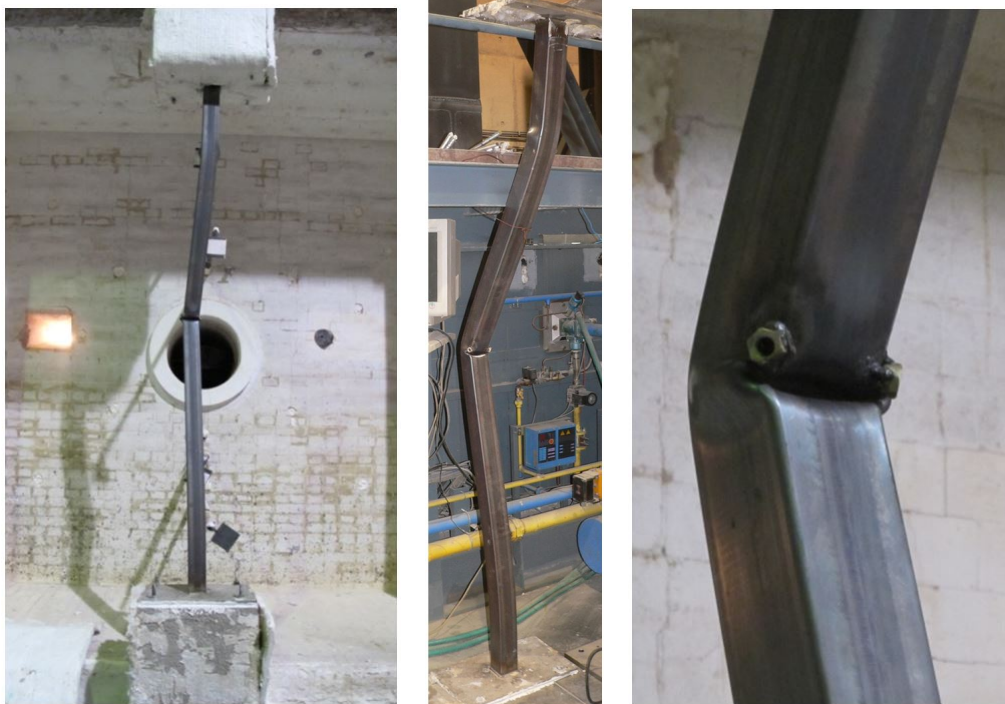


Figure 2.17: SHS 2500mm column - Failure mode

Similarly to the two previous tests, a thermal gradient is observed (see FIGURE 2.18), and the same methodology than for the previous tests is followed. Thus, the column is discretized into two times five zones of 500mm, and the temperature of each zone is calculated as the mean of the linear temperature distribution, which is based on the recorded temperature. The temperature discretization at time $t = 720s$ is illustrated in FIGURE 2.19.

The temperature evolution across time of each zone is determined and illustrated in FIGURES 2.20 and 2.21 for both the back and the front side zones. The same conclusion than for the previous tests can be done. The temperature of almost all the back zones is higher than that of the ISO 834 heating curve, and conversely, the temperature of almost all the front zones is smaller than that of the ISO 834 heating curve.

FIGURE 2.22 illustrates the deviation of the temperature of each zone in comparison to that of the ISO 834 heating curve. The same trends is observed, the temperature of the back zones (uneven zones) is almost always higher than that of the front zones (even zones). This graph shows also that the normative tolerance was respected during the test.

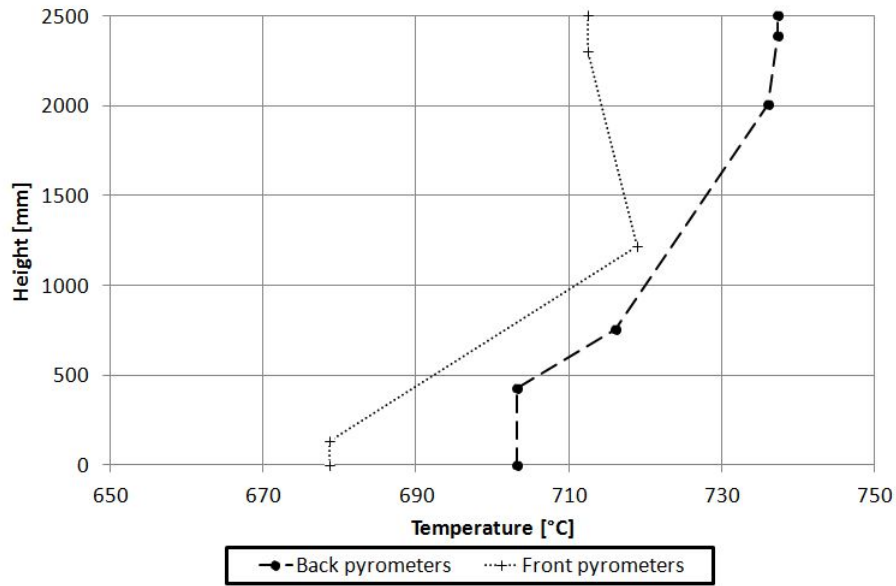


Figure 2.18: Temperature distribution at failure time ($t = 720s$) - Measured with the pyrometers

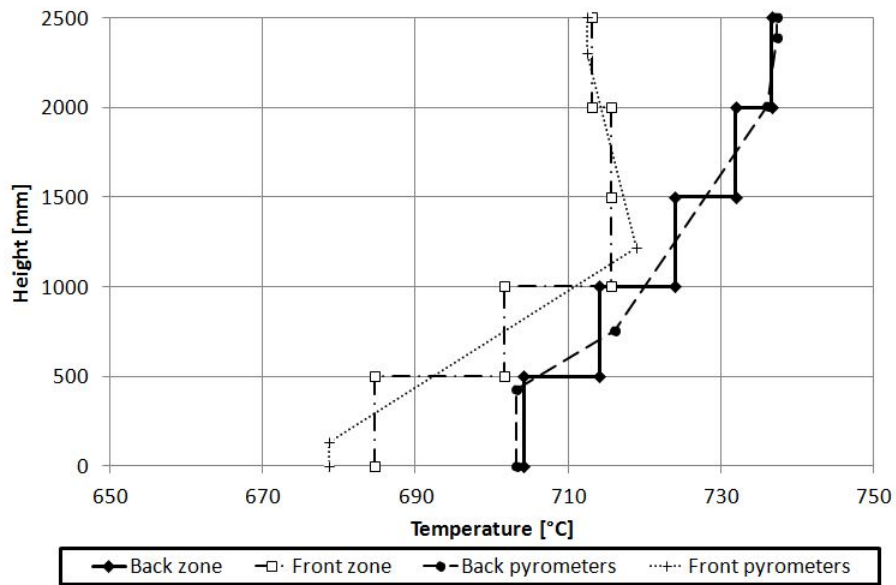


Figure 2.19: Temperature distribution at failure time ($t = 720s$) - Temperature discretization

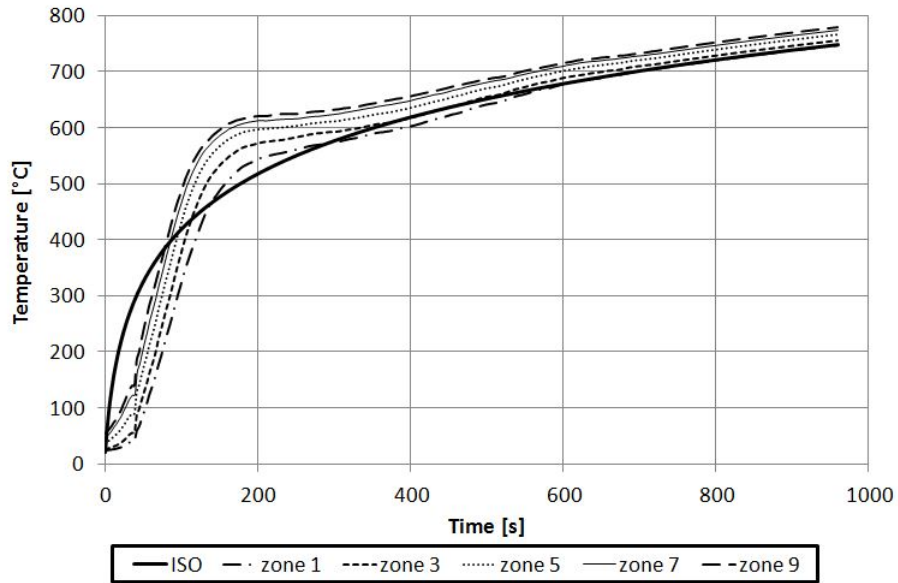


Figure 2.20: Temperature evolution in the back side of the furnace

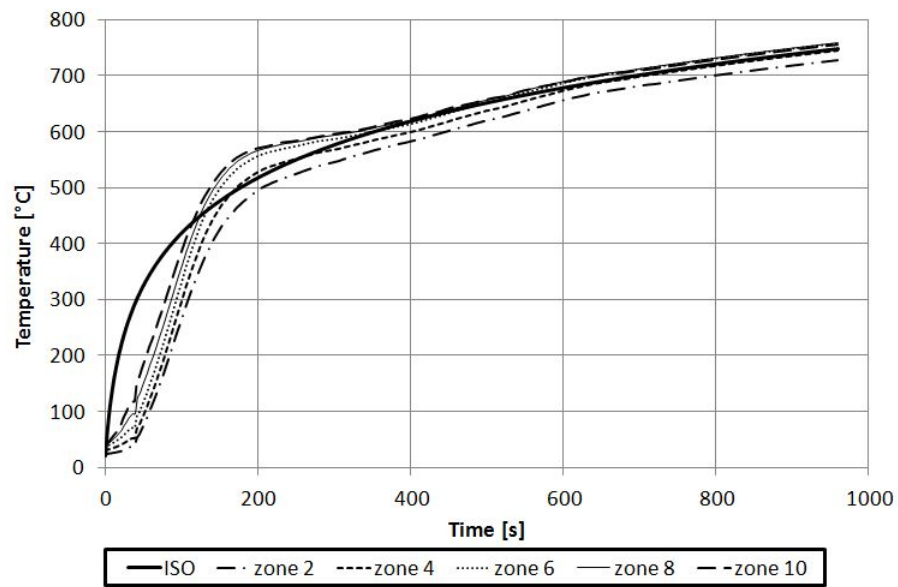


Figure 2.21: Temperature evolution in the front side of the furnace

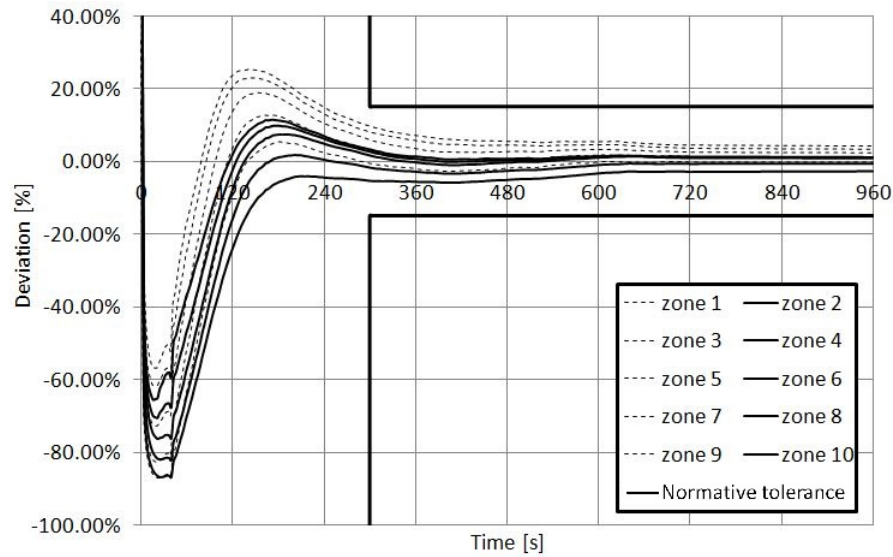


Figure 2.22: Deviation of temperature from the temperature of the ISO 834 curve

2.4.4 Conclusion

This thermal analysis of the fire tests has permit to bring out the existence of both a horizontal and a vertical thermal gradient. The temperature differences between the bottom and the top of the furnace can reach 40°C, which is not negligible. In several zones, the temperature at a time t was higher than that of the ISO 834 heating curve at the same time, resulting in a more penalizing test.

It can yet be said that the thermal gradient has an influence on the failure mode. Indeed, without thermal gradient, the failure mode would be symmetrical as that observed during the tests at room temperature, but the failure mode observed during the fire test was non-symmetrical.

Finally, the mean failure temperature of each test, calculated as the mean of the temperature of all the zones at failure time, is presented in TABLE 2.9.

RHS 2500mm	SHS 3000mm	SHS 2500mm
712.24°C	715.6°C	714.19°C

Table 2.9: Mean failure temperatures

Chapter 3

Numerical model of hollow section columns in fire

In this chapter, a finite element model is developed in order to predict the fire resistance of both rectangular and square hollow section columns. The numerical model is calibrated on the three tests described in the previous chapter.

3.1 Geometry and boundary conditions

The finite element model will be implemented into the software SAFIR. SAFIR has been developed in the University of Liege (Franssen [2011]) and is able to perform both thermal and mechanical calculation. In the following subsections, the finite element type, the kind of mesh and the boundary conditions used will be presented.

3.1.1 Finite element used in the model

Shell elements are used in the developed numerical model in order to be able to represent the behaviour of the thin-walled structure. Shell elements used for the structural model contain four nodes and each node contains six degrees of freedom.

3.1.2 Discretization of the column

For the discretization of the column, two models are studied. In the first model, the cross-section is idealized with straight corners, while in the second one, curved corners are modelled.

Straight corners

The first model consists in a hollow section with straight corners, as shown in FIGURE 3.1.

Curved corners

The previous model is then improved in order to better represent the cross-section. Corners are made of several straight lines, as shown in FIGURES 3.2 and 3.3. A comparison will be made between the cross-sections made of two or three elements per corner in order to study the influence of the discretization of this region.

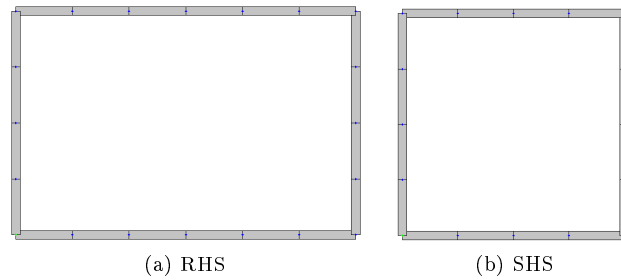


Figure 3.1: Rectangular and square hollow section with straight corners

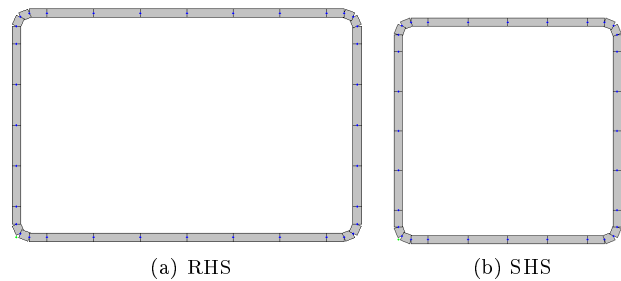


Figure 3.2: Rectangular and square hollow section with curved corners (two elements per corner)

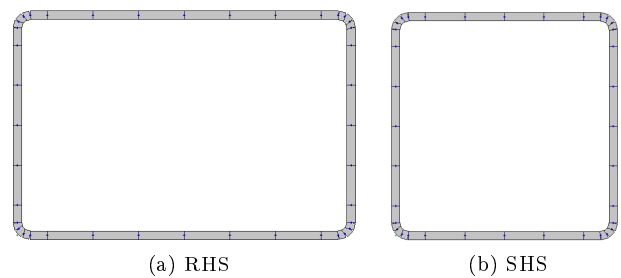


Figure 3.3: Rectangular and square hollow section with curved corners (three elements per corner)

Influence of the discretization in the corner region on the value of the area and the inertia of the cross section

Analytically, the area of the cross-section is given by EQUATION 3.1 and inertia about the weak axis can be determined with FORMULA 3.2.

$$A_{analytical} = (\pi \times (R_{ext}^2 - R_{int}^2)) + (2 \times t \times (h + b)) - (8 \times R_{ext} \times t) \quad (3.1)$$

$$I_{tot} = 2 \times (I_1 + I_2 + I_3) \quad (3.2)$$

where :

$$I_1 = \frac{(H - 2r_e) \times t^3}{12} + \left[((H - 2r_e) \times t) \times \left(\frac{H}{2} - \frac{t}{2} \right)^2 \right] \quad (3.3)$$

$$I_2 = \frac{t \times (B - 2r_e)^3}{12} + \left[((B - 2r_e) \times t) \times \left(\frac{(B - 2r_e)}{2} \right)^2 \right] \quad (3.4)$$

$$I_3 = \pi \times \frac{(r_e^4 - r_i^4)}{4} + \left[\frac{\pi}{2} \times (r_e^2 - r_i^2) \times \left((B - 2r_e) + \frac{\frac{2}{3} \times (r_i^3 + r_e^3)}{\frac{\pi}{2} \times (r_i^2 + r_e^2)} \right)^2 \right] \quad (3.5)$$

The area of the cross-section and the inertia about the weak axis are also determined for the three idealized cross-sections presented in FIGURES 3.1, 3.2 and 3.3. Results are compared in order to determine which model should be used in the numerical calibration. TABLE 3.1 shows that the model with straight corners over predict the area and the inertia about the weak axis of the cross-section, whereas the model with curved corner is closer to the real properties of the cross-section for both RHS and SHS. This analysis shows also that the difference between the idealized cross-section made of two or three elements per corner is small. Therefore, it can be said that the discretization made of two element per corner will provide good results. This does not stand for the real tested element, however it will be seen that it gives good predictions of the failure mode and of the temperature at which failure occurs.

Section type	Corner type - Number of element	A	I	error (A)	error (I)
[-]	[-]	[mm ²]	[mm ⁴]	[%]	[%]
RHS_analytical	/	1140.82	1230874.38	/	/
SHS_analytical	/	900.82	874954.4		
RHS	0	1164	1268806	+2.03	+3.08
RHS	2	1138.63	1229249.2	-0.19	-0.13
RHS	3	1139.89	1231474.5	-0.08	+0.05
SHS	0	924	913066	+2.57	+4.36
SHS	2	898.63	873509.2	-0.24	-0.17
SHS	3	899.89	875734.5	-0.10	+0.09

Table 3.1: Influence of the discretization on the value of the cross section and of inertia

3.1.3 Boundary conditions

The specimen were full-restrained at both ends, but the axial displacement was allowed at the loaded end, in order to permit the thermal dilatation and the contraction due to axial loading. A scheme of the system is shown in FIGURE 3.4.

FIGURE 4.4 illustrates the boundary conditions implemented into SAFIR in order to model the boundary conditions described here above. A 100mm thick plate is used at the top of the column in order to transmit the punctual vertical load to the column without introducing local buckling due to the punctual loading. Blue arrows illustrate blocked rotational degrees of freedom and red arrows illustrate blocked translational degrees of freedom. At the top of the column, all the rotational degrees of freedom are blocked and the horizontal displacements of the center of the top plate are blocked in order to prevent the movement of the entire end section. However the horizontal displacements of the other node of the end plate are free, in order to allow the thermal dilatation of the end plate. The horizontal displacement of the center of each side are blocked by symmetry of the thermal dilatation.

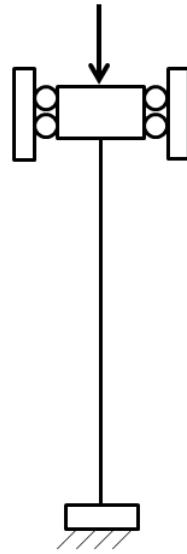


Figure 3.4: Boundary conditions during the test

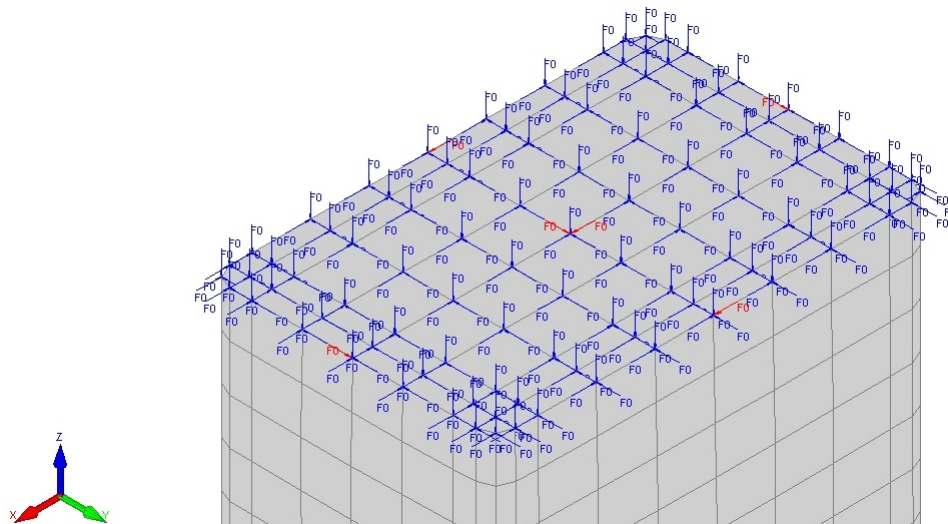


Figure 3.5: Boundary conditions - Numerical model

3.2 Material modelling

3.2.1 Mechanical properties

First of all, the law implemented into SAFIR is the one recommended in the European code EN 1993-1-2 and is presented in SECTION 1.1.3. To use this curve, elevated temperature material properties are needed.

Those elevated temperature material properties are determined from the room temperature material properties. The reduction factors recommended by the European code EN 1993-1-2 for the grade 1.4003

of stainless steel are used (see TABLE 1.3). Then, the material properties at ambient temperature are needed to be able to model the material behavior (i.e. to be able to predict the $\sigma - \varepsilon$ curve).

The measured room temperature material properties are used in the numerical model. However, two methods will be presented.

The first one consists in directly using the measured room temperature material properties. In this first method, there is a certain deviation between the theoretical representation of the $\sigma - \varepsilon$ curve in SAFIR and the measured $\sigma - \varepsilon$ curve.

The second method consists in fitting the measured behaviour law in order to obtain a numerical behaviour law as close to the measured one as possible. Those two methods are presented in the following subsections.

Note that during the finite element model calibration, the strength enhancement in the corner regions is not introduced. However, the measured properties used in the finite element model contain the strength enhancement of the flats. In order to introduce the strength enhancement in the corner regions during the parametric study, it is worth pointing that the section discretization contains elements with a length of $2t$ (where t is the thickness of the plate) at both side of each corner, as shown in FIGURE 3.6.

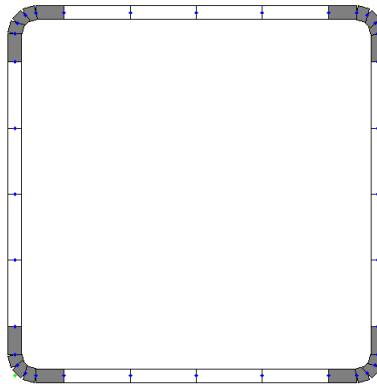


Figure 3.6: Strength enhancement in corner regions

Method 1 : Measured material properties

Tensile tests at ambient temperature have been performed, and material properties have been obtained. However, tensile tests give conventional values while the parameters needed to use the law proposed in EN 1993-1-2 are the rational stresses and strains. Therefore, FORMULAS 2.1 and 2.2 have to be used in order to get the rational stresses and strains from the conventional ones.

FIGURE 3.7 illustrates the comparison between the stress-strain curve obtained during the test and those predicted using the material behavior law proposed in EN 1993-1-2, for the measured material parameters presented in TABLE 3.2. The predictive law is close enough to the measured one, but the stresses are a little overrated in the second stage of the curve (i.e. for deformation higher than the total deformation corresponding to a plastic deformation of 0.2%).

$f_{0.2p}$ [MPa]	411.77
f_u [MPa]	562.8
E_0 [MPa]	220000
ε_u [-]	0.2

Table 3.2: Measured material parameters - RHS

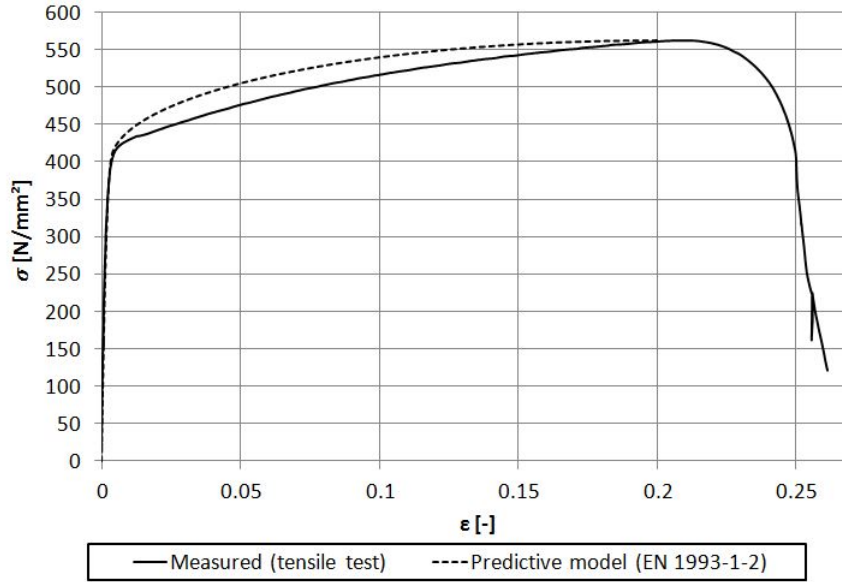


Figure 3.7: Comparison between the law proposed in EN 1993-1-2 using the measured properties and the stress-strain curve obtained during the test

Method 2 : Fitted law

The aim of this method is to obtain a material law as close as possible to the measured stress-strain curve. However, the modelled law must keep a physical meaning. Indeed, during the numerical simulation at elevated temperature, the parameters will be multiplied by reduction factors which have been defined for specific material properties. Therefore, the measured material parameters of TABLE 3.2 are all fixed, excepted the ultimate strength f_u which will vary so as to minimize the difference between the measured and the predicted curves for strains smaller than $\varepsilon = 0.15$. The choice of the value 0.15 as limit is based on the assumption that the strains in shell elements are not higher than this value. Naturally, this assumption has been checked a posteriori.

Parameters used are presented in TABLE 3.3 and FIGURE 3.8 shows that the predictive and measured laws are closer when the fitted parameters are used instead of the measured one.

$f_{0.2p}$ [MPa]	411.77
f_u [MPa]	533.92
E_0 [MPa]	220000
ε_u [-]	0.2

Table 3.3: Fitted material properties - RHS

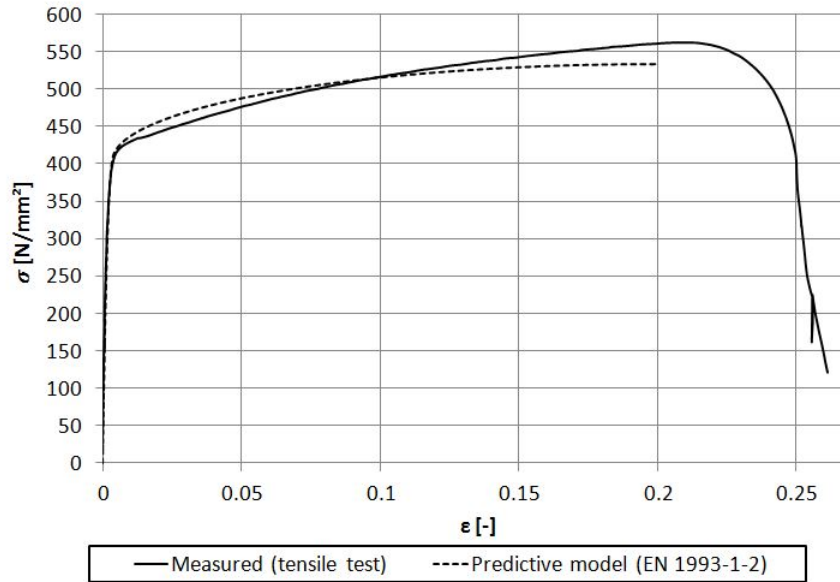


Figure 3.8: Comparison between the law proposed in EN 1993-1-2 (fitted on the measured law) and the stress-strain curve obtained during the test

3.2.2 Thermal properties

The thermal properties introduced into the finite element model are presented in TABLE 1.2. As explained in SECTION 1.1.1, these values are recommended by the European code EN 10088-1 and EN 1993-1-2.

3.3 Initial geometrical imperfections

In order to represent the real behaviour of the column, initial geometrical imperfections must be modelled.

Usually, equivalent geometrical imperfections are used in order to take into account both the geometrical and the structural imperfections. However, the effect of residual stresses will be studied in this work. Hence, only the geometrical imperfections are introduced.

According to EN 1993-1-5 - Annex C, the imperfection to use in a numerical model is 80% of the fabrication tolerances.

3.3.1 Global imperfection

For structural hollow section columns, EN 1090-2 recommends to consider a deviation tolerance of $\Delta = \frac{L}{750}$, as shown in FIGURE 3.9. Thus, by considering a global imperfection equal to 80% of the geometrical tolerance, an imperfection of $0.8 \times \frac{L}{750} = \frac{L}{937.5}$ is introduced into the numerical model.

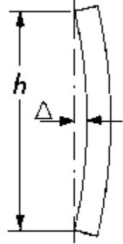
4	<p>Straightness of a single storey column:</p> 	<p>Location of the column in plan, relative to a straight line between position points at top and bottom:</p> <ul style="list-style-type: none"> - generally - structural hollow sections 	<p>$\Delta = \pm h/750$ $\Delta = \pm h/750$</p>
---	--	---	---

Figure 3.9: Global imperfection tolerance - EN 1090-2

3.3.2 Local imperfection

The local fabrication tolerances used are that provided by the steel supplier and they are based on the EN 10219-2. The local fabrication tolerances are given in TABLE 3.4. Therefore, the amplitude of the introduced local imperfections is equal to 80% of those fabrication tolerances. The FORMULAS 3.6 and 3.7 give the expression of those local imperfection. The shape of those initial local imperfections is a sine wave whose half wavelength is equal to the width of the walls of the cross-section, as illustrated in FIGURE 3.10a. FIGURE 3.10b gives the initial local imperfection distribution in the cross-section.

Side length h [mm]	Tolerance
$H, B < 100mm$	$\pm 1\%$ with a minimum of $\pm 0.5mm$
$100mm \leq H, B \leq 200mm$	$\pm 0.8\%$
$H, B > 200mm$	$\pm 0.6\%$

Table 3.4: Tolerances for square and rectangular hollow sections - EN10219-2

$$\delta_1 = 0.8 \times 0.008 \times b \tag{3.6}$$

$$\delta_2 = 0.8 \times 0.008 \times h \tag{3.7}$$

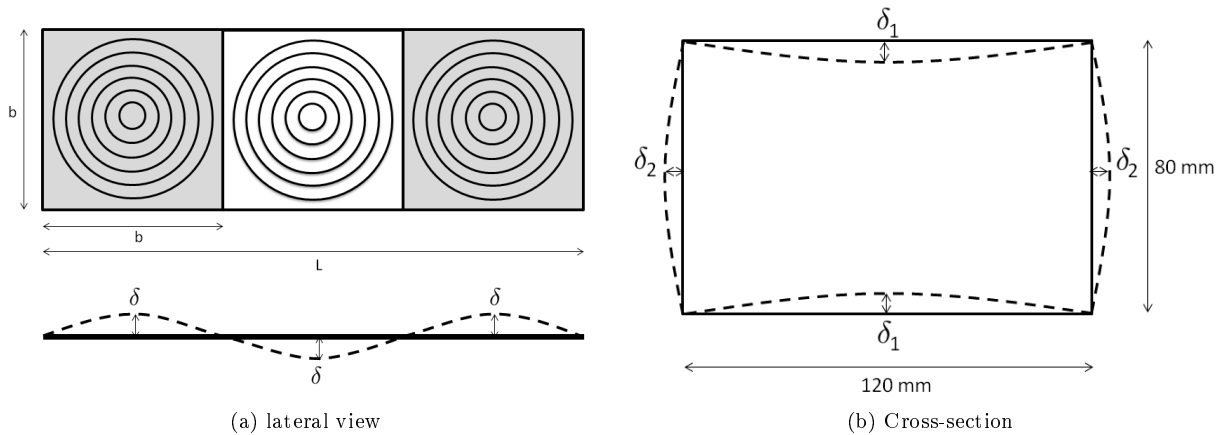


Figure 3.10: Local imperfections - shape

3.4 Residual stresses

Residual stresses are present in cold-rolled sections due to their forming process. It starts with the uncoiling and the leveling of the sheet material, and then, the cold rolling through a series of shaped rollers is performed, in order to produce square or rectangular hollow sections.

Gardner and Cruise’s model (Gardner and Cruise [2009])

Gardner and Cruise have made a proposal in order to introduce residual stresses into numerical model for stainless steel elements. This model does only consider the longitudinal residual stresses divided into bending and membrane residual stresses.

Concerning membrane residual stresses, no particular distribution emerges. Hence, mean and characteristics values of the absolute normalized membrane residual stresses are used as representative magnitudes. The characteristics values of membrane residual stresses are presented in TABLE 3.5.

Gardner noticed a tendency of tension at the outer surface of the section for the normalized bending residual stresses. He found characteristic values for the flat and corner regions (see TABLE 3.6 and FIGURE 3.11).

Flat	Corner
$0.37 \times \sigma_{0.2}$	$0.24 \times \sigma_{0.2}$

Table 3.5: Membrane residual stresses - characteristic values

Flat	Corner
$0.63 \times \sigma_{0.2}$	$0.37 \times \sigma_{0.2}$

Table 3.6: Bending residual stresses - characteristic values

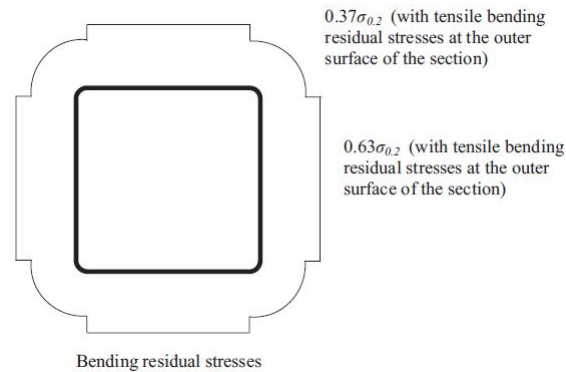


Figure 3.11: Membrane residual stresses distribution - Gardner's proposal

Residual stresses effects(Jandera et al. [2008])

Jandera has studied the effect of residual stresses on the bearing capacity of columns. He noticed that residual stresses may have a positive effect for non dimensional slendernesses $\bar{\lambda}$ up to 1.4. It is due to the fact that, above approximately 0.12% strains, the tangent modulus of the residual stresses containing curve is higher than that of the stress free curve. This tangent modulus has a significant importance on the column buckling resistance. Therefore, if this tangent modulus increases, the buckling load increases too. For high column slenderness ($\bar{\lambda} > 1.5$), strains at failure are lower, and the residual stresses may have a negative effect on the buckling load. However, the structural behaviour of columns of high slenderness is less sensitive to the presence of residual stresses. Therefore, significant variation in bearing capacity would not be expected.

Residual stresses model

Only the longitudinal residual stresses are taken into account presently. They are distributed over 3 zones as depicted in FIGURE 3.12 and such that their distribution is self-balanced.

The transverse bending residual stresses are taken into account in the measured material properties, due to the fact that corner coupons are outspread before the tensile test. Thus the effect of those transverse bending residual stresses appears in the enhanced proof strength measured during the tensile test. Therefore, only the longitudinal bending residual stresses are introduced.

Concerning the membrane residual stresses, the transverse residual stresses are negligible compared to the longitudinal ones. Thus, the longitudinal membrane residual stresses are the second residual stresses introduced into the finite element model.

Thus, the residual stresses distribution introduced in the finite element model is shown in FIGURE 3.12. The amplitudes of those residual stresses are presented in TABLE 3.7¹, they are based on Gardner's measurements.

	Bending residual stresses	Membrane residual stresses
Central portions of the plate	$\pm 0.63 \sigma_{0.2}$	$+0.37 \sigma_{0.2}$
End portions of the plate	$\pm 0.63 \sigma_{0.2}$	$-0.24 \sigma_{0.2}$
Corner regions	$\pm 0.37 \sigma_{0.2}$	$-0.24 \sigma_{0.2}$

Table 3.7: Residual stresses

¹Signe "+" for tensile stresses and signe "-" for compressive stresses.

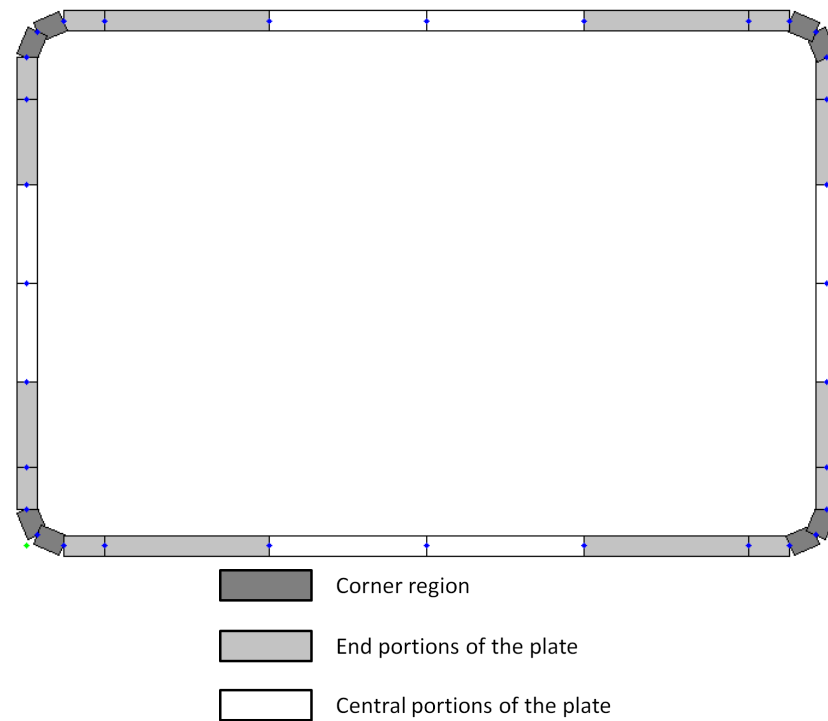


Figure 3.12: Residual stresses distribution on the rectangular cross-section

3.5 Temperature development in the cross-section

First of all, FIGURE 3.13 illustrates the time lag between the temperature development in the stainless steel material and in the furnace. Therefore it can be seen that it is not correct to apply the ISO 834 heating curve directly to the material and a thermal analysis is required to determine the temperature in the stainless steel material in function of the temperature of the gases.

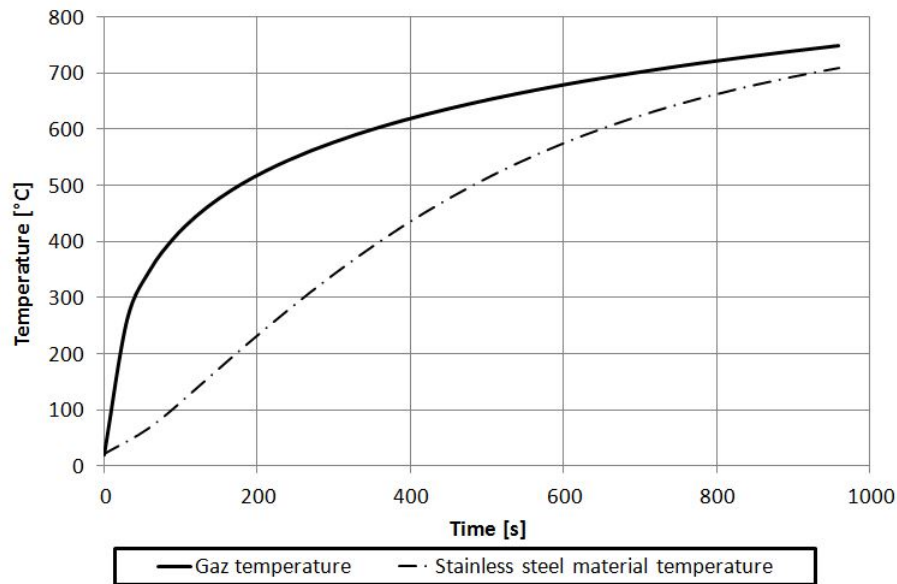


Figure 3.13: Temperature evolution in the furnace and in the stainless steel material

1D thermal analysis

The temperature in the furnace was recorded by several pyrometers. Then, the column was discretised into 10 (see FIGURE 3.14) or 12 zones (according to the column's height) and a temperature distribution has been determined from the recorded temperature and the position of the corresponding pyrometers (see SECTION 2.4).

Thus the temperature evolution of each zone determined in SECTION 2.4 from the temperatures recorded by the pyrometers is applied to the surface of a shell element and the temperature evolution of this shell element over time is calculated. This calculation is performed 10 times (or 12 times, depending on the column's height) in order to determine the temperature evolution of the material in each zone. Then, those determined temperature evolutions are applied to the shell elements in the structural analysis.

The distribution in the cross-section of the temperatures applied to the shell elements in the mechanical model is illustrated in FIGURE 3.15 for the 1D thermal analysis. The cross-section is divided into two zones : the front side and the back side of the column, corresponding to the front side and the back side of the furnace.

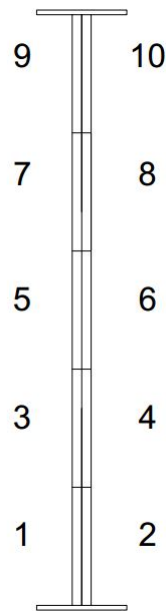


Figure 3.14: Temperature distribution - ten zones model

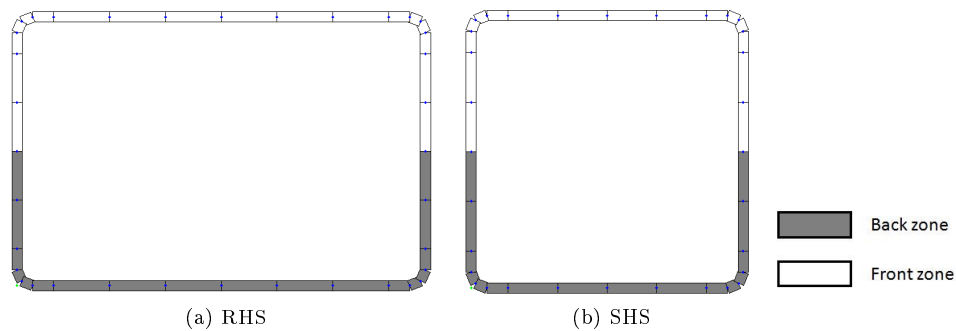


Figure 3.15: Temperature distribution in the cross-section

2D thermal analysis

The 1D thermal analysis described here above takes into account the effect of the temperature of the gases in the furnace on the temperature evolution in the material. However, this model does not take into account the thermal conductivity across the cross-section and the thermal radiation between the faces. Therefore, a numerical 2D thermal analysis has been performed in order to study the effects of those phenomenons.

Temperature evolutions determined in SECTION 2.4 are applied to outer walls as illustrated in FIGURES 3.16a and 3.17a. Thus the temperatures of the front side zones of the furnace are applied on a half of the outer outline and the temperatures of the back side zones of the furnace are applied on the other half of the outer outline. FIGURES 3.16b and 3.17b illustrate the horizontal thermal gradient between the front and the back of the furnace obtained with the 2D thermal analysis, respectively for rectangular and square hollow section.

In order to show the importance of this 2D thermal analysis, the temperature evolution in the material for zones 9 and 10 of the rectangular hollow section column, according to both 1D and 2D thermal analysis, is plotted in FIGURE 3.18a. It can be seen that the temperatures obtained through the 2D thermal analysis are higher than that obtained through the 1D thermal analysis.

FIGURE 3.18b shows that the difference of temperature in both type of analysis around the failure time ($\approx 700s$) for both the front and the back side of the furnace, can not be neglected ($\approx 30^{\circ}C$). The consequences of this second thermal analysis is that, in the previous thermal model, the temperature of the stainless steel column was underestimated.

The distribution in the cross-section of the temperatures applied to the shell elements in the mechanical model is illustrated in FIGURE 3.19 for this 2D thermal analysis. There are three zones : the back zone which is the hottest one, the front zone which is the coldest and between that zones, the intermediate zone.

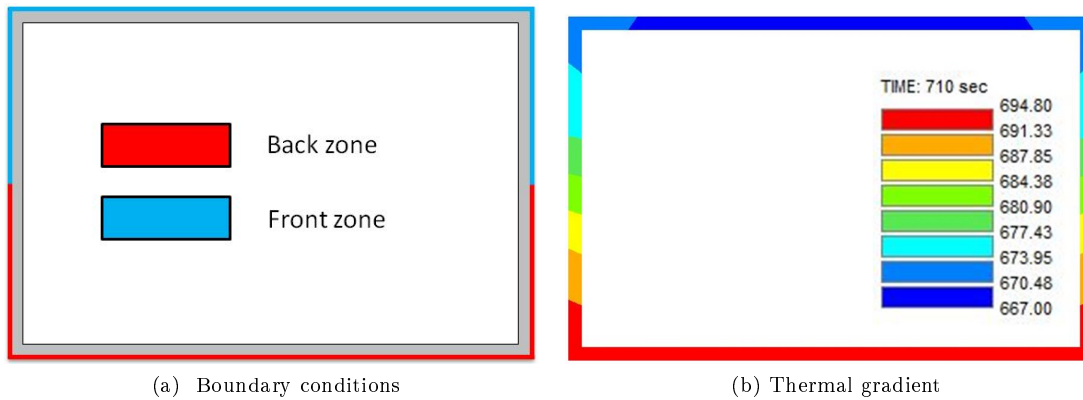


Figure 3.16: RHS - 2D thermal analysis

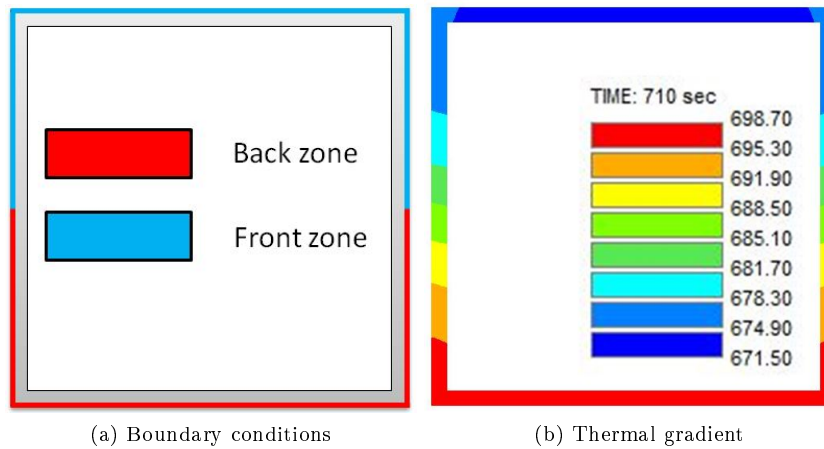
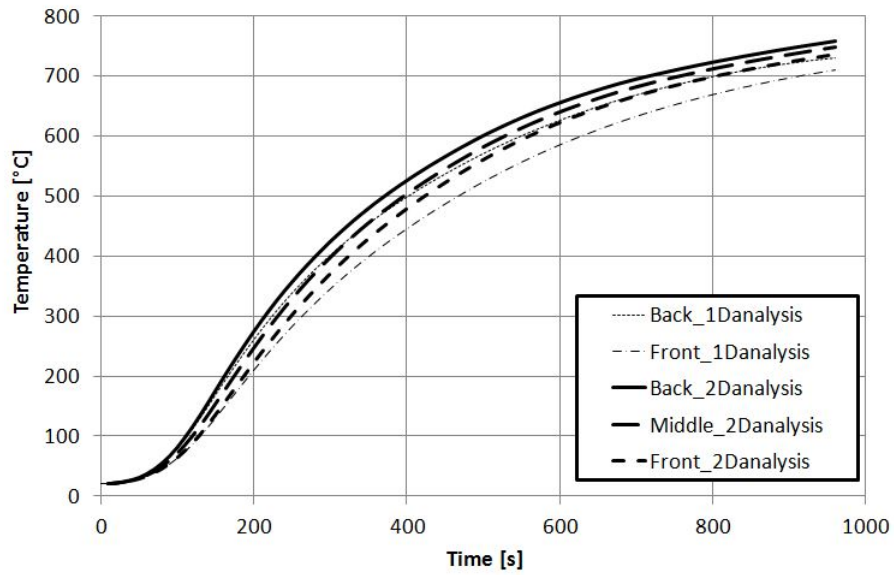
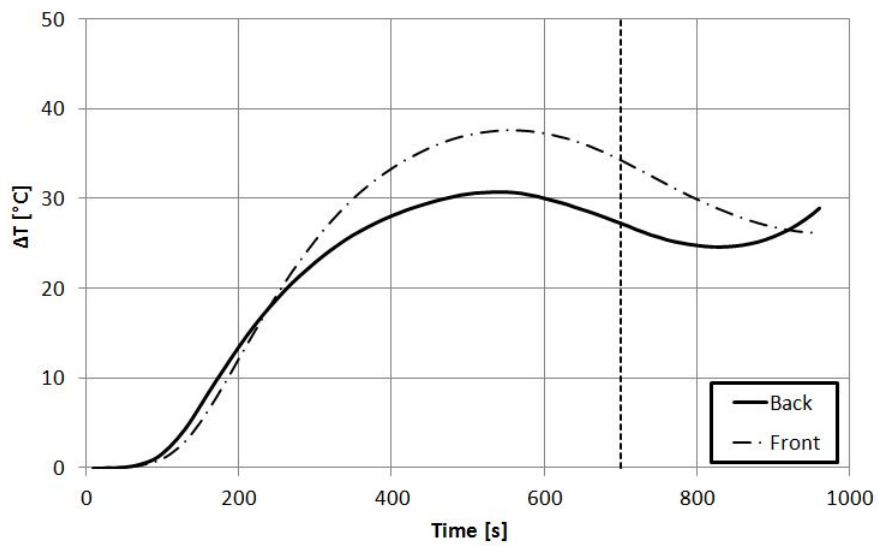


Figure 3.17: SHS - 2D thermal analysis



(a) Temperature evolution



(b) Difference of temperature

Figure 3.18: Comparison of the thermal analyses : 2D - 1D

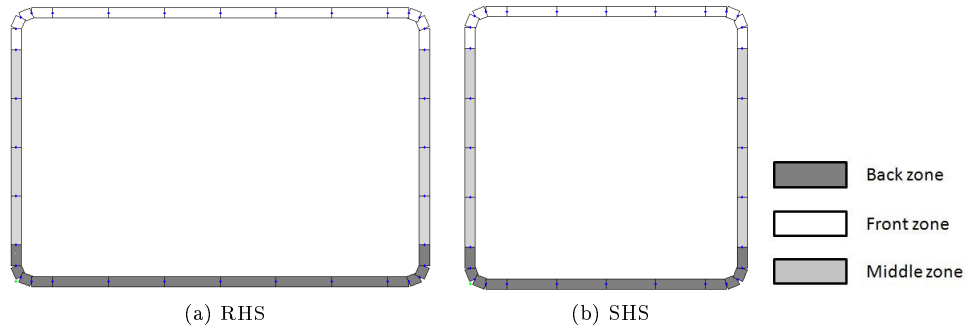


Figure 3.19: Temperature distribution in the cross-section - 2D thermal analysis

3.6 Loading conditions

During the tests, the specimens were concentrically loaded at thirty percents of their buckling resistance at ambient temperature calculated according to the European code EN 1993-1-4 considering $f_y = 350MPa$. Therefore, this load was applied from the beginning and maintained constant during the test, as illustrated in FIGURE 3.20. The values of this vertical load are presented in TABLE 3.8 for each tested column.

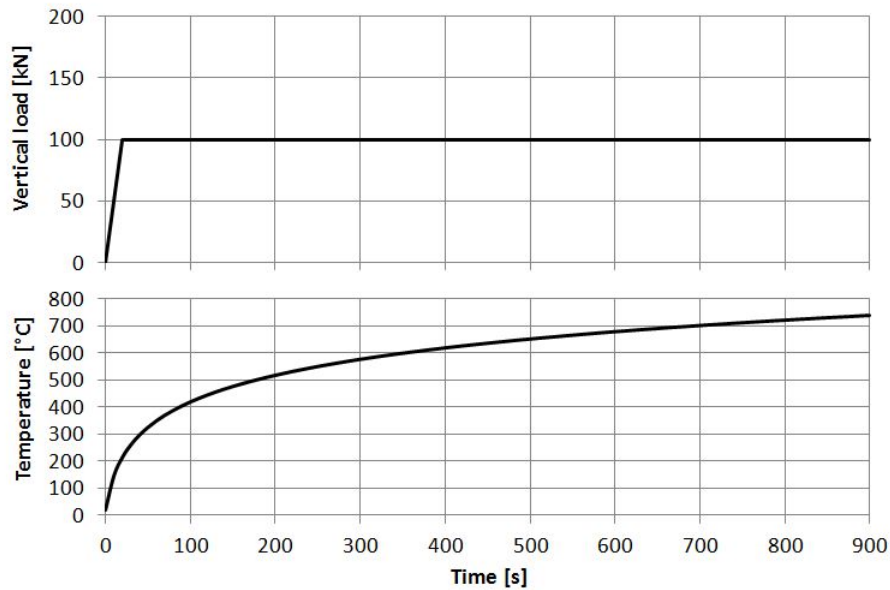


Figure 3.20: Loading conditions

RHS 2500 mm	SHS 2500 mm	RHS 3000 mm
100 kN	78 kN	72 kN

Table 3.8: Vertical loading

3.7 Numerical results

Two types of numerical analysis are performed for each model. A heat transfer analysis is initially performed to obtain the temperature development in the columns. Then, those results are incorporated into the geometrically and materially non-linear structural analysis. Those two analyses have been presented in the previous sections.

The results of the numerical analyses are presented in the following subsections.

3.7.1 RHS 2500mm

The finite element model of the rectangular hollow section column with a height of 2.5m is compared to the tests results of this column. In the following models, the measured material properties, obtained through tensile tests at ambient temperature on coupons cut from the tested columns, are applied for the entire cross-section. In fact, the strength enhancement in the corner region is higher than that in the flats. However, it is not taken into account in the finite element models used to model the tested columns.

Model 1 : basic model

This first model is made of straight corner, the geometrical and material properties used are the measured ones and the temperature distribution is uniform and follows the ISO 834 heating curve. It is an inelastic analysis including material nonlinear model using the predictive material law recommended by the European code EN 1993-1-2 and the initial global geometrical imperfection is modelled. The values of the parameters of this first model are presented in TABLE 3.9.

“*Corner type*”, “*Material law*”, “*Thermal gradient*”, “*End insulation*” and “ $\sigma_{residual}$ ” are the parameters which will be studied in the next finite element models in order to study their influence. A description of those parameters is given hereafter.

- *Corner type* : Gives the type of corner used in the model. It can be straight or curved.
- *Material law* : Gives the kind of material law used. It is always the Ramberg-Osgood model recommended by the European code EN 1993-1-2, but the material properties used can be the measured or the fitted ones.
- *Thermal gradient* : Gives the number of zones if a thermal gradient is modelled.
- *End insulation* : Use to know if the thermal insulation at both column ends is taken into account.
- $\sigma_{residual}$: Use to know if the residual stresses are used in the finite element model.

FIGURE 3.21, where the amplified deformation is represented, illustrates the symmetrical failure mode of this first model. At the failure, the temperature of the gases is 735.25°C.

b	h	L	r_i	r_e	t	E_0	$f_{y,flat}$	$f_{y,corner}$	f_u
[mm]	[mm]	[mm]	[mm]	[mm]	[mm]	$\frac{N}{mm^2}$	$\frac{N}{mm^2}$	$\frac{N}{mm^2}$	$\frac{N}{mm^2}$
79.4	119.5	2500	—	—	2.97	220000	411.77	411.77	562.8
<i>Corner type</i>		<i>Material law</i>		<i>Thermal gradient</i>		<i>End insulation</i>		$\sigma_{residual}$	
[—]		[—]		[—]		[—]		[—]	
<i>Straight</i>		<i>R – O (measured)</i>		—		—		—	
<i>FE type</i>		NG	NL	Nb	Nh	Nc	N_{axial}	Δ	δ
[—]		[—]	[—]	[—]	[—]	[—]	[kN]	[mm]	[mm]
1^{st} degree		4	125	4	6	0	–100	$0.8 \frac{L}{750}$	—

Table 3.9: RHS 2500mm- model 1

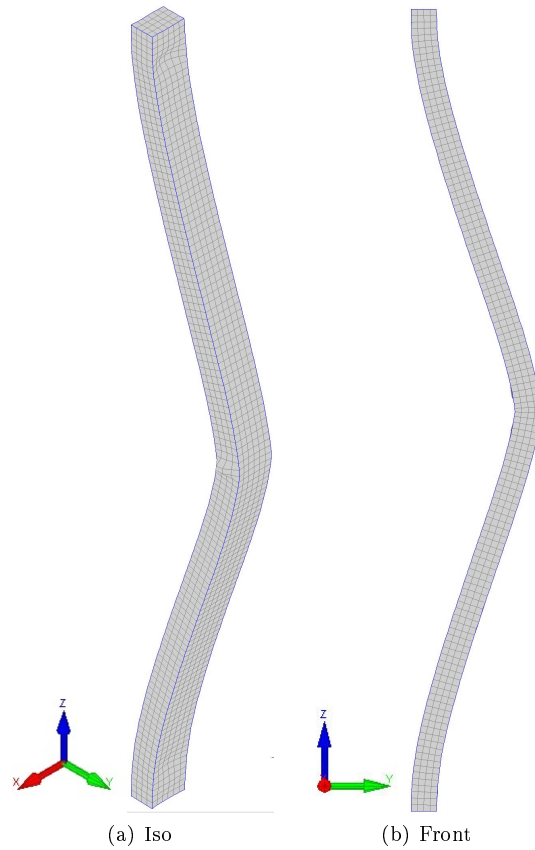


Figure 3.21: RHS 2500mm - model 1 : failure mode

Model 2 : influence of local imperfections

This second model has the same properties than the previous one, but local imperfections are added according to the rules described in SECTION 3.3.2. The values of the parameters used in this second model are given in Annex (TABLE 6.2).

FIGURE 3.22 illustrates the failure mode of this second model. It is the same than that presented in FIGURE 3.21, but local waves develop due to the introduction of initial local imperfections. By introducing initial local imperfections, the failure temperature also decreases from 735.25°C to 729.7°C .

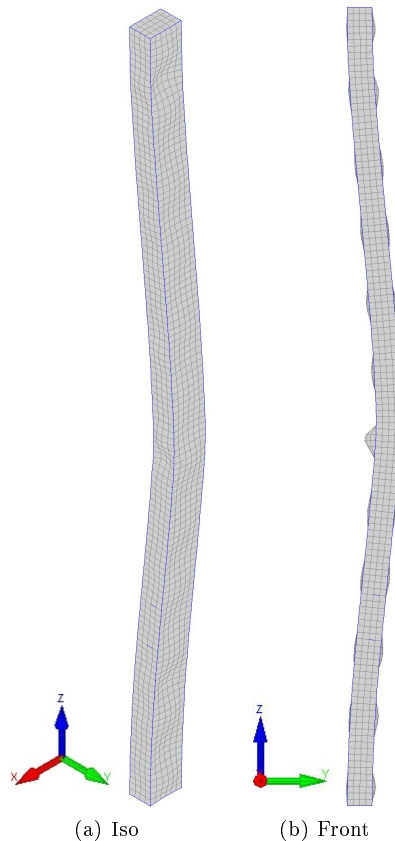


Figure 3.22: RHS 2500mm - model 2 : failure mode

Model 3 : influence of curved corners

Introducing curved corners in the finite element model has two main effects. It gives a model which is closer to the real geometrical properties (cross-section area and inertia) and it reduces the effect of local buckling in the flats. When the curved corner cross-section is compared to the straight corner cross-section, the two differences mentioned above have opposite effects. The reduction of the cross-section and the inertia about the weak axis reduces the bearing capacity of the column. Conversely, the introduction of the curved corner in the cross-section reduces the slenderness of the flats and thus have a beneficial effect on the column's bearing capacity.

The curved corner model is made of three elements per corner. The values of the parameters are presented in the TABLE (3.10).

The failure mode obtained is the same than that obtained in model 2 and is presented in FIGURE (3.24). There is a small deviation in the failure temperature, which decreases from 729.7°C for the second model to 728.5°C for this model.

Then, the same simulation has been done with two elements per corner, and it is shown that there is no difference when using two or three elements to model the corner. It is useful to notice that using two elements to model the corner allows to use less shell elements and reduces the computation time. Indeed, if three elements are used to model the corner, the width of those elements is smaller than if

two elements were used. Therefore, in order to respect a maximum value of the aspect ratio (equal to 3), the number of elements across the column's length will be higher in the model which contains three elements per corner than in that with two elements per corner.

Hence curved corners will be used in the next models, and they will be modelled with only two elements, in order to reduce the number of elements in the finite element model.

b	h	L	r_i	r_e	t	E_0	$f_{y,flat}$	$f_{y,corner}$	f_u
[mm]	[mm]	[mm]	[mm]	[mm]	[mm]	$\frac{N}{mm^2}$	$\frac{N}{mm^2}$	$\frac{N}{mm^2}$	$\frac{N}{mm^2}$
79.4	119.5	2500	3.86	6.86	2.97	220000	411.77	411.77	562.8
<i>Corner type</i>		<i>Material law</i>		<i>Thermal gradient</i>		<i>End insulation</i>		$\sigma_{residual}$	
[-]		[-]		[-]		[-]		[-]	
Curved		R - O (measured)		-		-		-	
<i>FE type</i>		NG	NL	Nb	Nh	Nc	N_{axial}	Δ	δ
[-]		[-]	[-]	[-]	[-]	[-]	[kN]	[mm]	[mm]
1 st degree		4	300 200	4	6	3 2	-100	$0.8 \frac{L}{750}$	$0.8 \times 0.008 \times b$ $0.8 \times 0.01 \times h$

Table 3.10: RHS 2500mm - model 3

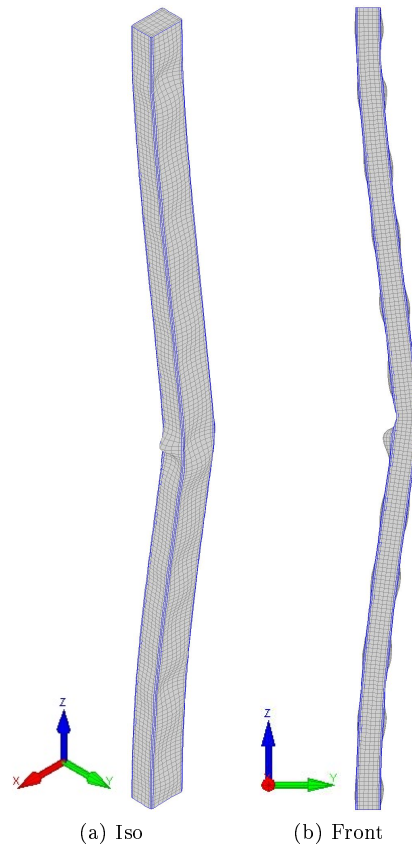


Figure 3.23: RHS 2500mm - model 3 : failure mode

Model 4 : influence of thermal gradient

The parameters used in this model are the same than in the third model. Curved corners are modelled (with two elements per corner), both local and global imperfections are used and the geometrical and material properties used are the measured ones. However, this model takes into account the vertical and horizontal thermal gradient in the furnace. This thermal gradient is introduced by dividing the column into 10 zones, as described in SECTION 3.5 and the temperature evolutions used are those determined through the 1D thermal analysis. The values of the parameters used in this fourth model are given in Annex (TABLE 6.3).

FIGURE 3.24 illustrates the failure mode obtained with this fourth model. This failure mode is very close to that obtained during the tests, as shown in FIGURE 3.25. This failure mode is made of two main hinges located in the upper zone of the column and near the mid-height of the column.

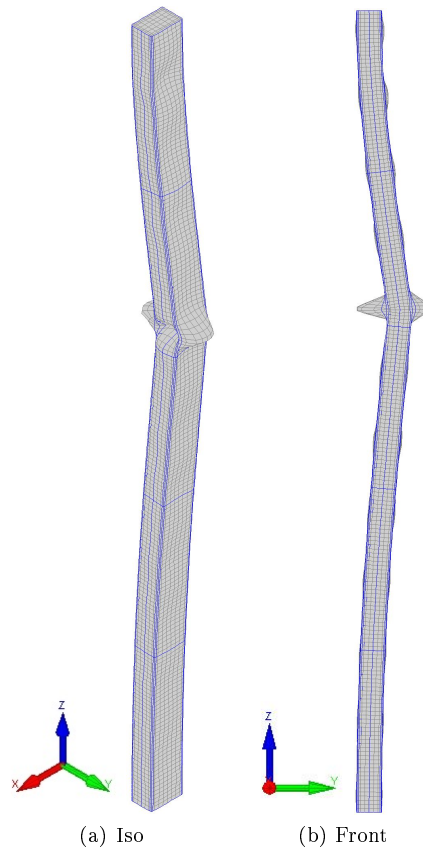


Figure 3.24: RHS 2500mm - model 4 : failure mode



Figure 3.25: RHS 2500mm - test in fire - failure mode

The mean temperature in the furnace is 722.1°C when it fails out, which is rather close to the mean temperature at which the column reached the failure during the test, 712.2°C . The thermal gradient is seen to have a major influence both on the failure mode and the temperature of failure.

Model 5 : influence of the material law

This fifth model is the same than the previous one, but the material properties used are different. In the fourth model, the material properties used are the measured ones ($f_{0.2p}$ and f_u) while in this model, f_u is determined so as to minimize the difference between the measured $\sigma - \varepsilon$ curve and the $\sigma - \varepsilon$ curve obtained with the modified Ramberg-Osgood model recommended in EN 1993-1-2, as discussed in SECTION 3.2.1. The value of f_u used in this model is equal to 533.92 MPa and the other parameters are the same than those used in model 4 (see TABLE 6.4).

The failure mode obtained is the same than in all the other models using thermal gradient (see FIGURE 3.24). Introducing the fitted parameters does not influence a lot the results, because the mean failure temperature decreases from 722.9°C with the measured properties (model 4) to 722.5°C with the fitted properties. Thus, introducing fitted material properties seems not to have a significant influence. Therefore, we will keep using the measured material properties in the next models.

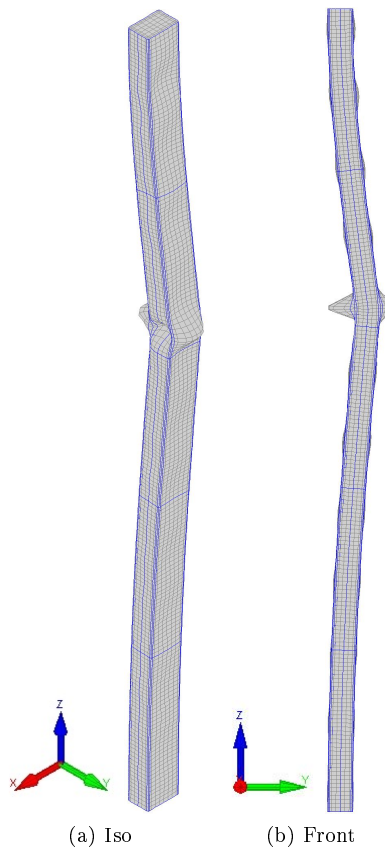


Figure 3.26: RHS 2500mm - model 5 : failure mode

Model 6 : influence of the thermal insulation at both ends

During the test, a thermal insulation was used at both ends of the column. Thus, a thermal insulation is introduced at both ends of the column in the sixth finite element model. In this case, in order to study the influence of such a brutal thermal gradient, a constant temperature of 20°C is imposed at both ends. In fact, the temperature at both ends is higher than 20°C , but the aim of this model is to demonstrate that even if we consider an extreme insulation, the effect on the failure temperature is almost negligible. The values of the parameters used in this sixth model are given in Annex (TABLE 6.5).

The failure temperature obtained with this model increases from 722.9°C without insulation to 724.4°C with insulation. It can also be noticed that the axial thermal displacement is reduced in the model with thermal insulation at both ends, due to the reduction of the heated length of the column.

As mentioned above, this model is an extreme situation because, in fact, the temperature at both ends is higher than 20°C during the test. Hence the real influence of this insulation at both ends is smaller than that observed with this idealized model. Given the weak influence of the thermal insulation at both ends, the next models will be performed without thermal insulation at the column ends.

FIGURE 3.27c illustrates the modelled thermal insulation at the column end. It results in a discontinuity of the horizontal thermal dilatation of the column.

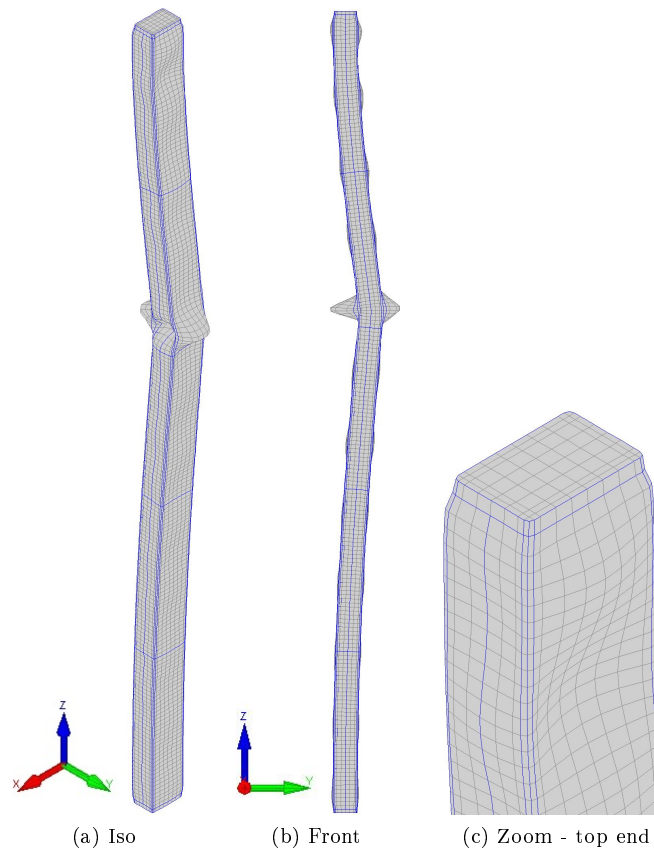


Figure 3.27: RHS 2500mm - model 6 : failure mode

Model 7 : influence of the residual stresses

This model has the same properties than the model four, but residual stresses are introduced into the numerical model. The residual stresses distribution has been discussed in section 3.4 and this distribution is used in this model. The values of the parameters used in this model seven are given in Annex (TABLE 6.6).

The failure mode obtained is the same than without residual stresses. The failure temperature (722.5°C) is a little higher than that obtained with the fourth model (722.1°C) . Therefore it can be said that introducing residual stresses does not have a significant influence. Consequently, the residual stresses will not be used in the next finite element models.

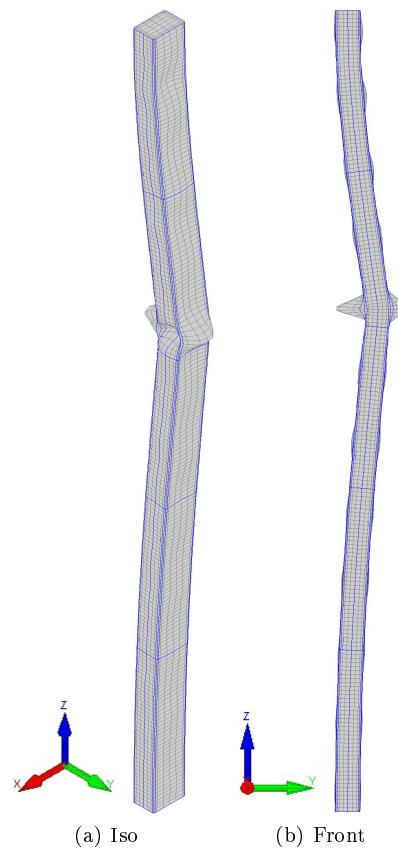


Figure 3.28: RHS 2500mm - model 7 : failure mode

Model 8 : influence of a 2D thermal analysis

A last model is performed with the same properties than the fourth model in order to study the influence of the 2D thermal analysis, described in SECTION 3.5. The values of the parameters used in this last model are given in Annex (TABLE 6.7).

The failure mode obtained is the same than in the models with thermal gradient. However, the mean failure temperature in the furnace decreases to $705.3^{\circ}C$, which is closer to the temperature reached during the test ($712.2^{\circ}C$).

Therefore, it can be said that a better representation of the temperature distribution in the cross-section leads to relatively significantly different results, closer to the tests results.

FIGURE 3.29 illustrates the failure mode which is made of a combination of local buckling and global flexural buckling around the weak axis.



Figure 3.29: RHS 2500mm - model 8 : failure mode

Conclusion

From this analysis, it can be concluded that :

- The thermal gradient has a significant influence in the numerical model both on the failure mode shape and time/temperature at failure.
- Taking into account the temperature distribution in the cross-section (2D thermal analysis) has also a quite important influence especially on the temperature at failure.
- The ratio between the mean failure temperature reached with the numerical model eight and this mean temperature when the failure did occur during the test is very close to the unity.

$$\frac{T_{failure,model}}{T_{failure,test}} = \frac{705.3}{712.2} = 0.99$$

- Strength enhancement in corners and the column ends insulation were not taken into account and may have a beneficial effect which would lead to a better result.

3.7.2 SHS 3000mm

The same work than that performed for the rectangular hollow section column has been performed for the square hollow section column. The results of the intermediate steps are provided in Annex and the influence of the parameters is summarized in TABLE 3.11. Finally, the model which contains the main parameters is presented.

Parameters	Mean failure T°	Failure mode	Significant influence?
Global imperfection	739.8°C	symmetrical	-
Local imperfection	737.4°C	symmetrical	not negligible
Curved corners	735.8°C	symmetrical	not negligible
Thermal gradient (1D)	733.4°C	similar to that of the test	yes
Material law (fitted)	733.3°C	similar to that of the test	no
Thermal insulation at both ends	733.9°C	similar to that of the test	no
Residual stresses	733.6°C	similar to that of the test	no
2D thermal analysis	713.0°C	similar to that of the test	yes

Table 3.11: SHS 3000mm - Influence of the parameters

In this final model, curved corners are modelled (with two elements per corner), both local and global imperfections are used and the geometrical and material properties used are the measured ones. The temperature evolutions, determined through the 2D thermal analysis, is introduced in the structural model. The parameters of this model eight are available in TABLE 3.12.

FIGURE 3.30 shows also that the failure mode shape obtained numerically is close to that observed during the fire test (see FIGURE 2.11). The failure mode consists in a combination of local buckling and global flexural buckling mainly about the x-axis, due to the horizontal thermal gradient. The hinges are located near the top of the column, due to the non negligible difference of temperature between the top and the bottom of the column.

The mean gases temperature when failure occurs is equal to 713.0°C. This mean failure temperature is close to the mean failure temperature recorded during the test (i.e. 715.6°C).

b	h	L	r_i	r_e	t	E_0	$f_{y,flat}$	$f_{y,corner}$	f_u
[mm]	[mm]	[mm]	[mm]	[mm]	[mm]	$\left[\frac{N}{mm^2}\right]$	$\left[\frac{N}{mm^2}\right]$	$\left[\frac{N}{mm^2}\right]$	$\left[\frac{N}{mm^2}\right]$
79.6	79.2	3000	4	6.87	2.87	220000	411.77	441.4	588.4
<i>Corner type</i>		<i>Material law</i>		<i>Thermal gradient</i>		<i>End insulation</i>		$\sigma_{residual}$	
[-]		[-]		[-]		[-]		[-]	
<i>Curved</i>		<i>R - O (measured)</i>		18 zones		/		/	
<i>FE type</i>		<i>NG</i>	<i>NL</i>	<i>Nb</i>	<i>Nh</i>	<i>Nc</i>	N_{axial}	Δ	δ
[-]		[-]	[-]	[-]	[-]	[-]	[kN]	[mm]	[mm]
1 st degree		4	240	4	4	2	-72	$0.8 \frac{L}{750}$	$0.8 \times 0.008 \times b$ $0.8 \times 0.01 \times h$

Table 3.12: SHS 3000mm - Finite element model

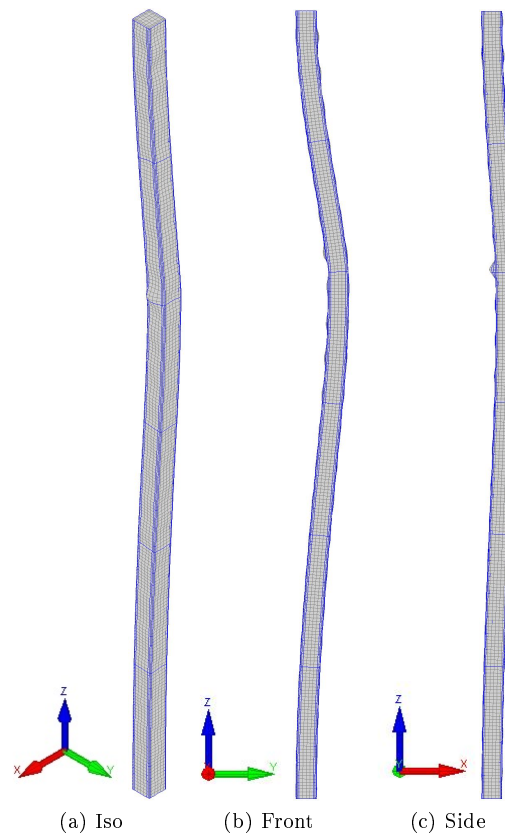


Figure 3.30: SHS 3000mm - Finite element model : failure mode

Conclusion

The same conclusions as those from the previous analysis can be drawn :

- The thermal gradient has a significant effect on both the mean failure temperature and the failure mode shape.
- The use of the 2D thermal analysis led up to a reliable finite element model able to predict the fire resistance of the tested column (Failure temperature).
- The ratio between the mean failure temperature obtained with the finite element model using the 2D thermal analysis and that obtained during the test is very close to the unity :

$$\frac{T_{failure,model}}{T_{failure,test}} = \frac{713.0}{715.6} = 0.996$$

- The low underestimation of the failure temperature can be explained by the fact that the strength enhancement in corners was not taken into account, but also by the column ends insulation which has been neglected.

3.7.3 SHS 2500mm

For this last column, only the final finite element model is presented. The parameters used are presented in TABLE 3.13. It is the model made of curved corners with two elements per corner, where the local and global initial geometrical imperfections are taken into account. The material and geometrical

properties are the measured ones, and the temperature distribution is based on the 2D thermal analysis.

Similarly to the two previous columns, the failure mode shape obtained numerically (see FIGURE 3.31) is close to that observed during the fire test (see FIGURE 2.17). Moreover, the mean temperature in the furnace obtained numerically at failure ($712.2^{\circ}C$) is close to that recorded at the end of the fire test ($714.2^{\circ}C$). The ratio between the mean failure temperature obtained with the finite element model and the mean temperature recorded during the test is, similarly to the two previous tests, close to the unity :

$$\frac{T_{failure,model}}{T_{failure,test}} = \frac{712.2}{714.2} = 0.997$$

The conclusion of the numerical modelling of this third column is that the use of the parameters highlighted in the two previous numerical modelling leads directly to a good numerical prediction of the column behaviour during the fire test.

b	h	L	r_i	r_e	t	E_0	$f_{y,flat}$	$f_{y,corner}$	f_u
[mm]	[mm]	[mm]	[mm]	[mm]	[mm]	$\left[\frac{N}{mm^2}\right]$	$\left[\frac{N}{mm^2}\right]$	$\left[\frac{N}{mm^2}\right]$	$\left[\frac{N}{mm^2}\right]$
		2500	4			220000			
<i>Corner type</i>		<i>Material law</i>			<i>Thermal gradient</i>		<i>End isolation</i>	$\sigma_{residual}$	
[-]		[-]			[-]		[-]	[-]	
<i>curved</i>		<i>R - O (EN1993 - 1 - 2)</i>			15 zones		/	/	
<i>FE type</i>	<i>NG</i>	<i>NL</i>	<i>Nb</i>	<i>Nh</i>	<i>Nc</i>	<i>N_{axial}</i>	Δ	δ	
[-]	[-]	[-]	[-]	[-]	[-]	[kN]	[mm]	[mm]	
1 st degree	4	150	4	4	2	-78	$0.8 \frac{L}{750}$	$0.8 \times 0.008 \times b$ $0.8 \times 0.01 \times h$	

Table 3.13: SHS 2500mm - Finite element model

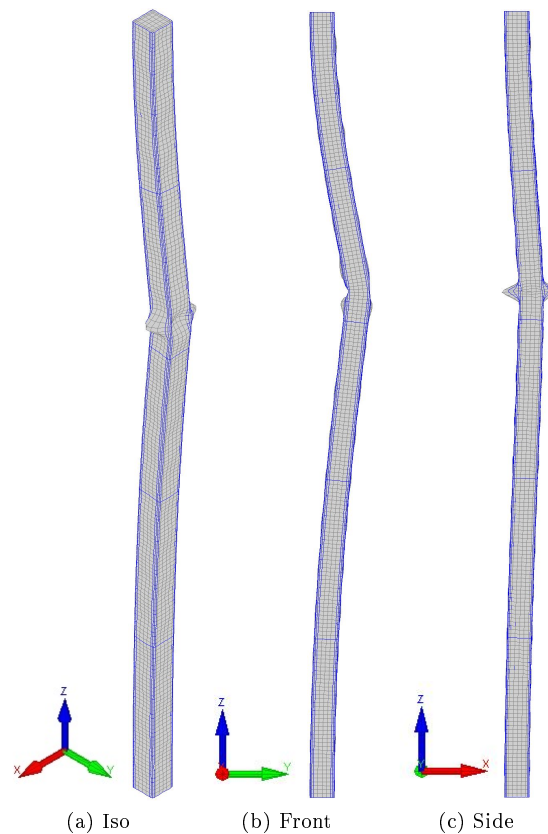


Figure 3.31: SHS 2500mm - Finite element model : failure mode

3.7.4 Conclusions

To conclude this finite element calibration section, it is important to remember the main parameters and their relative influence on the results.

Parameters like the residual stresses, the column ends insulation or the use of fitted material properties do not have an significant influence on the results and will be neglected.

Conversely, the measured material and geometrical properties were used, and the curved corners were modelled. Indeed, the influence on the results of the measured and geometrical properties is important. However, the use of curved corners does not have a significant influence, but this choice was based on the fact that when curved corners are used, the cross-section behaviour is closer to the real one. Indeed, the area and the inertia are almost equal to the actual ones when curved corners are modelled, and the buckling lengths of the flats are also closer to the actual ones.

Finally, the most important parameters in order to obtain a good prediction of the fire resistance of the tested columns are the temperature distribution and the vertical and horizontal thermal gradients. This section has also shown the importance of the 2D thermal analysis in comparison to the simple 1D thermal analysis, and thus the importance of the thermal conductivity across the cross-section and the thermal radiation of the internal faces of the box.

Moreover, the low underestimation of the mean failure temperature can be explained by the fact that the strength enhancement of corner regions has not be taken into account in the numerical model. Further, it has also be shown that the insulation of both ends has a beneficial effect on the mean failure temperature.

Chapter 4

Buckling curve - parametric analysis

The first part of this work consisted in modelling the fire test. Therefore, the loading conditions used during the tests were implemented into the numerical model. Hence, a load was applied at the bottom of the column and was maintained constant during the test while the temperature was increasing until it fails out.

In the second part of this work, several numerical simulations will be performed in order to obtain a number of points in the graph *Failure load – Length of the column*. The aim of this part of the work is to compare the results obtained numerically to those obtained when using EN 1993-1-2 - Annex C or other proposals made to predict the failure load. However, in order to obtain the failure loads for different temperatures, the type of numerical simulation has to change. Indeed, the temperature has to be constant while the load increases until failure occurs.

4.1 Comparison of both types of simulation

The numerical calibration has shown that the finite element model was able to predict the fire behaviour of the tested columns when the applied load remains constant and the temperature increases. Thus, the aim of the first step of the parametric analysis is to show that both types of loading condition lead to the same results and that the results obtained numerically are reliable.

4.1.1 Constant load and varying temperature

The first type of simulation is that developed in order to calibrate the numerical model on the tests (see CHAPTER 3). The evolution of load and temperature across time is shown in FIGURE 4.1.

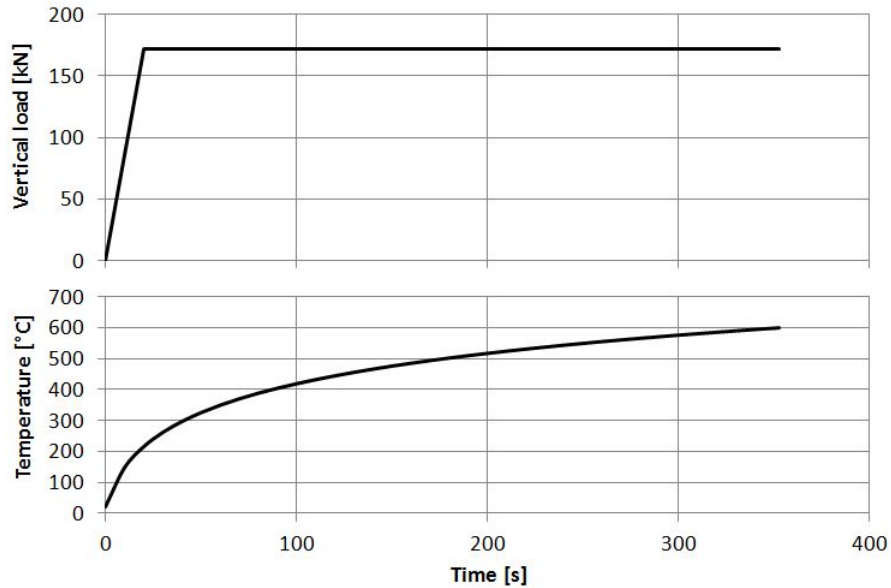


Figure 4.1: First type of simulation : Constant load and varying temperature

4.1.2 Varying load and constant temperature

In the second type of simulation, the goal is to obtain a failure load for several column slenderness and a certain number of temperature. The evolution of load and temperature with time is shown in FIGURE 4.2.

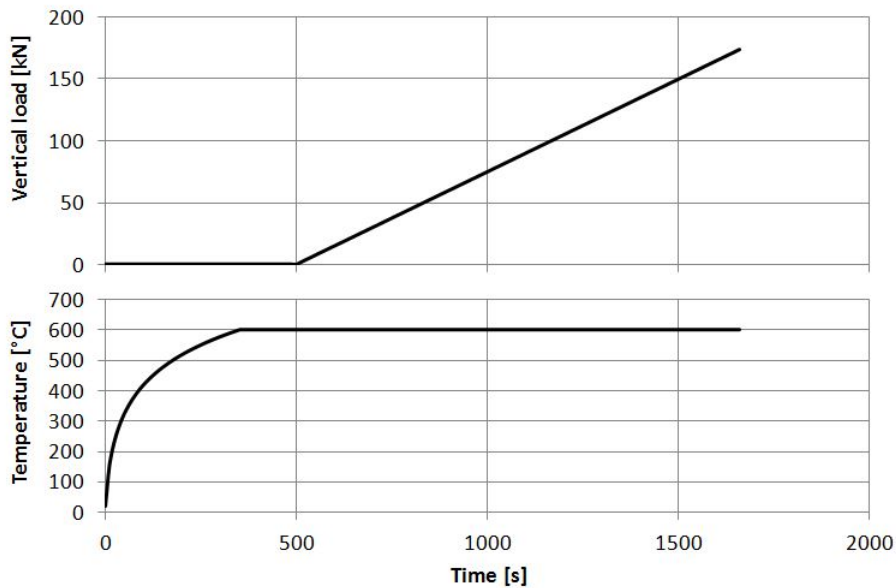


Figure 4.2: Second type of simulation : Varying load and constant temperature

4.1.3 Conclusion

The second type of simulation was performed with a constant temperature of $600^{\circ}C$ and the failure occurs for a vertical load equal to $172.1kN$. Then the second type of simulation was performed using a constant vertical load equal to that obtained with the previous simulation (i.e. $172.1kN$) and failure occurs for a temperature equal to $600^{\circ}C$. Moreover both type of simulations lead to the same failure mode. Thus it can be said that both models are equivalent and that the parametric analysis can be achieved using the second type of simulation.

4.2 Finite element model for the parametric analysis

4.2.1 Boundary conditions

In the numerical model, columns are free in rotation about the weak axis at both ends. The vertical displacement at the loaded end is free in order to permit the thermal elongation and the contraction due to the vertical compressive load while this vertical displacement is blocked at the other end. Horizontal displacement are also free at both ends, in order to permit the thermal dilatation of the end plates. The boundary conditions of this model are illustrated in FIGURE 4.3.

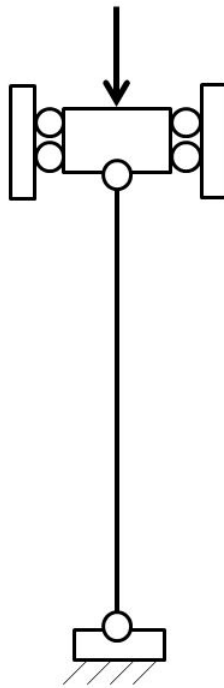


Figure 4.3: Boundary conditions

FIGURE 4.4 shows the boundary condition used into the software SAFIR to model the boundary conditions presented in FIGURE 4.3. Blue arrows illustrate the blocked rotational degrees of freedom and red arrows illustrate the blocked translational degrees of freedom. Thus only the rotation about the weak axis is allowed and all the translational displacements are allowed, except the horizontal displacement of the center of the top plate which is blocked. Moreover, horizontal displacement of the center of each side were blocked by symmetry of the thermal dilatation.

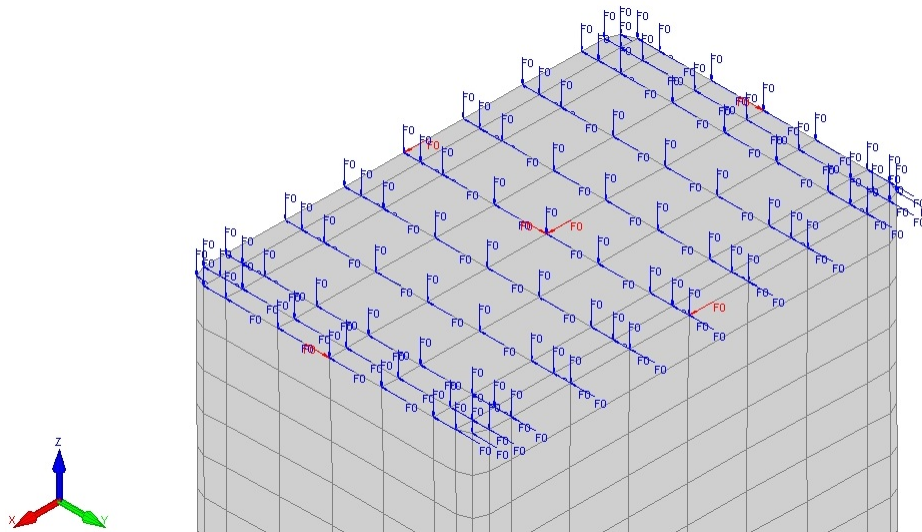


Figure 4.4: Boundary conditions - Numerical model

Similarly to the calibration part, a 100mm thick plate is used at both ends of the column. The plate at the top of the column is used to transmit the punctual vertical load to the column without introducing local buckling due to the punctual loading, and the plate at the bottom is used to permit the rotation movement of the column about the weak axis.

4.2.2 Geometrical properties

Nominal geometrical properties are used in the parametric analysis and curved corners are also taken into account in the numerical model.

The dimensions of the studied cross-sections are presented in TABLE 4.1, with their cross-section classification at ambient temperature.

Name	b	h	t	Class at ambient temperature
$120 \times 80 \times 3$	80	120	3	4
$80 \times 80 \times 3$	80	80	3	2
$80 \times 80 \times 6$	80	80	6	1
$150 \times 150 \times 3$	150	150	3	4

Table 4.1: Studied cross-sections - Parametric analysis

4.2.3 Material properties

During the calibration part of the work, measured material properties were used in the numerical model and it is known that these material properties take the material strength enhancement into account. Thus, during this parametric study, the results obtained while using nominal material properties will be compared to those obtained using enhanced material properties for the rectangular cross-section. Rossi (Rossi et al. [2013]) has proposed a model to predict the strength enhancement properties of flats and corners regions from the nominal properties. The nominal material properties used are those recommended by the European code EN 10088-4 and are presented in TABLE 4.2. The enhanced material properties are given in TABLE 4.3 for the rectangular $120 \times 80 \times 3$ cross-section.

Material properties	$f_{y,flat}$	$f_{y,corner}$	f_u
	<i>MPa</i>	<i>MPa</i>	<i>MPa</i>
Nominal properties	280	280	450

Table 4.2: Material properties(EN 10088-4)

Material properties	$f_{y,flat}$	$f_{y,corner}$	f_u
	<i>MPa</i>	<i>MPa</i>	<i>MPa</i>
Enhanced properties	308.36	375.38	450

Table 4.3: Enhanced material properties : $120 \times 80 \times 3$

4.2.4 Initial geometrical imperfections

Usually, in numerical models, equivalent geometrical imperfections are used. These equivalent imperfections take into account both the geometrical and the material imperfections. However, the values proposed in the European code have been determined for carbon steel columns and they may not well be adapted for stainless steel.

Presently, the following global and local geometrical imperfections were introduced in the model.

Global initial geometrical imperfection

The same global geometrical imperfection than that used during the calibration chapter is used. It is a global geometrical imperfection equal to 80 percents of the geometrical tolerances (i.e. $L/750$ for hollow section columns (EN 1090-2)). Thus, this amplitude is equal to $L/937.5$.

Local initial geometrical imperfection

The local imperfections used are equal to 80 percents of the geometrical tolerance as well. The straightness tolerance of hollow section is equal to 1 percent of the width of the flats, as recommended in EN 1090-2.

4.2.5 Temperature distribution and evolution

In the parametric analysis, the ISO 834 heating curve is directly applied to the entire column, without performing any thermal analysis. Hence, in this idealized model, there is no thermal gradient between the bottom and the top or between the front and the back of the furnace. Thus the results obtained with those numerical models can directly be compared to results obtained with EN 1993-1-2.

4.2.6 Cross-section classification

The cross-section used have been presented in TABLE 4.1. Their cross-section classification is given for the different formula of ε described in SECTION 1.3.3. TABLE 4.4 gives the values of the material factor, TABLE 4.5 provides the cross-section slenderness according to the expression of the material factor used, and finally TABLE 4.6 gives the cross-section classification according to the expression of the material factor used. The limit of each Class is remembered in TABLE 4.7.

It is interesting to remember that, in order to not over-predict the resistance of an element, it is recommended that cross-section that are Class 4 at room temperature cannot be promoted beyond Class 3 at elevated temperature (Ng and Gardner [2007]). Therefore, cross-sections $120 \times 80 \times 3$ and $150 \times 150 \times 3$ remains Class 3 cross-sections at $800^\circ C$, even if the ratio $\frac{c/t}{\varepsilon}$ is smaller than the limit of the Class 1 (i.e. $\frac{c/t}{\varepsilon} = 25.7$).

The TABLE 4.6 highlights the differences between the cross-section classification, especially for the $80 \times 80 \times 3$ cross-section which can be a Class 4 cross-section according to the cross-section classification recommended by the European code EN 1993-1-2. The cross-section can also be a Class 2 according to the cross-section classification at room-temperature and with the cross-section classification at elevated temperature, this section can either be Class 1, 2 or 3, depending on the temperature.

ε	$0.85 \left[\frac{235}{f_y} \right]^{0.5}$	$\left[\frac{235}{f_y} \frac{E}{210000} \right]^{0.5}$	$0.85 \left[\frac{235}{f_y} \frac{E}{210000} \right]^{0.5}$	$\left[\frac{235}{f_y} \frac{E}{210000} \frac{k_{E,\theta}}{k_{y,\theta}} \right]^{0.5}$		
	$\forall Temperature$	$\forall Temperature$	$\forall Temperature$	$200^\circ C$	$500^\circ C$	$800^\circ C$
$\forall Cross - section$	0.7787	0.9377	0.797	0.8994	0.9377	2.0642

Table 4.4: Material factors : ε

ε	$0.85 \left[\frac{235}{f_y} \right]^{0.5}$	$\left[\frac{235}{f_y} \frac{E}{210000} \right]^{0.5}$	$0.85 \left[\frac{235}{f_y} \frac{E}{210000} \right]^{0.5}$	$\left[\frac{235}{f_y} \frac{E}{210000} \frac{k_{E,\theta}}{k_{y,\theta}} \right]^{0.5}$		
	$\forall Temperature$	$\forall Temperature$	$\forall Temperature$	$200^\circ C$	$500^\circ C$	$800^\circ C$
$80 \times 80 \times 3$	31.68	26.31	30.94	27.43	26.31	11.95
$120 \times 80 \times 3$	48.80	40.53	47.68	42.25	40.53	18.41
$80 \times 80 \times 6$	14.55	12.09	14.22	12.60	12.09	5.49
$150 \times 150 \times 3$	61.64	51.19	60.22	53.37	51.19	23.25

Table 4.5: Cross-section classification : $\frac{c/t}{\varepsilon}$

ε	$0.85 \left[\frac{235}{f_y} \right]^{0.5}$	$\left[\frac{235}{f_y} \frac{E}{210000} \right]^{0.5}$	$0.85 \left[\frac{235}{f_y} \frac{E}{210000} \right]^{0.5}$	$\left[\frac{235}{f_y} \frac{E}{210000} \frac{k_{E,\theta}}{k_{y,\theta}} \right]^{0.5}$		
	$\forall Temperature$	$\forall Temperature$	$\forall Temperature$	$200^\circ C$	$500^\circ C$	$800^\circ C$
$80 \times 80 \times 3$	4	2	4	3	2	1
$120 \times 80 \times 3$	4	4	4	4	4	3
$80 \times 80 \times 6$	1	1	1	1	1	1
$150 \times 150 \times 3$	4	4	4	4	4	3

Table 4.6: Cross-section classification

	$\frac{c/t}{\varepsilon}$
Class 1	< 25.7
Class 2	< 26.7
Class 3	< 30.7

Table 4.7: Cross-section classification : limit values of the ratio $\frac{c/t}{\varepsilon}$

4.2.7 Tests results

During the parametric analysis, four kind of cross-sections will be studied, for nine column's length¹ ranging between $100mm$ and $6000mm$ and at three temperatures ($200^\circ C$, $500^\circ C$ and $800^\circ C$).

In addition to the study of these cross-sections at $200^\circ C$, $500^\circ C$ and $800^\circ C$, a cross-section will be studied at $600^\circ C$ and $700^\circ C$.

¹The vertical discretization used is 10 elements/100mm.

It is worth noting that during the parametric analysis, the results obtained for temperatures above 700°C did not seem to have reached the failure mode. Therefore, it is difficult to determine if the real failure of the column is about to occur in the few seconds which follow the end of the calculation, or if a numerical divergence leads to the end of the computation well before the actual failure of the column. Therefore, these results will be treated with caution in the next paragraphs.

$120 \times 80 \times 3$ Cross-section

FIGURES 4.5, 4.6 and 4.7 provide a comparison between the numerical results and the predictive bearing capacity at elevated temperature determined with the proposed models described in SECTION 1.3.

For temperatures equal to 200°C and 500°C , the models recommended by the European code EN 1993-1-2 and by Lopes (Lopes et al. [2012]) are safe. The model proposed by Euro Inox (Euro-Inox [2002]) is also always safe, except for $L < 1000\text{mm}$. The model proposed by Ng and Gardner (Ng and Gardner [2007]) fits well the numerical results for column lengths longer than 2000mm , but the predictions are unsafe for columns shorter than 2000mm . The other models overestimate the fire resistance of the numerical results, resulting in a unsafe bearing capacity prediction.

For temperature equal to 800°C , the numerical result corresponding to the column of 3000mm is out of the general trend of the other results (certainly due to convergence problems). The FIGURE 4.7 shows that all the models seem unsafe for member lengths longer than 1000mm . However the convergence of the numerical models is still under question and therefore, those results will not be taken into consideration herein.

It can nevertheless be observed that the model proposed by Lopes has the same trend that the numerical results.

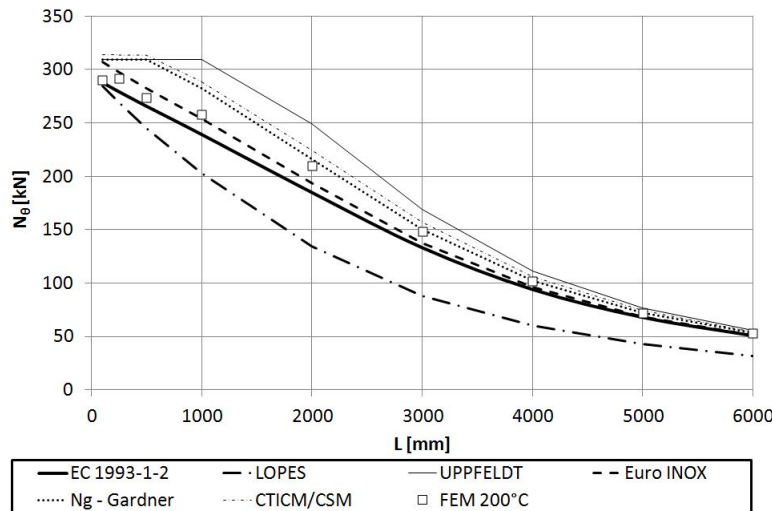
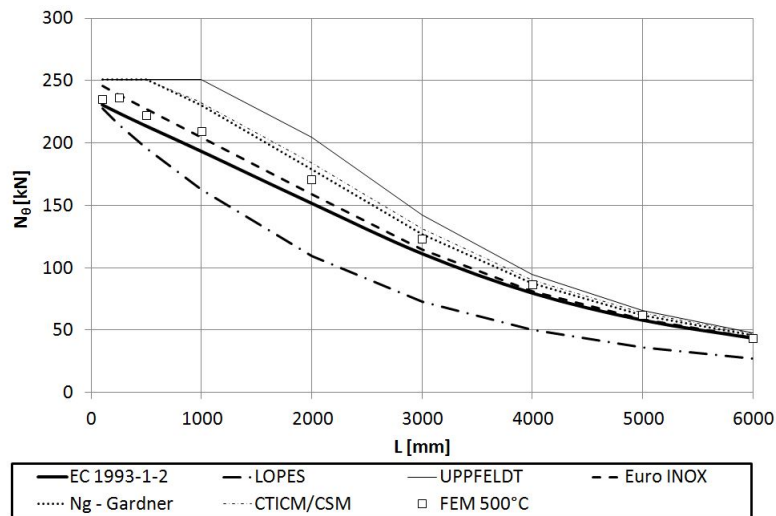
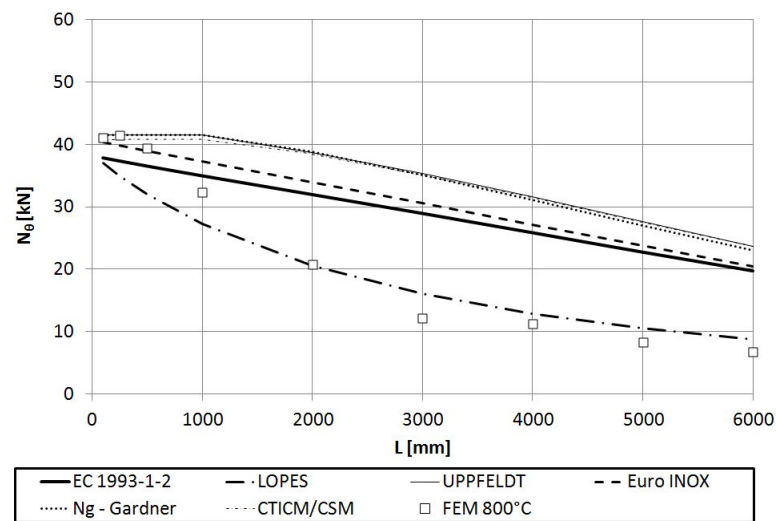


Figure 4.5: $120 \times 80 \times 3$: Numerical results versus theoretical predictions for 200°C

Figure 4.6: $120 \times 80 \times 3$: Numerical results versus theoretical predictions for 500°C Figure 4.7: $120 \times 80 \times 3$: Numerical results versus theoretical predictions for 800°C

$80 \times 80 \times 3$ Cross-section

A comparison between the numerical results and the predictive bearing capacity at elevated temperature determined with the proposed models can be made using FIGURES 4.9, 4.10 and 4.11 for the square hollow section $80 \times 80 \times 3$.

Similar observations than that made for the rectangular cross-section columns can be made for this column.

At 200°C and 500°C , The models proposed by the European code EN 1993-1-2 and by Lopes are safe.

The model proposed by Euro Inox, which was safe for the $120 \times 80 \times 3$ cross-section column at $200^\circ C$ and $500^\circ C$, is unsafe at the same temperature for the square hollow section when considering columns shorter than $3000mm$. It is due to the fact that Euro Inox performs the cross-section classification at ambient temperature. According to that cross-section classification, the studied cross-section is Class 2 in the model proposed by Euro Inox. Hence, it is supposed that local buckling will not occur and that the cross-section is fully efficient. However, FIGURE 4.8, which illustrates the failure mode of the studied square hollow section column, shows that local buckling occurs. Therefore, the local buckling reduces the bearing capacity of the column, and the numerical fire resistance is smaller than that predicted by Euro Inox. Conversely, the cross-section classification performed in the model recommended by the European code and in that proposed by Lopes lead to a Class 4 cross-section. Thus, the effective cross-section is determined and the predictive bearing capacity remains safe.

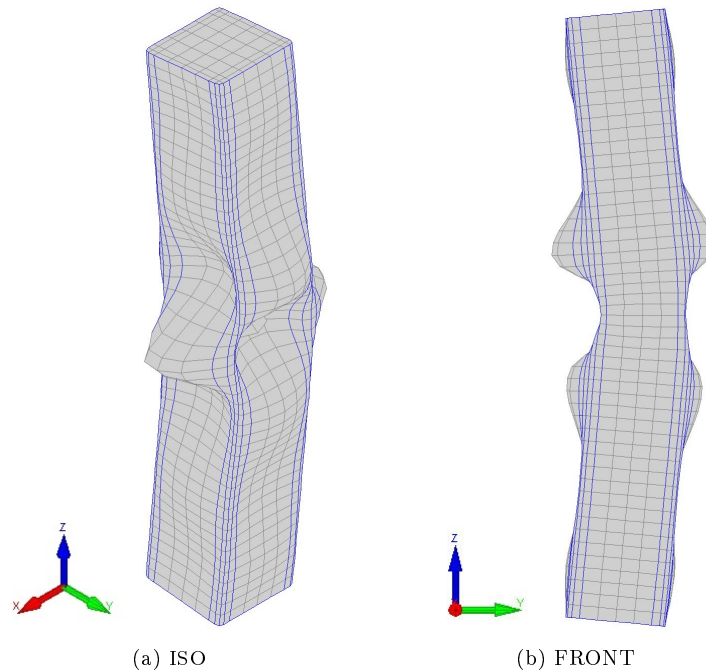


Figure 4.8: $80 \times 80 \times 3$ cross-section at $500^\circ C$ for $L = 500mm$: Failure mode

At $800^\circ C$, once again, the curve proposed by Lopes seems to have a well-adapted trend, but nothing can be concluded due to convergence problems. However, let's note that the result which corresponds to a column length of $2000mm$ does not follow the general trend of the other results and that it is certain that it is due to a convergence problem.

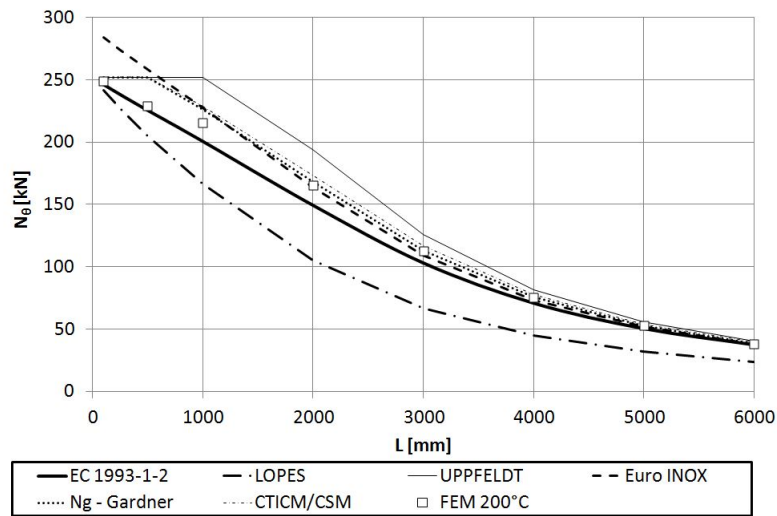


Figure 4.9: $80 \times 80 \times 3$: Numerical results versus theoretical predictions for $200^\circ C$

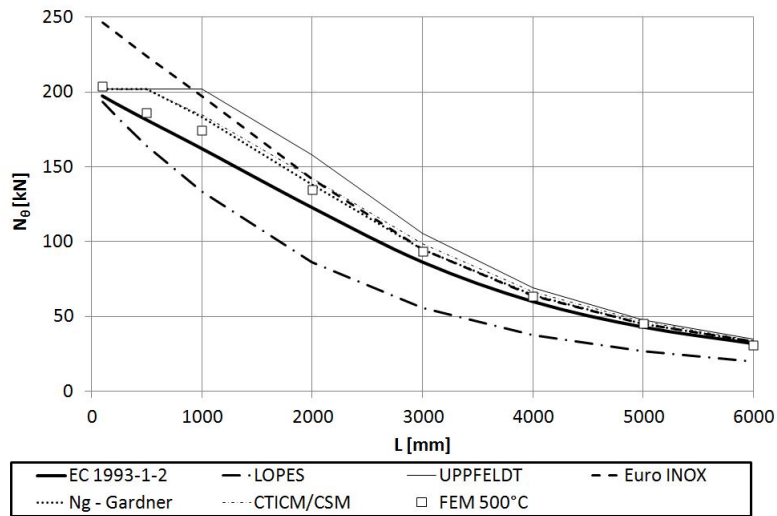


Figure 4.10: $80 \times 80 \times 3$: Numerical results versus theoretical predictions for $500^\circ C$

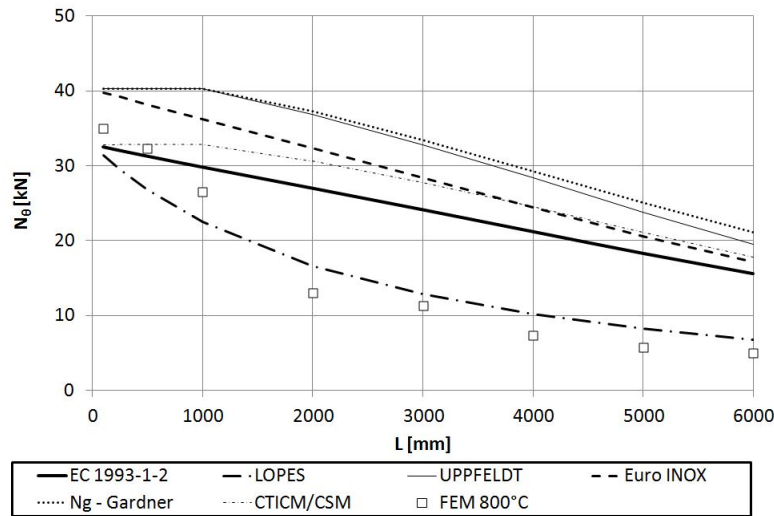
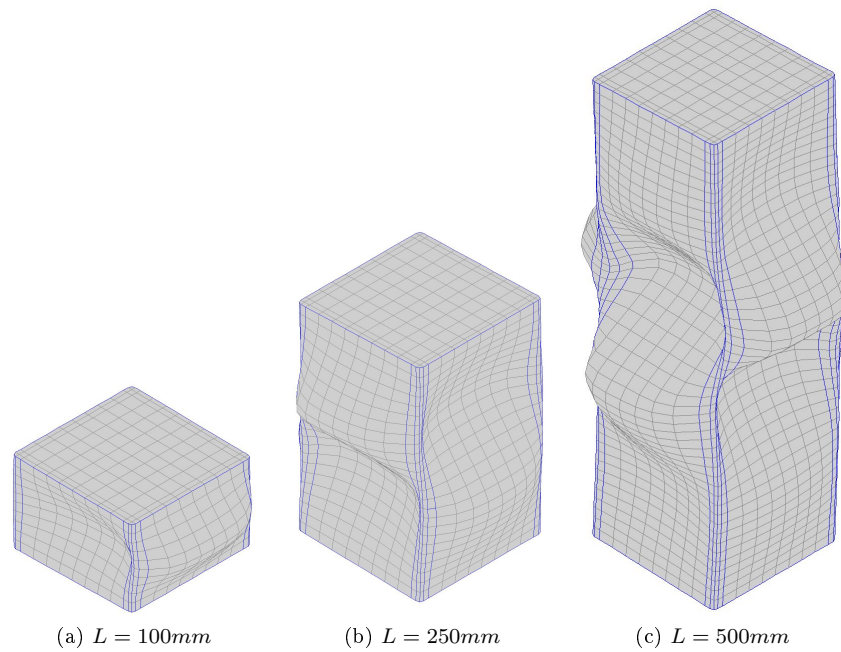


Figure 4.11: $80 \times 80 \times 3$: Numerical results versus theoretical predictions for 800°C

$150 \times 150 \times 3$ Cross section

This cross-section has a significant slenderness ($\frac{c/t}{\epsilon} = 51.2$) in comparison to the previous studied cross-sections. The comparisons between the predictive models and the numerical results for the three temperatures are given in FIGURES 4.13, 4.14 and 4.15.

On these graphs, it can be seen that, at 200°C , 500°C and 800°C , the bearing capacity of the column is almost constant for column length until nearly 2000mm . It is explained by the fact that the column fails out only by local buckling, as shown in FIGURE 4.12. Therefore, the column length have almost no influence. However, the two first point, corresponding to $L = 100\text{mm}$ and $L = 250\text{mm}$, have a higher failure load. It can be explained by the stain hardening of the material. It would result in a stress higher than the yield strength in the cross-section, which leads to a higher resistance of the cross-section.

Figure 4.12: $150 \times 150 \times 3$ - Failure modes

At 200°C and 500°C , the model recommended by the European code is safe for columns longer than 2000mm and the model proposed by Lopes is safe for columns longer than 1000mm . The model proposed by Euro Inox is only safe for columns longer than 5000mm . The other models are all unsafe.

At 800°C , as mentioned here before, the bearing capacity of short columns is almost constant until lengths of 1000mm . Those four finite element models, corresponding to column lengths ranging between 100mm and 1000mm , did converge. Thus, that points can be taken into account. For longer columns, once again, the values obtained numerically are lower than that predicted with most of the models, but nothing can be concluded. Note that for columns shorter than 4000mm , the model proposed by Lopes is safe.

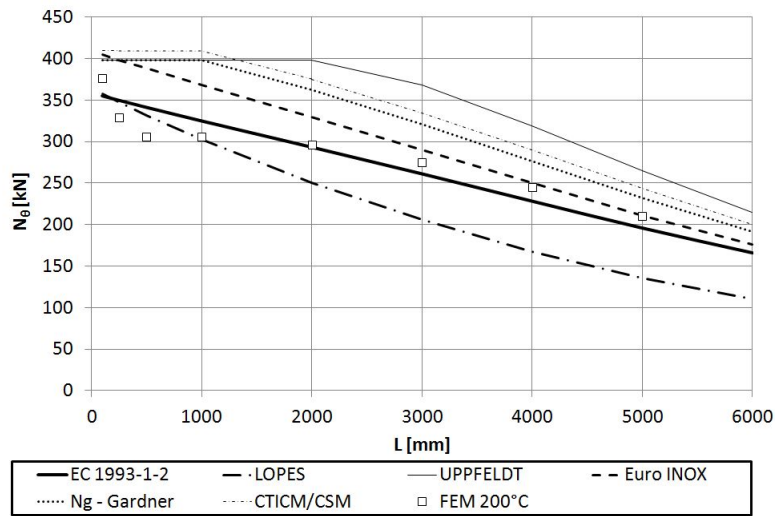


Figure 4.13: $150 \times 150 \times 3$: Numerical results versus theoretical predictions for $200^\circ C$

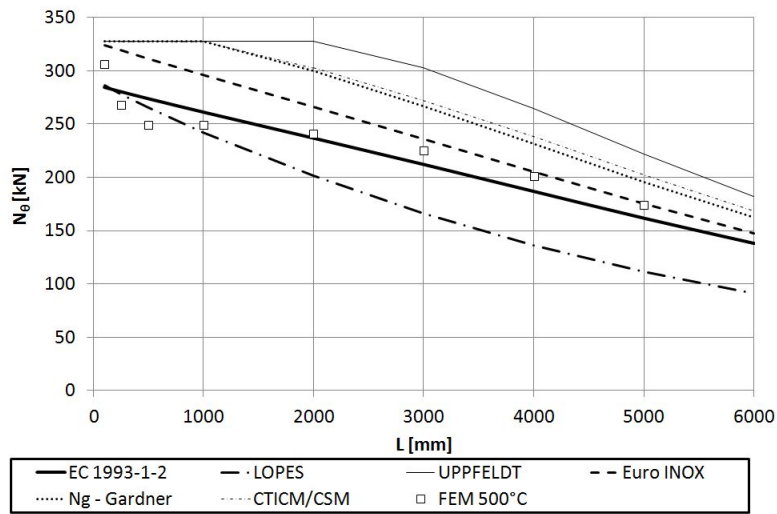


Figure 4.14: $150 \times 150 \times 3$: Numerical results versus theoretical predictions for $500^\circ C$

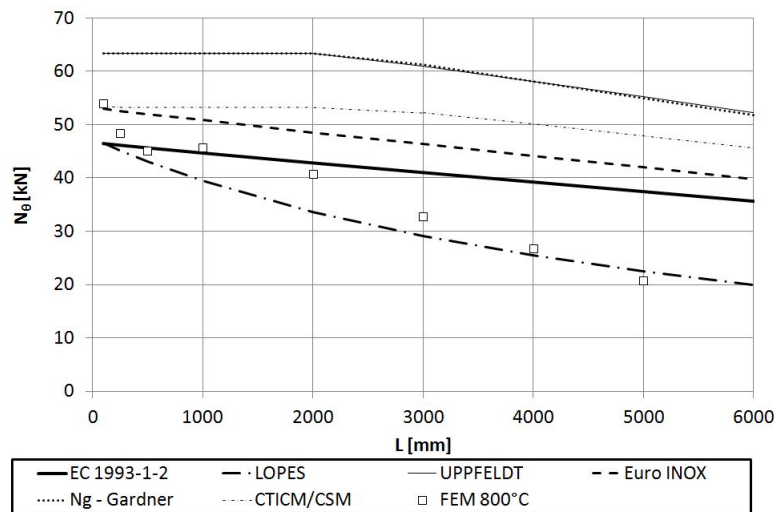


Figure 4.15: $150 \times 150 \times 3$: Numerical results versus theoretical predictions for 800°C

$80 \times 80 \times 6$ Cross-section

This cross-section is different from the three previous ones in that it is a Class 1 cross-section, whatever the formula used to determine the material parameter ε .

The European code and Euro Inox are unsafe for column's lengths shorter than 1000mm at 200°C and shorter than 2000mm at 500°C . For longer columns, those models are safe. The model proposed by Lopes is always safe, except for very short columns (shorter than 100mm) at 200°C . It can also be noticed that the model proposed by CTICM fits well the numerical results.

At 800°C , similarly to the three previous cross-sections, the curve proposed by Lopes seems to be well adapted in order to model the behaviour of ferritic columns at temperature above 500°C . However, it can yet be noticed that the numerical results corresponding to column lengths equal to 2000mm and 3000mm are out of the general trend of the other results. Therefore, the convergence problem is certain for these results.

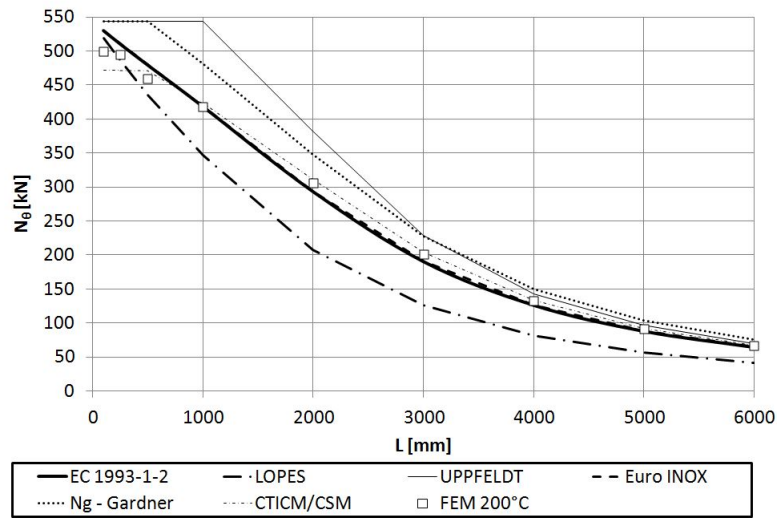


Figure 4.16: $80 \times 80 \times 6$: Numerical results versus theoretical predictions for $200^\circ C$

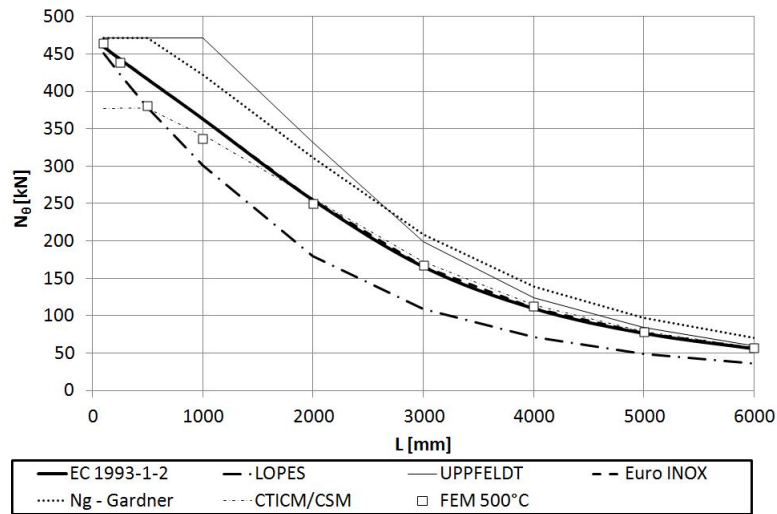


Figure 4.17: $80 \times 80 \times 6$: Numerical results versus theoretical predictions for $500^\circ C$

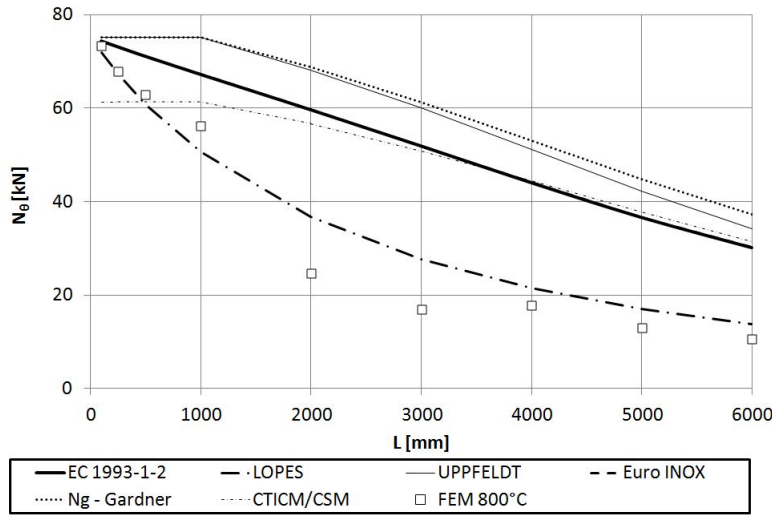


Figure 4.18: $80 \times 80 \times 6$: Numerical results versus theoretical predictions for 800°C

4.2.8 Buckling curves

In this section, the buckling curves proposed by Lopes and the European code 1993-1-2 are compared to the numerical results. The ratio between the failure load at elevated temperature (N_θ) and the maximum load which can be supported by the cross-section ($N_{Rd,\theta}$) will be plotted versus the member slenderness at elevated temperature ($\bar{\lambda}_\theta$).

$120 \times 80 \times 3$ Cross-section

Firstly, it can be observed on FIGURE 4.20a that, at 200°C and 500°C , the buckling curve proposed by the European code EN 1993-1-2 is very close to the numerical results for high column slenderness and for low column slenderness, and that this curve is more conservative for intermediate column slenderness.

It can also be observed that for temperatures above 600°C , the model recommended by the European code is no more safe. It is due to the temperature dependence of the ratio $\frac{k_{E,\theta}}{k_{0.2p,\theta}}$ of the ferritic 1.4003 grade, which is depicted in FIGURE 4.19. When temperature increases, this ratio increases, and therefore, the elevated temperature slenderness of the column decreases. Thus, due to the reduction of the slenderness, it is supposed that the ratio between the failure load and the load which can be supported by the effective cross-section increases, as modelled by the buckling curve recommended by the European code. However, the observed behaviour of the finite element models in this case is quite different. When temperature increases, the ratio between the failure load and the load which can be supported by the effective cross-section does not increase as much as supposed by the European code. This behaviour leads to an overrating of the bearing capacity of the column by EN 1993-1-2. The phenomenon described here above can be observed in FIGURE 4.20a. Indeed, the model recommended by the European code 1993-1-2 predicts the bearing capacity of the columns longer than 3000mm at 200°C and 500°C in a safely way, and becomes unsafe for the same column's lengths at 600°C . This has also been observed by Lopes (Lopes et al. [2012]).

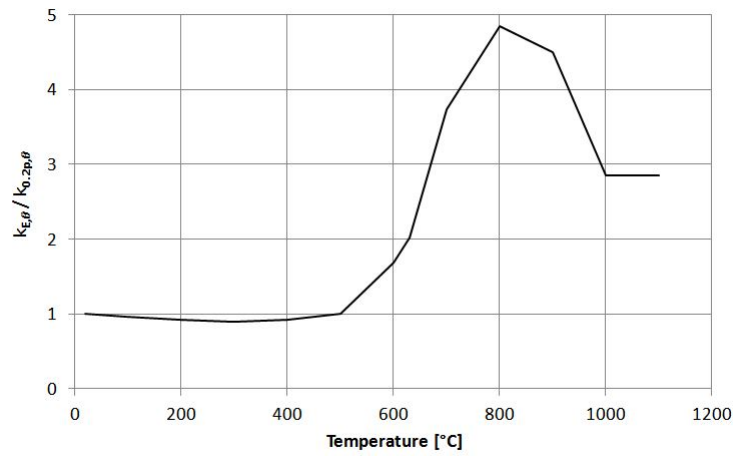
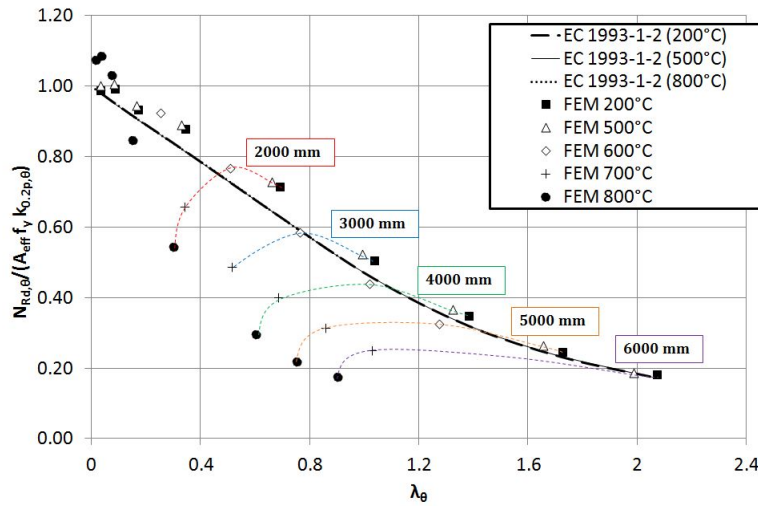
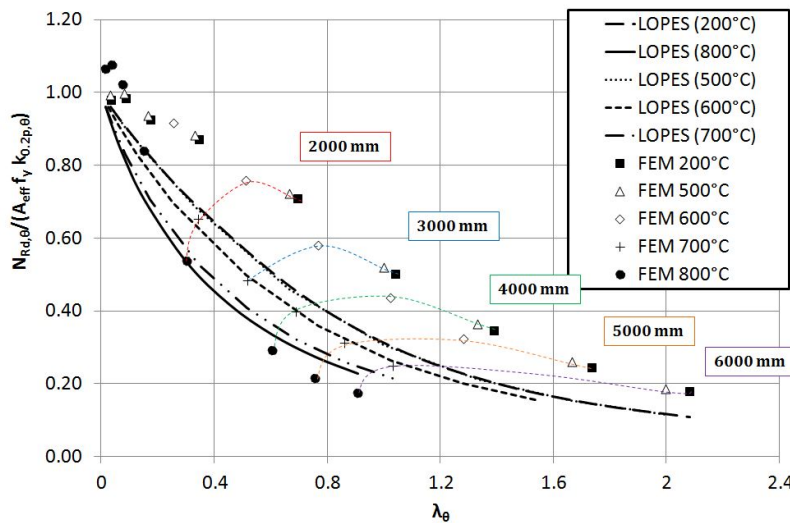
Figure 4.19: $\frac{k_{E,\theta}}{k_{0.2p,\theta}}$

FIGURE 4.20b illustrates the model proposed by Lopes. As mentioned previously, the model proposed by Lopes seems to be the best in order to model the column's behaviour at temperature above 500°C . Once again, it cannot be concluded if this model is unsafe at 800°C , due to the convergence problems. Nevertheless, it can yet been said that the model proposed by Lopes is safe for temperature until 700°C . It can also be said that the shape of the buckling curve seems well adapted.

From FIGURE 4.20b, it can also be observed that the model proposed by Lopes is too safe at temperature below 500°C .



(a) EN 1993-1-2



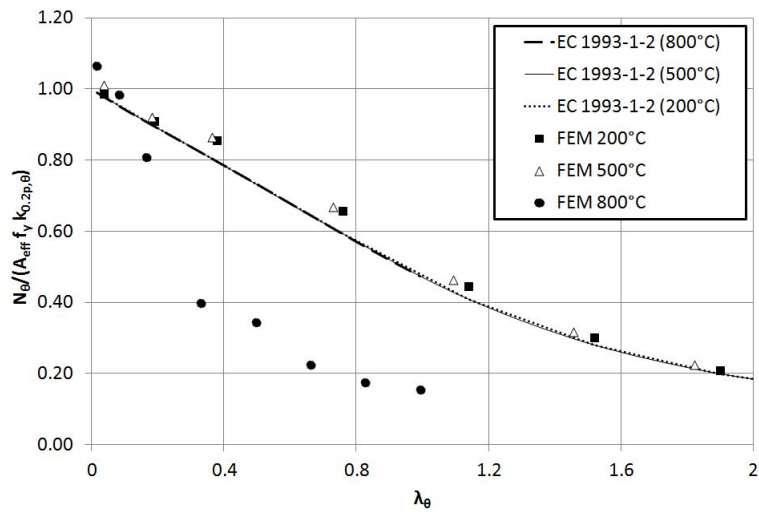
(b) Lopes

Figure 4.20: Comparison : EC1993-1-2 - Numerical results [$120 \times 80 \times 3$]

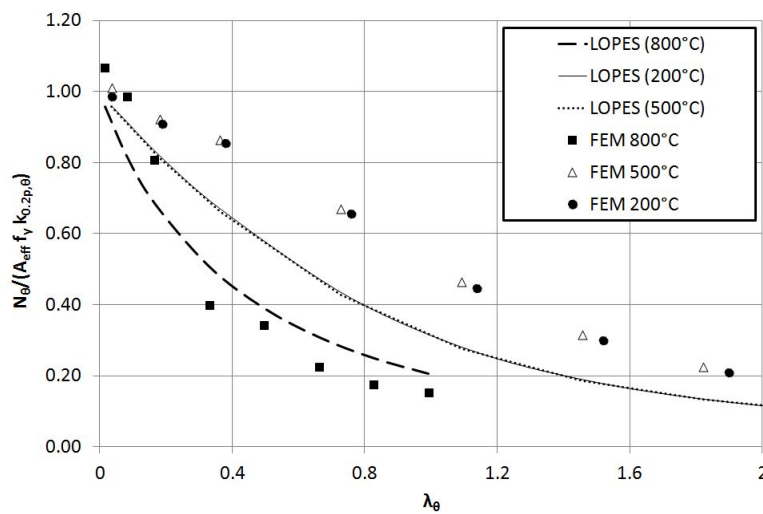
$80 \times 80 \times 3$ Cross-section

FIGURE 4.21a shows again that the model proposed by the European code is safe for temperatures until 500°C . For temperatures above 800°C , this model does not seem well-adapted, due to the large overrating of the bearing capacity. However, nothing can be concluded due to the potential convergence problems.

FIGURE 4.21b shows that the model proposed by Lopes is too conservative for temperatures below 500°C . For temperature above 500°C , the model proposed by Lopes has the same trend that the numerical results, but once again, nothing can be concluded.



(a) EN 1993-1-2

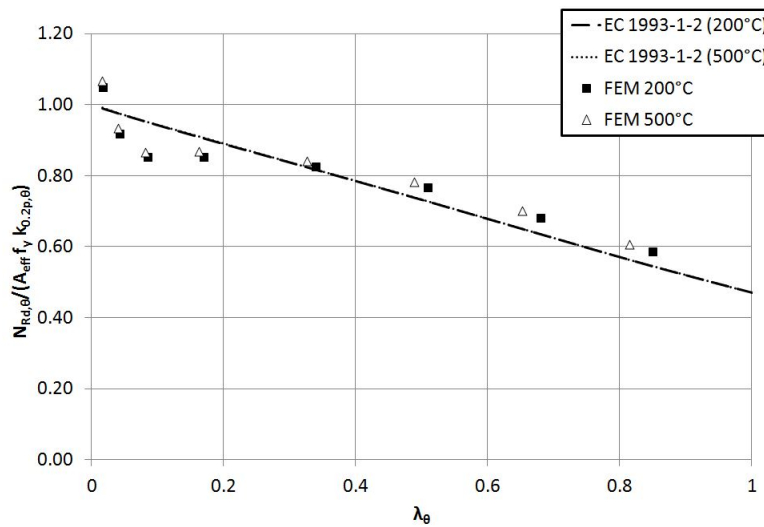


(b) Lopes

Figure 4.21: Comparison : EC1993-1-2 - Numerical results $[80 \times 80 \times 3]$

150 × 150 × 3 Cross-section

As mentioned previously, this cross-section has a high slenderness. FIGURE 4.22a shows that the model recommended by the European code 1993-1-2 is unsafe for short column slenderness ($\lambda_\theta < 0.2$). It could be explained by the formulas used in order to calculate the effective cross-section. Those formulas are maybe not well adapted for such cross-section slenderness.

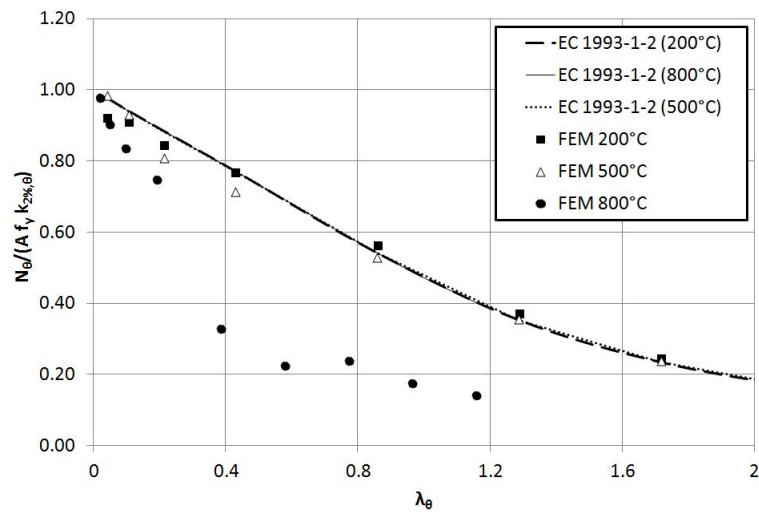


(a) EN 1993-1-2

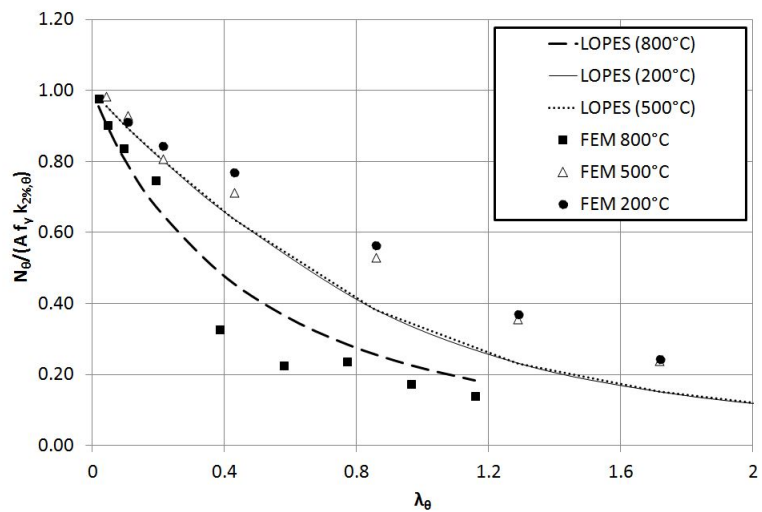
Figure 4.22: Comparison : Buckling curve - Numerical results [$150 \times 150 \times 3$] **$80 \times 80 \times 6$ Cross-section**

FIGURE 4.23a shows that the model recommended by the European code is unsafe for short column slenderness and FIGURE 4.23b illustrates that the model proposed by Lopes is safe, at least for temperatures below 500°C .

Once again, nothing can be concluded about the validity of the model proposed by Lopes at temperatures above 500°C , due to the potential convergence problems. Nevertheless, the trend of the buckling curve proposed by Lopes has the same shape than the obtained numerical results.



(a) EN 1993-1-2



(b) Lopes

Figure 4.23: Comparison : EC1993-1-2 - Numerical results $[80 \times 80 \times 6]$

4.2.9 Enhanced material properties

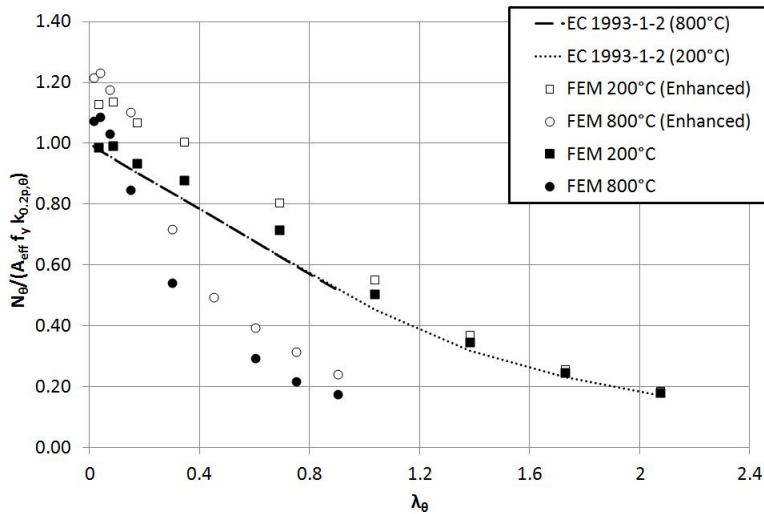
In this section, the strength enhancement is introduced into the finite element model for both corners and flats, for the rectangular $120 \times 80 \times 3$ cross-section. Then, the effect of that strength enhancement will be studied. Note that the numerical results obtained by using the enhanced material properties are compared to the results provided by the predictive models using the nominal properties.

$120 \times 80 \times 3$ Cross-section

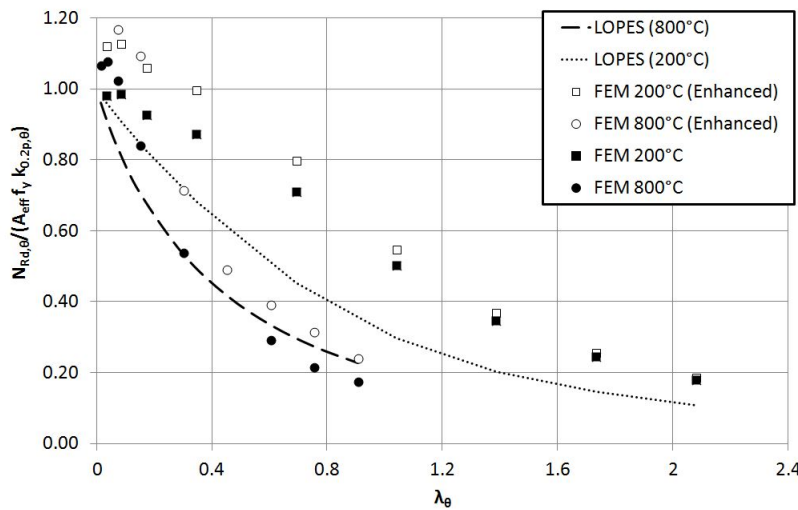
FIGURE 4.24a illustrates the effect of the strength enhancement. It can be seen that the more the global flexural buckling influences the failure mode, the less the strength enhancement influences the column's bearing capacity. Indeed, for columns with high slenderness, introducing the enhanced ma-

material properties does not have any influence, while for low slenderness, the effect is not negligible.

FIGURE 4.24b shows that when the material strength enhancement is taken into account, the predictive model proposed by Lopes is well adapted for temperature above 500°C. Indeed, the numerical results at 800°C are well fitted by the model proposed by Lopes. Hence, despite of the convergence problems, it can be affirmed that the model proposed by Lopes is safe, when the material strength enhancement is taken into account in the numerical model, for the rectangular hollow section.



(a) EN 1993-1-2



(b) Lopes

Figure 4.24: Comparison : EC1993-1-2 - Numerical results (with enhanced strength) [120 × 80 × 3]

4.2.10 Comparison of the models

In this section, the validity of the models will be discussed. A numerical comparison of the six studied predictive models is provided in TABLES 4.8 to 4.12. From this numerical analysis, the following

conclusions can be drawn.

- The model proposed by Ng and Gardner and that proposed by Uppfeldt were always unsafe. In most of the studied cases, those models predict in a safely way the bearing capacity for very short columns and for very long columns, but the prediction for intermediate column lengths is always unsafe. It could be explained by the fact that those models have been calibrated on austenitic stainless steel grade columns. However, when the model proposed by Ng and Gardner is compared to the numerical results obtained with the enhanced material properties, this model is safe and provides predictive bearing capacities very close to the numerical results, as shown in FIGURE 4.25.

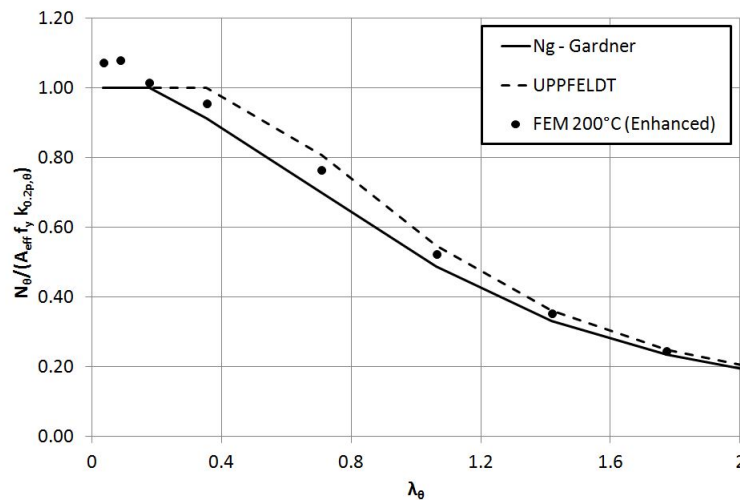


Figure 4.25: Comparison : Ng and Gardner - Uppfeldt - Numerical results (with enhanced strength) $[120 \times 80 \times 3]$

- In most of the studied cases, the predictive results provided by CTICM/CSM at 200°C and 500°C are very close to the numerical results, excepted for the $150 \times 150 \times 3$ cross-section. However, the predictions almost always slightly overestimate the bearing capacity. Moreover, the predictions of the bearing capacity of the Class 1 cross-section are very good. Similarly to the others models, this model is always unsafe at temperatures above 500°C .
- The model proposed by Euro Inox is very close to that recommended by the European code. The only difference is the method used to perform the cross-section classification. For the rectangular cross-section, the predictive results provided by Euro Inox are close to the numerical results, similarly to the European code EN 1993-1-2. However, to predict the bearing capacity of the $80 \times 80 \times 3$ cross-section, the predictive results provided by Euro Inox are unsafe, while those provided by the European code remains save. It can be explained by the way to determine the cross-section classification. The cross-section classification used by Euro Inox leads to a Class 2 cross-section, while that used by the European code leads to a Class 4 cross-section.
- The model proposed by Lopes provides almost always too conservative results at temperature below 500°C . However, for temperature above 500°C , this model seems to have a well-adapted trend. Due to the convergence problems, nothing can be concluded about the precision of this model. However, it can yet be said that this model can safely predict the resistance of rectangular hollow section columns at 800°C , if the enhanced material properties are taken into account.

- Finally, the model recommended by the European code 1993-1-2 is almost always safe for temperatures below $600^{\circ}C$, and seems to be unsafe for temperatures above $600^{\circ}C$. This model seems to be the most consistent. Indeed, for temperature below $600^{\circ}C$, this model provides almost always safe predictions of the bearing capacity of the column.

It must be kept in mind that most of the comparisons made here above are made for numerical results obtained using the nominal material properties. As shown for the model proposed by Ng and Gardner, if the enhanced material properties are taken into account in the numerical model, models which were unsafe when they were compared to numerical results obtained with the nominal properties, can become safe when they are compared to numerical results obtained with the enhanced material properties.

Length	FEM 200°C	EC 1993-1-2	LOPES	UPPFELDT	Euro INOX	Ng - Gardner	CTICM/CSM
		FEM	FEM	FEM	FEM	FEM	FEM
[mm]	[kN]	[-]	[-]	[-]	[-]	[-]	[-]
100	290.13	0.99	0.98	1.07	1.06	1.07	1.08
250	291.67	0.96	0.92	1.06	1.02	1.06	1.08
500	274.03	0.97	0.89	1.13	1.03	1.13	1.14
1000	258.15	0.93	0.78	1.20	0.98	1.09	1.12
2000	209.84	0.88	0.64	1.19	0.92	1.03	1.07
3000	148.48	0.90	0.59	1.14	0.93	1.01	1.06
4000	102.28	0.92	0.59	1.09	0.94	1.00	1.04
5000	72.14	0.94	0.60	1.06	0.96	1.00	1.03
6000	53.15	0.95	0.60	1.05	0.96	1.00	1.03
	MEAN	0.94	0.73	1.11	0.98	1.04	1.07
	COV	0.04	0.22	0.05	0.05	0.04	0.04

Length	FEM 500°C	EC 1993-1-2	LOPES	UPPFELDT	Euro INOX	Ng - Gardner	CTICM/CSM
		FEM	FEM	FEM	FEM	FEM	FEM
[mm]	[kN]	[-]	[-]	[-]	[-]	[-]	[-]
100	235.42	0.98	0.97	1.07	1.04	1.07	1.07
250	236.28	0.95	0.91	1.06	1.01	1.06	1.06
500	222.00	0.96	0.88	1.13	1.02	1.13	1.13
1000	209.17	0.92	0.78	1.20	0.98	1.10	1.11
2000	170.99	0.89	0.64	1.20	0.93	1.05	1.08
3000	123.22	0.90	0.59	1.15	0.93	1.03	1.07
4000	86.32	0.92	0.58	1.10	0.94	1.01	1.05
5000	61.85	0.94	0.58	1.07	0.95	1.00	1.03
6000	43.81	0.99	0.62	1.10	1.00	1.05	1.07
	MEAN	0.94	0.73	1.12	0.98	1.06	1.07
	COV	0.04	0.22	0.05	0.04	0.04	0.03

Length	FEM 600°C	EC 1993-1-2	LOPES	UPPFELDT	Euro INOX	Ng - Gardner	CTICM/CSM
		FEM	FEM	FEM	FEM	FEM	FEM
[mm]	[kN]	[-]	[-]	[-]	[-]	[-]	[-]
100	-	-	-	-	-	-	-
250	-	-	-	-	-	-	-
500	-	-	-	-	-	-	-
1000	122.16	0.93	0.76	1.18	0.99	1.13	1.12
2000	101.27	0.95	0.66	1.24	1.00	1.15	1.15
3000	77.25	1.01	0.62	1.30	1.05	1.20	1.22
4000	58.05	1.05	0.61	1.30	1.08	1.20	1.24
5000	43.05	1.09	0.62	1.29	1.12	1.22	1.25
6000	-	-	-	-	-	-	-
	MEAN	1.01	0.65	1.26	1.05	1.18	1.20
	COV	0.07	0.10	0.04	0.05	0.03	0.05

Length	FEM 700°C	EC 1993-1-2	LOPES	UPPFELDT	Euro INOX	Ng - Gardner	CTICM/CSM
		FEM	FEM	FEM	FEM	FEM	FEM
[mm]	[kN]	[-]	[-]	[-]	[-]	[-]	[-]
100	-	-	-	-	-	-	-
250	-	-	-	-	-	-	-
500	-	-	-	-	-	-	-
1000	-	-	-	-	-	-	-
2000	96.75	1.24	0.81	1.52	1.31	1.50	1.49
3000	27.15	1.49	0.84	1.84	1.57	1.80	1.81
4000	22.35	1.58	0.81	1.95	1.65	1.89	1.92
5000	17.55	1.72	0.83	2.09	1.79	2.02	2.07
6000	14.01	1.82	0.86	2.17	1.88	2.09	2.14
	MEAN	1.57	0.83	1.92	1.64	1.86	1.89
	COV	0.14	0.03	0.13	0.13	0.12	0.14

Length	FEM 800°C	EC 1993-1-2	LOPES	UPPFELDT	Euro INOX	Ng - Gardner	CTICM/CSM
		FEM	FEM	FEM	FEM	FEM	FEM
[mm]	[kN]	[-]	[-]	[-]	[-]	[-]	[-]
100	41.03	0.92	0.90	1.01	0.98	1.01	0.99
250	41.47	0.90	0.84	1.00	0.96	1.00	0.98
500	39.41	0.93	0.81	1.05	0.99	1.05	1.03
1000	32.37	1.08	0.84	1.28	1.15	1.28	1.26
2000	20.73	1.54	0.99	1.87	1.64	1.87	1.86
3000	12.21	2.37	1.32	2.89	2.51	2.87	2.88
4000	11.27	2.30	1.14	2.81	2.41	2.76	2.79
5000	8.30	2.74	1.27	3.33	2.86	3.25	3.32
6000	6.69	2.95	1.31	3.54	3.06	3.44	3.53
	MEAN	1.75	1.05	2.09	1.84	2.06	2.07
	COV	0.48	0.20	0.51	0.47	0.50	0.51

Potential convergence problem

Table 4.8: 120 × 80 × 3

Length	FEM 200°C	EC 1993-1-2	LOPES	UPPFELDT	Euro INOX	Ng - Gardner	CTICM/CSM
		FEM	FEM	FEM	FEM	FEM	FEM
[mm]	[kN]	[-]	[-]	[-]	[-]	[-]	[-]
100	248.85	0.99	0.97	1.01	1.14	1.01	1.01
250	228.45	1.04	0.99	1.10	1.20	1.10	1.10
500	229.36	0.98	0.89	1.10	1.13	1.10	1.10
1000	215.82	0.93	0.77	1.17	1.05	1.05	1.06
2000	165.60	0.90	0.64	1.17	0.99	1.02	1.05
3000	112.49	0.92	0.60	1.12	0.97	1.00	1.04
4000	75.67	0.93	0.59	1.07	0.97	1.00	1.03
5000	52.64	0.95	0.60	1.06	0.98	1.00	1.03
6000	38.29	0.97	0.61	1.05	0.99	1.01	1.03
	MEAN	0.96	0.74	1.09	1.05	1.03	1.05
	COV	0.05	0.23	0.05	0.08	0.04	0.03

Length	FEM 500°C	EC 1993-1-2	LOPES	UPPFELDT	Euro INOX	Ng - Gardner	CTICM/CSM
		FEM	FEM	FEM	FEM	FEM	FEM
[mm]	[kN]	[-]	[-]	[-]	[-]	[-]	[-]
100	203.97	0.97	0.95	0.99	1.21	0.99	0.99
250	185.42	1.03	0.98	1.09	1.28	1.09	1.09
500	186.00	0.98	0.88	1.08	1.21	1.08	1.08
1000	174.33	0.93	0.77	1.16	1.13	1.05	1.06
2000	134.93	0.91	0.64	1.17	1.05	1.03	1.06
3000	93.65	0.92	0.59	1.13	1.01	1.01	1.05
4000	63.69	0.94	0.59	1.09	1.00	1.01	1.04
5000	45.28	0.95	0.59	1.05	0.99	1.00	1.02
6000	30.68	1.04	0.65	1.13	1.08	1.08	1.11
	MEAN	0.96	0.74	1.10	1.11	1.04	1.06
	COV	0.05	0.22	0.05	0.10	0.04	0.03

Length	FEM 800°C	EC 1993-1-2	LOPES	UPPFELDT	Euro INOX	Ng - Gardner	CTICM/CSM
		FEM	FEM	FEM	FEM	FEM	FEM
[mm]	[kN]	[-]	[-]	[-]	[-]	[-]	[-]
100	34.95	0.93	0.90	1.15	1.14	1.15	0.94
250	32.31	0.99	0.91	1.25	1.21	1.25	1.01
500	32.29	0.97	0.83	1.25	1.18	1.25	1.02
1000	26.49	1.12	0.85	1.52	1.37	1.52	1.24
2000	13.05	2.07	1.28	2.82	2.48	2.85	2.34
3000	11.25	2.14	1.14	2.92	2.53	2.97	2.46
4000	7.35	2.88	1.38	3.86	3.32	3.99	3.34
5000	5.73	3.19	1.43	4.14	3.59	4.38	3.69
6000	5.03	3.09	1.35	3.88	3.41	4.20	3.55
	MEAN	1.93	1.12	2.53	2.25	2.62	2.18
	COV	0.50	0.22	0.50	0.46	0.52	0.53

Potential convergence problem

Table 4.9: 80 × 80 × 3

Length	FEM 200°C	EC 1993-1-2	LOPES	UPPFELDT	Euro INOX	Ng - Gardner	CTICM/CSM
		FEM	FEM	FEM	FEM	FEM	FEM
[mm]	[kN]	[-]	[-]	[-]	[-]	[-]	[-]
100	500.00	1.06	1.04	1.09	1.06	1.09	0.94
250	494.96	1.03	0.98	1.10	1.03	1.10	0.95
500	458.91	1.05	0.95	1.18	1.05	1.18	1.03
1000	417.63	1.00	0.83	1.30	1.00	1.15	1.01
2000	306.23	0.96	0.68	1.25	0.96	1.14	1.02
3000	201.03	0.95	0.63	1.14	0.95	1.13	1.02
4000	132.60	0.96	0.62	1.08	0.96	1.13	1.01
5000	91.47	0.97	0.62	1.06	0.97	1.14	1.01
6000	66.30	0.98	0.63	1.04	0.98	1.14	1.01
MEAN		0.99	0.77	1.14	0.99	1.13	1.00
COV		0.04	0.23	0.08	0.04	0.03	0.03

Length	FEM 500°C	EC 1993-1-2	LOPES	UPPFELDT	Euro INOX	Ng - Gardner	CTICM/CSM
		FEM	FEM	FEM	FEM	FEM	FEM
[mm]	[kN]	[-]	[-]	[-]	[-]	[-]	[-]
100	463.83	0.99	0.97	1.02	0.99	1.02	0.81
250	438.77	1.01	0.96	1.07	1.01	1.07	0.86
500	381.26	1.09	0.99	1.24	1.09	1.24	0.99
1000	336.55	1.08	0.89	1.40	1.08	1.26	1.01
2000	249.69	1.02	0.72	1.33	1.02	1.25	1.03
3000	167.66	0.99	0.65	1.19	0.99	1.24	1.03
4000	112.57	0.98	0.63	1.10	0.98	1.23	1.02
5000	78.46	0.98	0.63	1.07	0.98	1.23	1.01
6000	57.28	0.98	0.63	1.05	0.98	1.24	1.01
MEAN		1.01	0.79	1.16	1.01	1.20	0.97
COV		0.04	0.21	0.12	0.04	0.07	0.08

Length	FEM 800°C	EC 1993-1-2	LOPES	UPPFELDT	Euro INOX	Ng - Gardner	CTICM/CSM
		FEM	FEM	FEM	FEM	FEM	FEM
[mm]	[kN]	[-]	[-]	[-]	[-]	[-]	[-]
100	73.39	1.01	0.98	1.02	1.01	1.02	0.83
250	67.80	1.08	0.99	1.11	1.08	1.11	0.90
500	62.85	1.13	0.97	1.20	1.13	1.20	0.97
1000	56.10	1.20	0.90	1.34	1.20	1.34	1.09
2000	24.57	2.43	1.49	2.77	2.43	2.80	2.30
3000	16.89	3.07	1.64	3.55	3.07	3.62	3.01
4000	17.85	2.47	1.20	2.86	2.47	2.97	2.49
5000	13.05	2.81	1.30	3.23	2.81	3.44	2.90
6000	10.50	2.87	1.31	3.25	2.87	3.55	3.00
MEAN		2.01	1.20	2.26	2.01	2.34	1.95
COV		0.44	0.22	0.47	0.44	0.49	0.50

Potential convergence problem

Table 4.10: 80 × 80 × 6

Length	FEM 200°C	EC 1993-1-2	LOPES	UPPFELDT	Euro INOX	Ng - Gardner	CTICM/CSM
		FEM	FEM	FEM	FEM	FEM	FEM
[mm]	[kN]	[-]	[-]	[-]	[-]	[-]	[-]
100	376.92	0.94	0.95	1.06	1.07	1.06	1.09
250	329.51	1.06	1.06	1.21	1.21	1.21	1.24
500	306.00	1.12	1.08	1.30	1.27	1.30	1.34
1000	306.01	1.06	0.99	1.30	1.20	1.30	1.34
2000	296.05	0.99	0.85	1.34	1.11	1.22	1.27
3000	275.15	0.95	0.75	1.34	1.05	1.17	1.22
4000	244.76	0.93	0.68	1.30	1.02	1.13	1.19
5000	210.24	0.93	0.64	1.26	1.00	1.10	1.16
6000	-	-	-	-	-	-	-
MEAN		1.00	0.88	1.26	1.12	1.19	1.23
COV		0.07	0.19	0.07	0.09	0.08	0.07

Length	FEM 500°C	EC 1993-1-2	LOPES	UPPFELDT	Euro INOX	Ng - Gardner	CTICM/CSM
		FEM	FEM	FEM	FEM	FEM	FEM
[mm]	[kN]	[-]	[-]	[-]	[-]	[-]	[-]
100	306.27	0.93	0.94	1.07	1.06	1.07	1.07
250	267.93	1.05	1.04	1.22	1.19	1.22	1.22
500	248.95	1.10	1.07	1.32	1.25	1.32	1.32
1000	249.21	1.05	0.97	1.31	1.19	1.31	1.31
2000	241.34	0.98	0.83	1.36	1.10	1.24	1.25
3000	224.92	0.94	0.74	1.35	1.05	1.19	1.21
4000	201.29	0.93	0.68	1.31	1.02	1.15	1.18
5000	174.29	0.93	0.64	1.27	1.00	1.12	1.16
6000	-	-	-	-	-	-	-
MEAN		0.99	0.86	1.28	1.11	1.20	1.22
COV		0.07	0.19	0.07	0.08	0.07	0.07

Length	FEM 800°C	EC 1993-1-2	LOPES	UPPFELDT	Euro INOX	Ng - Gardner	CTICM/CSM
		FEM	FEM	FEM	FEM	FEM	FEM
[mm]	[kN]	[-]	[-]	[-]	[-]	[-]	[-]
100	53.98	0.86	0.86	1.17	0.98	1.17	0.99
250	48.34	0.96	0.94	1.31	1.09	1.31	1.10
500	45.16	1.01	0.96	1.40	1.15	1.40	1.18
1000	45.65	0.98	0.87	1.39	1.11	1.39	1.17
2000	40.80	1.05	0.82	1.55	1.19	1.55	1.30
3000	32.72	1.25	0.89	1.86	1.42	1.87	1.60
4000	26.70	1.47	0.95	2.18	1.65	2.18	1.88
5000	20.70	1.81	1.09	2.67	2.03	2.66	2.31
6000	-	-	-	-	-	-	-
MEAN		1.17	0.92	1.69	1.33	1.69	1.44
COV		0.27	0.09	0.30	0.27	0.30	0.32

Potential convergence problem

Table 4.11: 150 × 150 × 3

Length	FEM 200°C	EC 1993-1-2	LOPES	UPPFELDT	Euro INOX	Ng - Gardner	CTICM/CSM
	(ENHANCED)	FEM	FEM	FEM	FEM	FEM	FEM
[mm]	[kN]	[-]	[-]	[-]	[-]	[-]	[-]
100	331.57	0.87	0.86	0.93	0.93	0.93	0.95
250	333.75	0.84	0.81	0.93	0.89	0.93	0.94
500	313.75	0.85	0.78	0.99	0.90	0.99	1.00
1000	295.15	0.81	0.69	1.05	0.86	0.96	0.98
2000	236.28	0.78	0.57	1.05	0.82	0.91	0.95
3000	161.93	0.82	0.54	1.04	0.85	0.93	0.97
4000	108.77	0.86	0.55	1.02	0.88	0.94	0.98
5000	75.57	0.90	0.57	1.02	0.91	0.96	0.99
6000	54.98	0.92	0.58	1.01	0.93	0.97	0.99
MEAN		0.85	0.66	1.00	0.89	0.95	0.97
COV		0.05	0.19	0.05	0.04	0.02	0.02

Length	FEM 800°C	EC 1993-1-2	LOPES	UPPFELDT	Euro INOX	Ng - Gardner	CTICM/CSM
	(ENHANCED)	FEM	FEM	FEM	FEM	FEM	FEM
[mm]	[kN]	[-]	[-]	[-]	[-]	[-]	[-]
100	46.43	0.82	0.80	0.89	0.87	0.89	0.88
250	47.01	0.79	0.74	0.88	0.85	0.88	0.87
500	44.97	0.81	0.71	0.92	0.87	0.92	0.91
1000	42.09	0.83	0.65	0.99	0.88	0.99	0.97
2000	27.45	1.17	0.75	1.41	1.24	1.41	1.40
3000	18.87	1.54	0.85	1.87	1.62	1.86	1.86
4000	15.03	1.72	0.86	2.10	1.81	2.07	2.09
5000	12.09	1.88	0.87	2.29	1.97	2.23	2.28
6000	9.24	2.14	0.95	2.56	2.22	2.49	2.56
MEAN		1.30	0.80	1.55	1.37	1.53	1.53
COV		0.41	0.12	0.43	0.40	0.42	0.44

Potential convergence problem

Table 4.12: $120 \times 80 \times 3$ - Numerical modal with enhanced material properties

Chapter 5

Conclusions

The aim of the work was to do a finite element model of the three columns tested in the vertical wall furnace at the Fire Testing Laboratory of the University of Liege. Then, after validating the numerical models against the fire test results, the objective was to perform a parametric analysis in order to compare the proposed design models.

The numerical model of the hollow section columns in fire has been performed by introducing a new parameter at each step. The influence of each parameter was discussed, and it has been decided to take some parameters into account, and to neglect the others.

The residual stresses, the column ends insulation or the use of fitted material properties have been studied, and it has been shown that they do not have a significant influence on the results and therefore, they have been neglected. Conversely, the measured material and geometrical properties were used, and the curved corners were modelled. Finally, it has been shown that the most important parameters in order to obtain a good prediction of the fire resistance of the tested columns are the temperature distribution and the vertical and horizontal thermal gradients. It has also been shown that the thermal conductivity across the cross-section and the thermal radiation of the internal faces of the box has to be taken into account.

Finally, the finite element models obtained were able to predict with a good precision both the failure mode shape and the mean temperature at failure.

After validating the numerical model, the parametric analysis has been performed. Four kind of cross-section have been studied, for nine column's length ranged between $100mm$ and $6000mm$ and at three temperatures ($200^{\circ}C$, $500^{\circ}C$ and $800^{\circ}C$). Intermediate temperatures ($600^{\circ}C$ and $700^{\circ}C$) have been studied for the rectangular cross-section. The material and geometrical properties used were the nominal ones, both global and local initial geometrical imperfections have been modelled, and the residual stresses have been neglected.

The numerical results have been compared to six predictive models. The comparisons of the numerical results and the predictive models have been given in the TABLE ranged between 4.8 and 4.12.

Thus, from the first part of this work, it can be said that the behaviour of the tested columns was well modelled by the finite element models. The measured material properties were used in the numerical model, and therefore, due to the fact that the measured material properties contain the enhanced material properties, it means that those enhanced material properties have to be taken into account in the finite element model in order to get a finite element model able to represent the real behaviour of the column

. In the second part of this work, it has also been shown that the enhanced material properties have a significant influence on the bearing capacity of the columns (see FIGURES 4.24a and 4.24b).

Therefore, to conclude, it can be said that the numerical results obtained with the nominal properties leads to failure loads lower than those which would be obtained if real fire tests were performed.

Indeed, it is known that all the cold-rolled cross-sections have undergone plastic deformations which leads to the enhancement of their material properties. Therefore, the enhanced material properties have to be taken into account in the numerical models, due to their influence on the bearing capacity of the columns.

When the numerical results (calculated with the nominal material properties) are compared to the predictive models, it has been shown that most of the models are unsafe, except those proposed by Lopes and the European code 1993-1-2. However, when the enhanced material properties are introduced into the finite element model, the numerical results obtained increase and models which were unsafe can become safe (as demonstrated for the model proposed by Ng and Gardner).

Consequently, the enhanced material properties have to be taken into account in order to stand for the actual element behaviour and to be allow to use more effective design rules.

Chapter 6

Annexes

6.1 Design rules

CTISM/CSM

The full proposed design model is given hereafter :

$$N_{b,fi,t,Rd} = \frac{\chi_{fi} A k_{y,\theta} f_y}{\gamma_{M,fi}} \quad (6.1)$$

where χ_{fi} is still the reduction factor for flexural buckling in the fire design situation and $k_{y,\theta}$ the reduction factor for the yield strength of steel at the steel temperature θ_a reached at time t .

$$\chi_{fi} = \frac{1}{\varphi_\theta + \sqrt{\varphi_\theta^2 - \bar{\lambda}_\theta^2}} \quad (6.2)$$

with

$$\varphi_\theta = \frac{1}{2} [1 + \alpha (\bar{\lambda}_\theta - \bar{\lambda}_0) + \bar{\lambda}_\theta^2] \quad (6.3)$$

where :

$$\bar{\lambda}_\theta = \bar{\lambda} \left[\frac{k_{y,\theta}}{k_{E,\theta}} \right]^{0.5} \quad (6.4)$$

In order to determine the cross-section classification and the effective area of Class 4 cross-sections, the same formulas than that recommended by 1993-1-2-Annex E are used. However, the material factor is calculated at ambient temperature, according to the following formula.

$$\varepsilon = \left[\frac{235}{f_y} \frac{E}{210000} \right]^{0.5} \quad (6.5)$$

Design rules at elevated temperature proposed by Ng and Gardner

The full proposed design model is given hereafter :

$$N_{b,fi,t,Rd} = \frac{\chi_{fi} A k_{y,\theta} f_y}{\gamma_{M,fi}} \quad (6.6)$$

where χ_{fi} is still the reduction factor for flexural buckling in the fire design situation and $k_{y,\theta}$ the reduction factor for the yield strength of steel at the steel temperature θ_a reached at time t .

$$\chi_{fi} = \frac{1}{\varphi_{\theta} + \sqrt{\varphi_{\theta}^2 - \bar{\lambda}_{\theta}^2}} \quad (6.7)$$

with

$$\varphi_{\theta} = \frac{1}{2} [1 + \alpha (\bar{\lambda}_{\theta} - \bar{\lambda}_0) + \bar{\lambda}_{\theta}^2] \quad (6.8)$$

where :

$$\bar{\lambda}_{\theta} = \bar{\lambda} \left[\frac{k_{y,\theta}}{k_{E,\theta}} \right]^{0.5} \quad (6.9)$$

In order to determine the cross-section classification and the effective area of Class 4 cross-sections, the same formulas than that recommended by 1993-1-2-Annex E are used. However, the material factor at elevated temperature is calculated with the following formula which depends on the strength-stiffness ratio.

$$\varepsilon_{\theta} = \varepsilon \left[\frac{k_{E,\theta}}{k_{y,\theta}} \right]^{0.5} \quad (6.10)$$

where :

- ε is the material factor at ambient temperature
- $k_{E,\theta}$ is the reduction factor for Young's modulus
- $k_{y,\theta} = k_{2,\theta}$ for Class 1 and 2 cross section at room temperature;
- $k_{y,\theta} = k_{0.2p,\theta}$ for Class 3 and 4 cross section at room temperature;

Design rules at elevated temperature proposed by Uppfeldt et al.

The full proposed design model is given hereafter :

$$N_{b,fi,t,Rd} = \frac{\chi_{fi} A k_{y,\theta} f_y}{\gamma_{M,fi}} \quad (6.11)$$

where χ_{fi} is still the reduction factor for flexural buckling in the fire design situation and $k_{y,\theta}$ the reduction factor for the yield strength of steel at the steel temperature θ_a reached at time t .

$$\chi_{fi} = \frac{1}{\varphi_{\theta} + \sqrt{\varphi_{\theta}^2 - \bar{\lambda}_{\theta}^2}} \quad (6.12)$$

with

$$\varphi_{\theta} = \frac{1}{2} [1 + \alpha (\bar{\lambda}_{\theta} - \bar{\lambda}_{0,\theta}) + \bar{\lambda}_{\theta}^2] \quad (6.13)$$

where :

$$\bar{\lambda}_{\theta} = \bar{\lambda} \left[\frac{k_{y,\theta}}{k_{E,\theta}} \right]^{0.5} \quad (6.14)$$

$$\bar{\lambda}_{0,\theta} = \bar{\lambda}_0 \left[\frac{k_{y,\theta}}{k_{E,\theta}} \right]^{0.5} \quad (6.15)$$

In order to determine the cross-section classification and the effective area of Class 4 cross-sections, the same formulas than that recommended by 1993-1-2-Annex E are used. However, the material factor at elevated temperature is calculated with the following formula which depends on the strength-stiffness ratio.

$$\varepsilon_{\theta} = \varepsilon \left[\frac{k_{E,\theta}}{k_{y,\theta}} \right]^{0.5} \quad (6.16)$$

where :

- ε is the material factor at ambient temperature
- $k_{E,\theta}$ is the reduction factor for Young's modulus
- $k_{y,\theta} = k_{2,\theta}$ for Class 1 and 2 cross section at room temperature;
- $k_{y,\theta} = k_{0.2p,\theta}$ for Class 3 and 4 cross section at room temperature;

Design rules at elevated temperature proposed by Lopes, Vila Real et al.

The full proposed design model is given hereafter :

$$N_{b,fi,t,Rd} = \frac{\chi_{fi} A k_{y,\theta} f_y}{\gamma_{M,fi}} \quad (6.17)$$

where χ_{fi} is still the reduction factor for flexural buckling in the fire design situation and $k_{y,\theta}$ the reduction factor for the yield strength of steel at the steel temperature θ_a reached at time t .

$$\chi_{fi} = \frac{1}{\varphi_{\theta} + \sqrt{\varphi_{\theta}^2 - \beta \bar{\lambda}_{\theta}^2}} \quad (6.18)$$

with

$$\varphi_{\theta} = \frac{1}{2} [1 + \alpha \bar{\lambda}_{\theta} + \beta \bar{\lambda}_{\theta}^2] \quad (6.19)$$

and

$$\alpha = \eta \sqrt{\frac{235}{f_y} \frac{E}{210000} \sqrt{\frac{k_{E,\theta}}{k_{y,\theta}}}} \quad (6.20)$$

The non-dimensional slenderness $\bar{\lambda}_{\theta}$ for the temperature θ_a , is still given by :

$$\bar{\lambda}_{\theta} = \bar{\lambda} \left[\frac{k_{y,\theta}}{k_{E,\theta}} \right]^{0.5} \quad (6.21)$$

TABLES 1.10 and 1.11 give the values of coefficients β and η .

In order to determine the cross-section classification and the effective area of Class 4 cross-sections, the same formulas than that recommended by 1993-1-2-Annex E are used. However, the material factor at elevated temperature is calculated with the following formula.

$$\varepsilon = 0.85 \left[\frac{235}{f_y} \frac{E}{210000} \right]^{0.5} \quad (6.22)$$

6.2 Experimental investigation on ferritic stainless steel columns in fire

This is a summary of the report written by Tondini et al., which describes the experiments on the three ferritic columns studied in this work (Tondini et al. [2013]).

6.2.1 Column tests in fire

Test set-up and loading protocol

The columns were tested in the vertical wall furnace at the Fire Testing Laboratory of the University of Liege, which is certified to the ISO 17025 standard by the Belgian accreditation body BELAC. The furnace is provided with a system capable of imposing vertical loads to the specimens. The bottom horizontal beam (HEB 400) can move up along slide guides attached to the columns of the reaction frame, as shown in FIGURE 6.1. These guides basically allow only the translational displacement (up and down). Slight rotation about the horizontal transverse axis of the beam may however occur owing to connection slacks. In fact, for the three tests, a small adjustment was observed at the beginning of the static loading then both displacement transducers (Depl. 1 and Depl. 2 on the FIGURE 6.1) provided the same measure, indicating that the lower support did not rotate. The load was transmitted to the column through the lower beam, this one being pushed up by means of two jacks, as depicted in FIGURE 6.2.

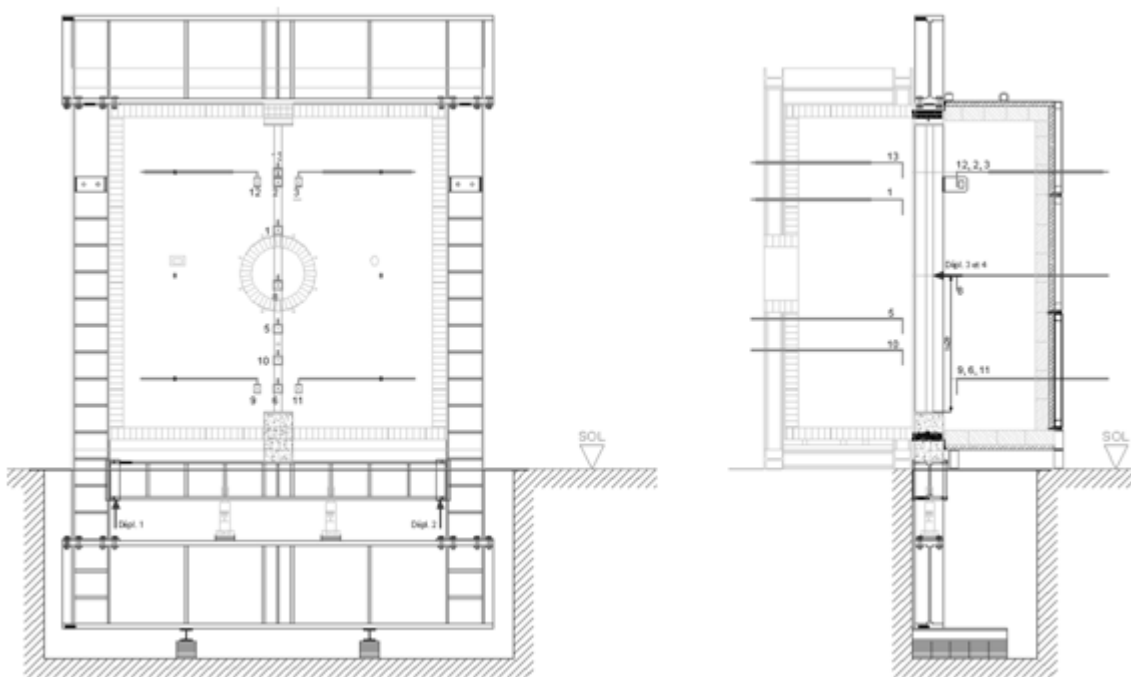


Figure 6.1: Frontal and lateral views of the vertical furnace with the pyrometers

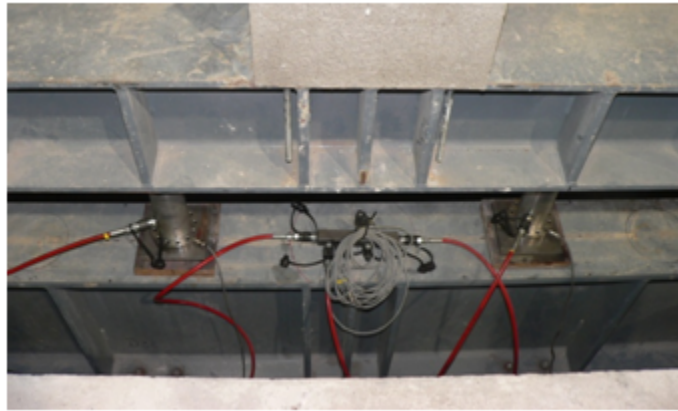


Figure 6.2: Lower HEB 400 beam with left and right jacks

The specimens were welded to 20mm thick end plates (see FIGURE 6.3a) made of stainless steel grade EN 1.4307 and holes for four bolts were allowed for to ensure a full degree of fixity at both column ends. The welding wire was made of EN 1.4430 stainless steel grade and the depth of the welded lips was 5.0 mm thick. Then, the plates were bolted to concrete blocks (see FIGURE 6.3b), which were covered with a fine grain temperature resistant plaster to guarantee an optimal contact with the plate, as shown in FIGURE 6.3c. The purpose of these rigid concrete blocks was to yield a buckling length of the tested columns that is shorter than the distance between the beam of the loading frame.



(a) Bottom end plate with holes for bolts



(b) Supporting concrete block with waiting steel bars



(c) Column top end with plate mounted on the concrete block

Figure 6.3: Column ends

The supports made of concrete were then covered with ceramic fibre (see FIGURE 6.4). The distribution of the temperature, as well as oxygen content and pressure, in the furnace was measured by using pyrometers located at 11 points around the column: 7 coming into the furnace through the closing device and 4 located behind the column coming into the furnace through the brick wall where burners are located, as shown in FIGURE 6.5. They were located at a distance of 100 mm from the steel surface and no thermocouples were installed on the specimens.



Figure 6.4: Column top end covered with ceramic fibre



(a) 4 pyrometers located at the back side of the column



(b) 7 pyrometers located at the front side of the column through the furnace closing device

Figure 6.5: Pyrometers

The load protocol followed the EN1363-1 provisions, which entail to maintain the load constant at least during 15 minutes, time after which the ISO 834 heating curve is applied, with the load being maintained constant until failure. In detail, the tests began by applying the static loading at ambient temperature until 30% of the design buckling resistance $N_{b,Rd}$ calculated at room temperature according to EN1993-1-4 and on the basis of a yield strength equal to 350MPa and of a buckling curve c . The actual lengths of the columns and the applied loads are reported in TABLE 6.1.

	C1	C2	C3
Length [mm]	3000.0	2499.5	2500.0
Heated length [mm]	2950	2449.5	2450
$N_{b,Rd}$ [mm]	239	260	336
Applied load [kN]	72	78	100

Table 6.1: Actual lengths and applied loads

6.3 Numerical model of tubular columns in fire

6.3.1 FEMs results

RHS 2500mm

b	h	L	r_i	r_e	t	E_0	$f_{y,flat}$	$f_{y,corner}$	f_u
[mm]	[mm]	[mm]	[mm]	[mm]	[mm]	$\frac{N}{mm^2}$	$\frac{N}{mm^2}$	$\frac{N}{mm^2}$	$\frac{N}{mm^2}$
79.4	119.5	2500	/	/	2.97	220000	411.77	411.77	562.8
<i>Corner type</i>		<i>Material law</i>		<i>Thermal gradient</i>		<i>End insulation</i>		$\sigma_{residual}$	
[-]		[-]		[-]		[-]		[-]	
Straight		R – O (measured)		/		/		/	
<i>FE type</i>		<i>NG</i>	<i>NL</i>	<i>Nb</i>	<i>Nh</i>	<i>Nc</i>	N_{axial}	Δ	δ
[-]		[-]	[-]	[-]	[-]	[-]	[kN]	[mm]	[mm]
1 st degree		4	125	4	6	0	-100	$0.8 \frac{L}{750}$	$0.8 \times 0.008 \times b$ $0.8 \times 0.01 \times h$

Table 6.2: RHS 2500mm - model 2

b	h	L	r_i	r_e	t	E_0	$f_{y,flat}$	$f_{y,corner}$	f_u
[mm]	[mm]	[mm]	[mm]	[mm]	[mm]	$\frac{N}{mm^2}$	$\frac{N}{mm^2}$	$\frac{N}{mm^2}$	$\frac{N}{mm^2}$
79.4	119.5	2500	3.86	6.83	2.97	220000	411.77	411.77	562.8
<i>Corner type</i>		<i>Material law</i>		<i>Thermal gradient</i>		<i>End insulation</i>		$\sigma_{residual}$	
[-]		[-]		[-]		[-]		[-]	
Curved		R – O (measured)		10 zones		/		/	
<i>FE type</i>		<i>NG</i>	<i>NL</i>	<i>Nb</i>	<i>Nh</i>	<i>Nc</i>	N_{axial}	Δ	δ
[-]		[-]	[-]	[-]	[-]	[-]	[kN]	[mm]	[mm]
1 st degree		4	200	4	6	2	-100	$0.8 \frac{L}{750}$	$0.8 \times 0.008 \times b$ $0.8 \times 0.01 \times h$

Table 6.3: RHS 2500mm - model 4

b	h	L	r_i	r_e	t	E_0	$f_{y,flat}$	$f_{y,corner}$	f_u
[mm]	[mm]	[mm]	[mm]	[mm]	[mm]	$\frac{N}{mm^2}$	$\frac{N}{mm^2}$	$\frac{N}{mm^2}$	$\frac{N}{mm^2}$
79.4	119.5	2500	3.86	6.83	2.97	220000	411.77	411.77	533.92
<i>Corner type</i>		<i>Material law</i>			<i>Thermal gradient</i>		<i>End insulation</i>		$\sigma_{residual}$
[-]		[-]			[-]		[-]		[-]
<i>Curved</i>		<i>R - O (fitted)</i>			10 zones		/		/
<i>FE type</i>		<i>NG</i>	<i>NL</i>	<i>Nb</i>	<i>Nh</i>	<i>Nc</i>	<i>N_{axial}</i>	Δ	δ
[-]		[-]	[-]	[-]	[-]	[-]	[kN]	[mm]	[mm]
1 st degree		4	200	4	6	2	-100	$0.8 \frac{L}{750}$	$0.8 \times 0.008 \times b$ $0.8 \times 0.01 \times h$

Table 6.4: RHS 2500mm - model 5

b	h	L	r_i	r_e	t	E_0	$f_{y,flat}$	$f_{y,corner}$	f_u
[mm]	[mm]	[mm]	[mm]	[mm]	[mm]	$\frac{N}{mm^2}$	$\frac{N}{mm^2}$	$\frac{N}{mm^2}$	$\frac{N}{mm^2}$
79.4	119.5	2500	3.86	6.83	2.97	220000	411.77	411.77	562.8
<i>Corner type</i>		<i>Material law</i>			<i>Thermal gradient</i>		<i>End insulation</i>		$\sigma_{residual}$
[-]		[-]			[-]		[-]		[-]
<i>Curved</i>		<i>R - O (measured)</i>			10 zones		$T_{end} = 20^\circ\text{C}$		/
<i>FE type</i>		<i>NG</i>	<i>NL</i>	<i>Nb</i>	<i>Nh</i>	<i>Nc</i>	<i>N_{axial}</i>	Δ	δ
[-]		[-]	[-]	[-]	[-]	[-]	[kN]	[mm]	[mm]
1 st degree		4	200	4	6	2	-100	$0.8 \frac{L}{750}$	$0.8 \times 0.008 \times b$ $0.8 \times 0.01 \times h$

Table 6.5: RHS 2500mm - model 6

b	h	L	r_i	r_e	t	E_0	$f_{y,flat}$	$f_{y,corner}$	f_u
[mm]	[mm]	[mm]	[mm]	[mm]	[mm]	$\frac{N}{mm^2}$	$\frac{N}{mm^2}$	$\frac{N}{mm^2}$	$\frac{N}{mm^2}$
79.4	119.5	2500	3.86	6.83	2.97	220000	411.77	411.77	562.8
<i>Corner type</i>		<i>Material law</i>			<i>Thermal gradient</i>		<i>End insulation</i>		$\sigma_{residual}$
[-]		[-]			[-]		[-]		[-]
<i>Curved</i>		<i>R - O (measured)</i>			10 zones		/		yes
<i>FE type</i>		<i>NG</i>	<i>NL</i>	<i>Nb</i>	<i>Nh</i>	<i>Nc</i>	<i>N_{axial}</i>	Δ	δ
[-]		[-]	[-]	[-]	[-]	[-]	[kN]	[mm]	[mm]
1 st degree		4	200	4	4	2	-100	$0.8 \frac{L}{750}$	$0.8 \times 0.008 \times b$ $0.8 \times 0.01 \times h$

Table 6.6: RHS 2500mm - model 7

b	h	L	r_i	r_e	t	E_0	$f_{y,flat}$	$f_{y,corner}$	f_u	
[mm]	[mm]	[mm]	[mm]	[mm]	[mm]	$\frac{N}{mm^2}$	$\frac{N}{mm^2}$	$\frac{N}{mm^2}$	$\frac{N}{mm^2}$	
79.4	119.5	2500	3.86	6.83	2.97	220000	411.77	411.77	562.8	
Corner type										
Material law		Thermal gradient			End insulation		$\sigma_{residual}$			
[-]		[-]			[-]		[-]			
Curved		R - O (measured)			15 zones		/		/	
FE type										
NG	NL	Nb	Nh	Nc	N_{axial}	Δ	δ			
[-]	[-]	[-]	[-]	[-]	[-]	[kN]	[mm]	[mm]		
1 st degree	4	200	4	6	2	-100	$0.8 \frac{L}{750}$	$0.8 \times 0.008 \times b$ $0.8 \times 0.01 \times h$		

Table 6.7: RHS 2500mm - model 8

SHS 3000mm**Model 1 : basic model**

This first model is made of straight corners and contains an initial global geometrical imperfection but local imperfections are not modelled. The material and geometrical properties used are the measured ones and all the parameters of this first model are presented in TABLE 6.8. To model the global imperfection, the expressions presented in SECTION 3.3.1 are used.

FIGURE 6.6 illustrates the symmetrical failure mode of this first model. The temperature of the gases when failure occurs is 739.8°C.

b	h	L	r_i	r_e	t	E_0	$f_{y,flat}$	$f_{y,corner}$	f_u	
[mm]	[mm]	[mm]	[mm]	[mm]	[mm]	$\frac{N}{mm^2}$	$\frac{N}{mm^2}$	$\frac{N}{mm^2}$	$\frac{N}{mm^2}$	
79.6	79.2	3000	/	/	2.87	220000	411.77	441.4	588.4	
Corner type										
Material law		Thermal gradient			End insulation		$\sigma_{residual}$			
[-]		[-]			[-]		[-]			
Straight		R - O (measured)			/		/		/	
FE type										
NG	NL	Nb	Nh	Nc	N_{axial}	Δ	δ			
[-]	[-]	[-]	[-]	[-]	[-]	[kN]	[mm]	[mm]		
1 st degree	4	150	4	4	0	-72	$0.8 \frac{L}{750}$	/		

Table 6.8: SHS 3000mm - model 1

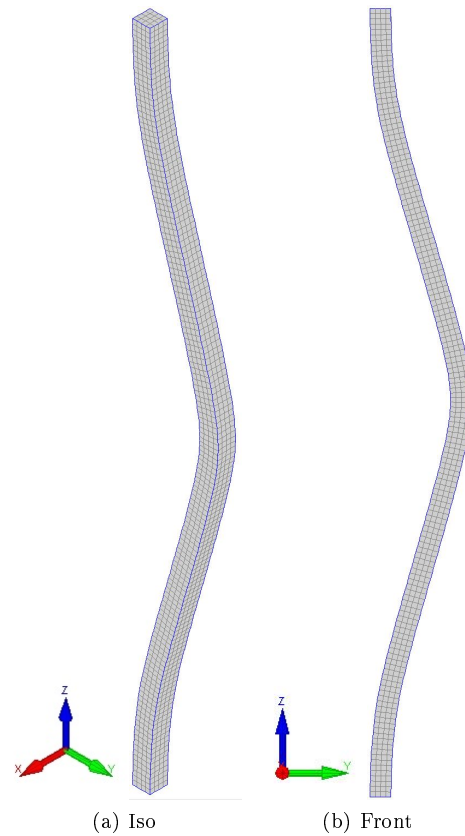


Figure 6.6: SHS 3000mm - model 1 : failure mode

Model 2 : influence of local imperfections

Initial local geometrical imperfections are added to model 1 to get model 2. The local imperfection expression used are that presented in SECTION 3.3.2. The values of the parameters used in this second model are available in TABLE 6.9.

FIGURE 6.7 illustrates the failure mode of this second model. It is the same than that obtained with the first model, but local waves develop due to the introduction of initial local imperfections. The gases temperature at failure is 737.4°C .

For those columns made of square hollow section, the cross-section slenderness is smaller than that of the rectangular hollow section modelled in the previous section. Therefore the mean failure temperature of the square hollow section column is less influenced by the introduction of the local imperfections than the rectangular hollow section column. Indeed, when local geometrical imperfections were introduced in the column with rectangular hollow section, the mean failure temperature was reduced of an amount of 5.5°C whereas the failure temperature is reduced of 2.4°C for the square hollow section. It can be explained by the fact that, concerning the square hollow section, the effective area is closer to the nominal area than for rectangular hollow section.

b	h	L	r_i	r_e	t	E_0	$f_{y,flat}$	$f_{y,corner}$	f_u	
[mm]	[mm]	[mm]	[mm]	[mm]	[mm]	$\frac{N}{mm^2}$	$\frac{N}{mm^2}$	$\frac{N}{mm^2}$	$\frac{N}{mm^2}$	
79.6	79.2	3000	/	/	2.87	220000	411.77	441.4	588.4	
<i>Corner type</i>					<i>Material law</i>		<i>Thermal gradient</i>		<i>End insulation</i>	$\sigma_{residual}$
[-]					[-]		[-]		[-]	[-]
<i>Straight</i>					<i>R - O (measured)</i>		/		/	/
<hr/>										
<i>FE type</i>		NG	NL	Nb	Nh	Nc	N_{axial}	Δ	δ	
[-]		[-]	[-]	[-]	[-]	[-]	[kN]	[mm]	[mm]	
$1^{st} degree$		4	150	4	4	0	-72	$0.8 \frac{L}{750}$	$0.8 \times 0.008 \times b$ $0.8 \times 0.01 \times h$	

Table 6.9: SHS 3000mm - model 2

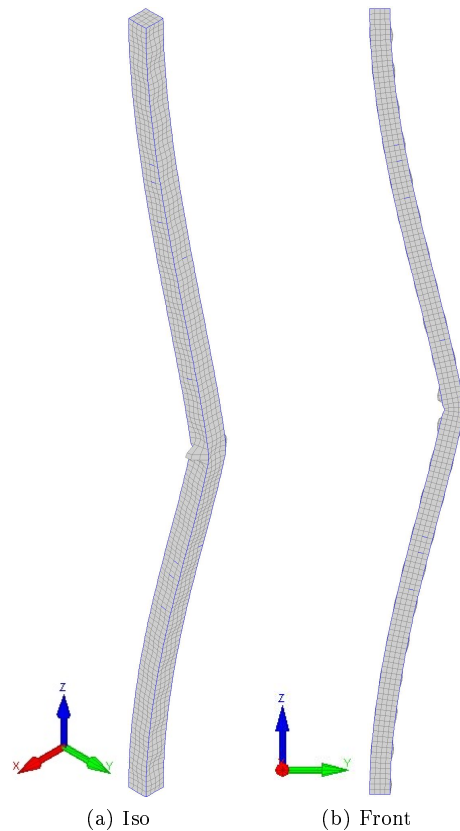


Figure 6.7: SHS 3000mm - model 2 : failure mode

Model 3 : influence of curved corners

This third model introduces the curved corners. Using curved corners make the numerical model closer to the real cross-section properties, as discussed previously. The same comparison has been led for

the RHS column and it has shown that using two or three elements to model a corner gives the same results. Therefore this model will be made of two elements per corner. The values of the parameters of this third model are presented in TABLE 6.10.

There is a small deviation of failure temperature between the previous model and this one. Indeed, the gases temperature at failure decreases from 737.4°C in the second model to 735.8°C in this third model.

b	h	L	r_i	r_e	t	E_0	$f_{y,flat}$	$f_{y,corner}$	f_u
[mm]	[mm]	[mm]	[mm]	[mm]	[mm]	$\left[\frac{N}{mm^2}\right]$	$\left[\frac{N}{mm^2}\right]$	$\left[\frac{N}{mm^2}\right]$	$\left[\frac{N}{mm^2}\right]$
79.6	79.2	3000	4	6.87	2.87	220000	411.77	441.4	588.4
<i>Corner type</i>		<i>Material law</i>			<i>Thermal gradient</i>		<i>End insulation</i>	$\sigma_{residual}$	
[-]		[-]			[-]		[-]	[-]	
<i>Curved</i>		<i>R - O (measured)</i>			/		/	/	
<i>FE type</i>		<i>NG</i>	<i>NL</i>	<i>Nb</i>	<i>Nh</i>	<i>Nc</i>	<i>N_{axial}</i>	Δ	δ
[-]		[-]	[-]	[-]	[-]	[-]	[kN]	[mm]	[mm]
<i>1st degree</i>		4	240	4	4	2	-72	$0.8 \frac{L}{750}$	$0.8 \times 0.008 \times b$ $0.8 \times 0.01 \times h$

Table 6.10: SHS 3000mm - model 3

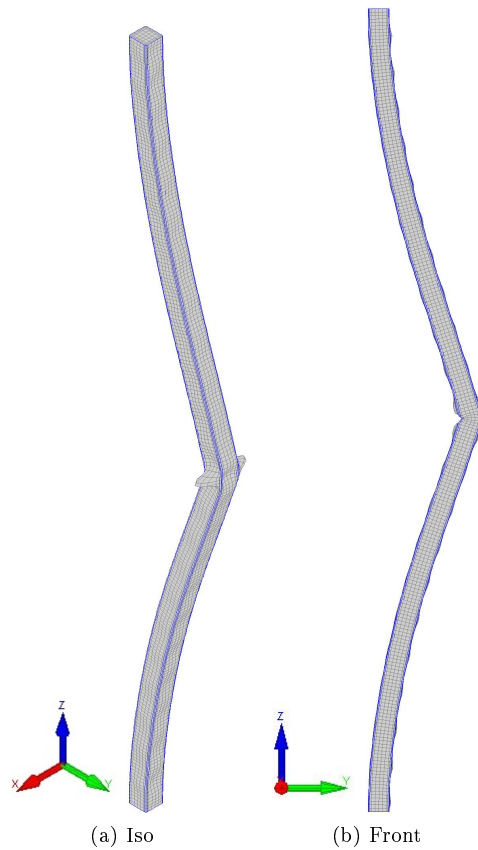


Figure 6.8: SHS 3000mm - model 3 : failure mode

Model 4 : influence of thermal gradient

The parameters used in this model are the same than in the third model. However, this model takes into account the vertical and horizontal thermal gradients in the furnace. The temperature evolution of the zones assigned to the shell elements are based on the 1D thermal analysis. The thermal gradient is introduced by dividing the column into 12 zones, as described in SECTION 3.5. The values of the parameters used in this fourth model are given in TABLE 6.11.

FIGURE 6.9 illustrates the failure mode obtained with this fourth model. This failure mode is very close to that obtained during the test and which is illustrated in FIGURE 2.11. This failure mode is made of two main hinges located in the upper zone of the column and near the mid-height of the column. The mean temperature when failure occurs is $733.4^{\circ}C$.

b	h	L	r_i	r_e	t	E_0	$f_{y,flat}$	$f_{y,corner}$	f_u
[mm]	[mm]	[mm]	[mm]	[mm]	[mm]	$\frac{N}{mm^2}$	$\frac{N}{mm^2}$	$\frac{N}{mm^2}$	$\frac{N}{mm^2}$
79.6	79.2	3000	4	6.87	2.87	220000	411.77	441.4	588.4
<hr/>									
<i>Corner type</i>	<i>Material law</i>			<i>Thermal gradient</i>			<i>End insulation</i>	$\sigma_{residual}$	
[-]	[-]			[-]			[-]	[-]	
<i>Curved</i>	<i>R - O (measured)</i>			12 zones			/	/	
<hr/>									
<i>FE type</i>	NG	NL	Nb	Nh	Nc	N_{axial}	Δ	δ	
[-]	[-]	[-]	[-]	[-]	[-]	[kN]	[mm]	[mm]	
$1^{st} degree$	4	240	4	4	2	-72	$0.8 \frac{L}{750}$	$0.8 \times 0.008 \times b$ $0.8 \times 0.01 \times h$	

Table 6.11: SHS 3000mm - model 4

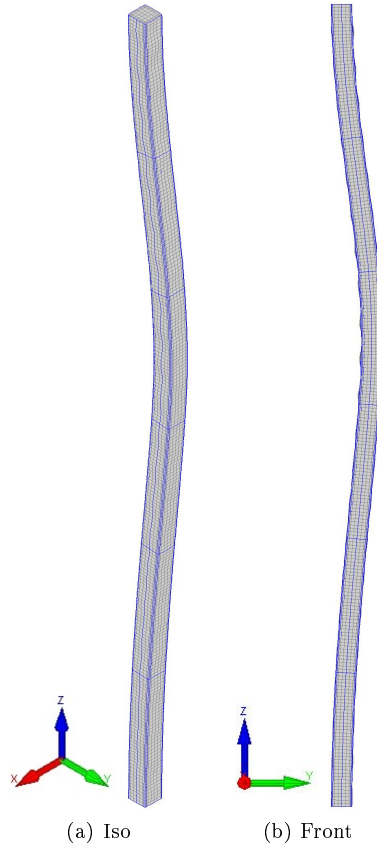


Figure 6.9: SHS 3000mm - model 4 : failure mode

Model 5 : influence of the material law

This model is the same than the previous one, but the material properties used are different. Measured material properties were used in model four ($f_{0.2p}$ and f_u) while in this fifth model, f_u is determined

so as to minimize the difference between the measured $\sigma - \varepsilon$ curve and the $\sigma - \varepsilon$ curve obtained with the modified Ramberg-Osgood model recommended in EN 1993-1-2, as discussed in SECTION 3.2. The value of f_u and the values of the other parameters are available in TABLE 6.12.

The failure mode obtained is the same than that obtained in all the others models using the thermal gradient. The failure temperature decreases from 733.4°C with the measured properties to 733.3°C with the fitted properties.

b	h	L	r_i	r_e	t	E_0	$f_{y,flat}$	$f_{y,corner}$	f_u
[mm]	[mm]	[mm]	[mm]	[mm]	[mm]	$\frac{N}{\text{mm}^2}$	$\frac{N}{\text{mm}^2}$	$\frac{N}{\text{mm}^2}$	$\frac{N}{\text{mm}^2}$
79.6	79.2	3000	4	6.87	2.87	220000	411.77	411.77	556.67
<i>Corner type</i>		<i>Material law</i>			<i>Thermal gradient</i>		<i>End insulation</i>		$\sigma_{residual}$
[-]		[-]			[-]		[-]		[-]
<i>Curved</i>		<i>R - O (fitted)</i>			12 zones		/		/
<i>FE type</i>		<i>NG</i>	<i>NL</i>	<i>Nb</i>	<i>Nh</i>	<i>Nc</i>	<i>N_{axial}</i>	Δ	δ
[-]		[-]	[-]	[-]	[-]	[-]	[kN]	[mm]	[mm]
<i>1st degree</i>		4	240	4	4	2	-72	$0.8 \frac{L}{750}$	$0.8 \times 0.008 \times b$ $0.8 \times 0.01 \times h$

Table 6.12: SHS 3000mm - model 5

Model 6 : influence of the thermal insulation at both ends

This model is the same than the model four, but a thermal insulation is introduced at both ends of the column in order to have a model as close to the tested column as possible. A temperature equal to 20°C is imposed at both ends in order to study what happens in this extreme configuration. The values of the parameters used in this sixth model are provided in TABLE 6.13.

The failure temperature increases from 733.4°C without insulation to 733.9°C with insulation. The thermal axial displacement is reduced in the numerical model with thermal insulation at both ends, due to the reduction of the heated length of the column.

For the same reasons than those mentioned for the rectangular hollow section, the thermal insulation at both column's ends is not defined as a relevant parameter.

b	h	L	r_i	r_e	t	E_0	$f_{y,flat}$	$f_{y,corner}$	f_u
[mm]	[mm]	[mm]	[mm]	[mm]	[mm]	$\frac{N}{\text{mm}^2}$	$\frac{N}{\text{mm}^2}$	$\frac{N}{\text{mm}^2}$	$\frac{N}{\text{mm}^2}$
79.6	79.2	3000	4	6.87	2.87	220000	411.77	441.4	588.4
<i>Corner type</i>		<i>Material law</i>			<i>Thermal gradient</i>		<i>End insulation</i>		$\sigma_{residual}$
[-]		[-]			[-]		[-]		[-]
<i>Curved</i>		<i>R - O (measured)</i>			12 zones		$T_{end} = 20^\circ\text{C}$		/
<i>FE type</i>		<i>NG</i>	<i>NL</i>	<i>Nb</i>	<i>Nh</i>	<i>Nc</i>	<i>N_{axial}</i>	Δ	δ
[-]		[-]	[-]	[-]	[-]	[-]	[kN]	[mm]	[mm]
<i>1st degree</i>		4	240	4	4	2	-72	$0.8 \frac{L}{750}$	$0.8 \times 0.008 \times b$ $0.8 \times 0.01 \times h$

Table 6.13: SHS 3000mm - model 6

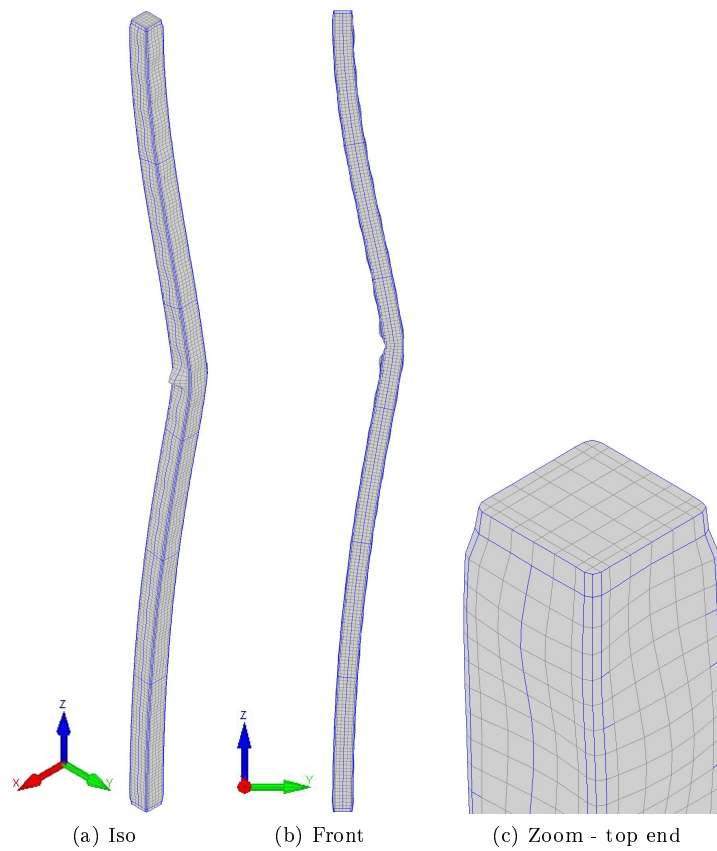


Figure 6.10: SHS 3000mm - model 7 : failure mode

Model 7 : influence of residual stresses

This model has the same properties than the model four, but residual stresses are introduced into the numerical model.

The failure mode obtained is the same than those obtained with all the models where thermal gradient were taken into account. The mean failure temperature is equal to 733.7°C , which is very close to that obtained in the fourth model (733.4°C). Therefore, residual stresses will not be taken into account in the following finite element models.

b	h	L	r_i	r_e	t	E_0	$f_{y,flat}$	$f_{y,corner}$	f_u	
[mm]	[mm]	[mm]	[mm]	[mm]	[mm]	$\frac{N}{mm^2}$	$\frac{N}{mm^2}$	$\frac{N}{mm^2}$	$\frac{N}{mm^2}$	
79.4	119.5	2500	4	6.87	2.97	220000	411.77	411.77	562.8	
<i>Corner type</i>					<i>Material law</i>		<i>Thermal gradient</i>		<i>End insulation</i>	$\sigma_{residual}$
[-]					[-]		[-]		[-]	[-]
<i>Curved</i>					<i>R - O (measured)</i>		12 zones		/	<i>yes</i>
<i>FE type</i>		NG	NL	Nb	Nh	Nc	N_{axial}	Δ	δ	
[-]		[-]	[-]	[-]	[-]	[-]	[kN]	[mm]	[mm]	
$1^{st} degree$		4	240	4	4	2	-72	$0.8 \frac{L}{750}$	$0.8 \times 0.008 \times b$ $0.8 \times 0.01 \times h$	

Table 6.14: SHS 3000mm - model 7

List of Figures

0.1	Geometrical properties of the cross-section	6
1.1	Strength and stiffness reduction factors at elevated temperature - EC1993-1-2 - Annex C	11
1.2	Strength reduction factors at elevated temperature - Gardner et al. [2010]	12
1.3	Strength reduction factors at elevated temperature - Manninen and Saynajakangas [2013]	13
1.4	Stiffness reduction factors at elevated temperature - Gardner et al. [2010]	14
1.5	Material behavior of stainless steel at elevated temperature - EC1993-1-2-Annex C	17
1.6	Comparison of the models	18
1.7	Cold-rolling fabrication of tubular box sections - Rossi et al. [2013]	19
1.8	Corner regions - Uppfeldt, 2008	21
1.9	Variation of the modification factor $\left(\frac{k_{E,\theta}}{k_{y,\theta}}\right)^{0.5}$ with temperature	24
2.1	Notations for the cross-section dimensions	30
2.2	$\sigma_{true} - \varepsilon_{ln}$ curve - RHS	32
2.3	$\sigma_{true} - \varepsilon_{ln}$ curve - SHS	32
2.4	Column C3 - Failure mode	34
2.5	Temperature distribution at failure time ($t = 711s$) - Measured with the pyrometers	35
2.6	Ten zones	35
2.7	Temperature distribution at failure time ($t = 711s$) - Temperature discretization	36
2.8	Temperature evolution in the back side of the furnace	37
2.9	Temperature evolution in the front side of the furnace	37
2.10	Deviation of temperature from the temperature of the ISO 834 curve	38
2.11	SHS 3000mm column - Failure mode	39
2.12	Temperature distribution at failure time ($t = 729s$) - Measured with the pyrometers	40
2.13	Temperature distribution at failure time ($t = 729s$) - Temperature discretization	40
2.14	Temperature evolution in the back side of the furnace	41
2.15	Temperature evolution in the front side of the furnace	41
2.16	Deviation of temperature from the temperature of the ISO 834 curve	42
2.17	SHS 2500mm column - Failure mode	43
2.18	Temperature distribution at failure time ($t = 720s$) - Measured with the pyrometers	44
2.19	Temperature distribution at failure time ($t = 720s$) - Temperature discretization	44
2.20	Temperature evolution in the back side of the furnace	45
2.21	Temperature evolution in the front side of the furnace	45
2.22	Deviation of temperature from the temperature of the ISO 834 curve	46
3.1	Rectangular and square hollow section with straight corners	48
3.2	Rectangular and square hollow section with curved corners (two elements per corner)	48
3.3	Rectangular and square hollow section with curved corners (three elements per corner)	48
3.4	Boundary conditions during the test	50
3.5	Boundary conditions - Numerical model	50
3.6	Strength enhancement in corner regions	51

3.7	Comparison between the law proposed in EN 1993-1-2 using the measured properties and the stress-strain curve obtained during the test	52
3.8	Comparison between the law proposed in EN 1993-1-2 (fitted on the measured law) and the stress-strain curve obtained during the test	53
3.9	Global imperfection tolerance - EN 1090-2	54
3.10	Local imperfections - shape	55
3.11	Membrane residual stresses distribution - Gardner's proposal	56
3.12	Residual stresses distribution on the rectangular cross-section	57
3.13	Temperature evolution in the furnace and in the stainless steel material	58
3.14	Temperature distribution - ten zones model	59
3.15	Temperature distribution in the cross-section	59
3.16	RHS - 2D thermal analysis	60
3.17	SHS - 2D thermal analysis	60
3.18	Comparison of the thermal analyses : 2D - 1D	61
3.19	Temperature distribution in the cross-section - 2D thermal analysis	62
3.20	Loading conditions	62
3.21	RHS 2500mm - model 1 : failure mode	64
3.22	RHS 2500mm - model 2 : failure mode	65
3.23	RHS 2500mm - model 3 : failure mode	66
3.24	RHS 2500mm - model 4 : failure mode	67
3.25	RHS 2500mm - test in fire - failure mode	68
3.26	RHS 2500mm - model 5 : failure mode	69
3.27	RHS 2500mm - model 6 : failure mode	70
3.28	RHS 2500mm - model 7 : failure mode	71
3.29	RHS 2500mm - model 8 : failure mode	72
3.30	SHS 3000mm - Finite element model : failure mode	74
3.31	SHS 2500mm - Finite element model : failure mode	76
4.1	First type of simulation : Constant load and varying temperature	78
4.2	Second type of simulation : Varying load and constant temperature	78
4.3	Boundary conditions	79
4.4	Boundary conditions - Numerical model	80
4.5	120×80×3 : Numerical results versus theoretical predictions for 200C	83
4.6	120×80×3 : Numerical results versus theoretical predictions for 500C	84
4.7	120×80×3 : Numerical results versus theoretical predictions for 800C	84
4.8	80 × 80 × 3 cross-section at 500°C for $L = 500mm$: Failure mode	85
4.9	80×80×3 : Numerical results versus theoretical predictions for 200C	86
4.10	80×80×3 : Numerical results versus theoretical predictions for 500C	86
4.11	80×80×3 : Numerical results versus theoretical predictions for 800C	87
4.12	150 × 150 × 3 - Failure modes	88
4.13	150×150×3 : Numerical results versus theoretical predictions for 200C	89
4.14	150×150×3 : Numerical results versus theoretical predictions for 500C	89
4.15	150×150×3 : Numerical results versus theoretical predictions for 800C	90
4.16	80×80×6 : Numerical results versus theoretical predictions for 200C	91
4.17	80×80×6 : Numerical results versus theoretical predictions for 500C	91
4.18	80×80×6 : Numerical results versus theoretical predictions for 800C	92
4.19	$\frac{k_{E,\theta}}{k_{0.2p,\theta}}$	93
4.20	Comparison : EC1993-1-2 - Numerical results [120 × 80 × 3]	94
4.21	Comparison : EC1993-1-2 - Numerical results [80 × 80 × 3]	95
4.22	Comparison : Buckling curve - Numerical results [150 × 150 × 3]	96
4.23	Comparison : EC1993-1-2 - Numerical results [80 × 80 × 6]	97
4.24	Comparison : EC1993-1-2 - Numerical results (with enhanced strength) [120 × 80 × 3]	98

4.25 Comparison : Ng and Gardner - Uppfeldt - Numerical results (with enhanced strength) [120 × 80 × 3]	99
6.1 Frontal and lateral views of the vertical furnace with the pyrometers	111
6.2 Lower HEB 400 beam with left and right jacks	112
6.3 Column ends	112
6.4 Column top end covered with ceramic fibre	113
6.5 Pyrometers	113
6.6 SHS 3000mm - model 1 : failure mode	117
6.7 SHS 3000mm - model 2 : failure mode	118
6.8 SHS 3000mm - model 3 : failure mode	120
6.9 SHS 3000mm - model 4 : failure mode	121
6.10 SHS 3000mm - model 7 : failure mode	123

List of Tables

1.1	Chemical composition of stainless steel 1.4003 grade - [% by mass]	8
1.2	Thermal material properties	9
1.3	Strength and stiffness reduction factors at elevated temperature - EC1993-1-2 - Annex C	10
1.4	Compound Ramberg-Osgood's parameters - Ashraf et al. [2006]	16
1.5	Compound Ramberg-Osgood's parameters - Afshan et al. [2013b]	16
1.6	Parameters used for the comparison	18
1.7	Values of α and $\bar{\lambda}_0$ for flexural buckling	22
1.8	Values of α and $\bar{\lambda}_0$ for flexural buckling - CTICM/CSM	25
1.9	Values of α and $\bar{\lambda}_0$ for flexural buckling - Ng and Gardner	25
1.10	Coefficient for determining the reduction factor	27
1.11	Severity factor for the flexural buckling of stainless steel members in case of fire	27
1.12	Summary of the new predictive models	28
2.1	Cross-section dimensions	30
2.2	Mill certificate data (from Stalatube)	31
2.3	Average tensile coupon tests results (from Aperam)	31
2.4	True material properties	31
2.5	Column tests results at ambient temperature	33
2.6	RHS 2500mm - Failure characteristics	33
2.7	SHS 3000mm column - Failure characteristics	38
2.8	SHS 2500mm column - Failure characteristics	42
2.9	Mean failure temperatures	46
3.1	Influence of the discretization on the value of the cross section and of inertia	49
3.2	Measured material parameters - RHS	51
3.3	Fitted material properties - RHS	52
3.4	Tolerances for square and rectangular hollow sections - EN10219-2	54
3.5	Membrane residual stresses - characteristic values	55
3.6	Bending residual stresses - characteristic values	55
3.7	Residual stresses	56
3.8	Vertical loading	62
3.9	RHS 2500mm- model 1	64
3.10	RHS 2500mm - model 3	66
3.11	SHS 3000mm - Influence of the parameters	73
3.12	SHS 3000mm - Finite element model	73
3.13	SHS 2500mm - Finite element model	75
4.1	Studied cross-sections - Parametric analysis	80
4.2	Material properties(EN 10088-4)	81
4.3	Enhanced material properties : $120 \times 80 \times 3$	81
4.4	Material factors : ε	82

4.5	Cross-section classification : $\frac{c/t}{\varepsilon}$	82
4.6	Cross-section classification	82
4.7	Cross-section classification : limit values of the ratio $\frac{c/t}{\varepsilon}$	82
4.8	$120 \times 80 \times 3$	101
4.9	$80 \times 80 \times 3$	102
4.10	$80 \times 80 \times 6$	103
4.11	$150 \times 150 \times 3$	104
4.12	$120 \times 80 \times 3$ - Numerical modal with enhanced material properties	105
6.1	Actual lengths and applied loads	114
6.2	RHS $2500mm$ - model 2	114
6.3	RHS $2500mm$ - model 4	114
6.4	RHS $2500mm$ - model 5	115
6.5	RHS $2500mm$ - model 6	115
6.6	RHS $2500mm$ - model 7	115
6.7	RHS $2500mm$ - model 8	116
6.8	SHS $3000mm$ - model 1	116
6.9	SHS $3000mm$ - model 2	118
6.10	SHS $3000mm$ - model 3	119
6.11	SHS $3000mm$ - model 4	121
6.12	SHS $3000mm$ - model 5	122
6.13	SHS $3000mm$ - model 6	122
6.14	SHS $3000mm$ - model 7	124

Bibliography

- S. Afshan, L. Gardner, and N.R. Baddoo. Buckling response of ferritic stainless steel columns at elevated temperatures. 2013a.
- S. Afshan, B. Rossi, and L. Gardner. Strength enhancements in cold-formed structural sections - part i : Material testing. *Journal of Constructional Steel Research*, 2013b.
- T Ala-Outinen and T Oksanen. Stainless steel compression members exposed to fire. *VTT research notes*, 1997.
- M. Ashraf. M. structural stainless steel design : Resistance based on deformation capacity. *PhD. Thesis. Departement of Civil and Environmental Engineering, Imperial College London, UK*, 2006.
- M. Ashraf, L. Gardner, and D. A. Nethercot. Finite element modelling of structural stainless steel cross-sections. *Thin-Walled Structures*, 44(10):1048 – 1062, 2006. ISSN 0263-8231. doi: 10.1016/j.tws.2006.10.010.
- J. Chen and B. Young. Stress-strain curves for stainless steel at elevated temperatures. *Engineering structures*, 28(2):229–239, 2006.
- R.B. Cruise and L. Gardner. Residual stress analysis of structural stainless steel sections. *Journal of Constructional Steel Research*, 64(3):352 – 366, 2008. ISSN 0143-974X. doi: 10.1016/j.jcsr.2007.08.001.
- CTICM/CSM. Stainless steel column buckling behaviour at elevated temperatures - comparison of euro inox and cticm methods. 2005.
- Euro-Inox. Design manual for structural stainless steel. *Building series*, 3, 2002. Euro Inox and the Steel Construction Institute.
- European Committee for standardization (CEN). Eurocode 1 : Actions on structures - part 1-2 : General actions - actions on structures exposed to fire. 2002.
- European Committee for standardization (CEN). Stainless steels - part 1 : List of stainless steels. en 10088-1. 2005a.
- European Committee for standardization (CEN). Eurocode 3 : Design of steel structures - part 1-2 : General rules - structural fire design, en 1993-1-2. 2005b.
- European Committee for standardization (CEN). Eurocode 3 : Design of steel structures - part 1-4 : General rules - supplementary rules for stainless steels, en 1993-1-4. 2006a.
- European Committee for standardization (CEN). Eurocode 3 : Design of steel structures - part 1-5 - annex c : Finite element methods of analysis (fem). 2006b.
- European Committee for standardization (CEN). Execution of steel structures and aluminium structures - part 2 : Technical requirements for steel structures, en 1090-2. 2008.

- J.M. Franssen. User's manual for safir 2011 : A computer program for analysis of structures subjected to fire. 2011.
- L. Gardner and M. Ashraf. Structural design for non-linear metallic materials. *Engineering Structures*, 28:926 – 34, 2006.
- L. Gardner and N.R. Baddoo. Fire testing and design of stainless steel structures. *Journal of Constructional Steel Research*, 62(6):532 – 543, 2006. ISSN 0143-974X. doi: 10.1016/j.jcsr.2005.09.009.
- L. Gardner and R.B. Cruise. Modeling of residual stresses in structural stainless steel sections. *Journal of structural engineering*, 135(1):42–53, 2009. doi: 10.1061/(ASCE)0733-9445(2009)135:1(42).
- L. Gardner and K.T. Ng. Temperature development in structural stainless steel sections exposed to fire. *Fire Safety Journal*, 41(3):185 – 203, 2006. ISSN 0379-7112. doi: 10.1016/j.firesaf.2005.11.009.
- L. Gardner, A. Insausti, K.T. Ng, and M. Ashraf. Elevated temperature material properties of stainless steel alloys. *Journal of Constructional Steel Research*, 66(5):634 – 647, 2010. ISSN 0143-974X. doi: 10.1016/j.jcsr.2009.12.016.
- P. Hradil, A. Talja, E. Real, E. Mirambell, and B. Rossi. Generalized multistage mechanical model for nonlinear metallic materials. *Thin-Walled Structures*, 63(0):63 – 69, 2013. ISSN 0263-8231. doi: 10.1016/j.tws.2012.10.006.
- M. Jandera, L. Gardner, and J. Machacek. Residual stresses in cold-rolled stainless steel hollow sections. *Journal of Constructional Steel Research*, 64(11):1255 – 1263, 2008. ISSN 0143-974X. doi: 10.1016/j.jcsr.2008.07.022.
- N. Lopes, P. Vila Real, L.S. da Silva, and J.M. Franssen. Numerical analysis of stainless steel beam-columns in case of fire. *Fire Safety Journal*, 50(0):35 – 50, 2012. ISSN 0379-7112. doi: 10.1016/j.firesaf.2012.02.003.
- T. Manninen and J. Saynajakangas. Mechanical properties of ferritic stainless steels at elevated temperature. (2), 2013. Research Programme of the Research Fund for Coal and Steel.
- K.T. Ng and L. Gardner. Buckling of stainless steel columns and beams in fire. *Engineering Structures*, 29(5):717 – 730, 2007. ISSN 0141-0296. doi: 10.1016/j.engstruct.2006.06.014.
- K.J.R. Rasmussen. Full-range stress-strain curves for stainless steel alloys. *Journal of Constructional Steel Research*, 59:47 – 61, 2003.
- B. Rossi, S. Afshan, and L. Gardner. Strength enhancements in cold-formed structural sections - part ii: Predictive models. *Journal of Constructional Steel Research*, 83(0):189 – 196, 2013. ISSN 0143-974X.
- N. Tondini, B. Rossi, and J.M. Franssen. Experimental investigation on ferritic stainless steel columns in fire. 2013.
- B. Uppfeldt, T. Ala Outinen, and M. Veljkovic. A design model for stainless steel box columns in fire. *Journal of Constructional Steel Research*, 64(11):1294 – 1301, 2008. ISSN 0143-974X. doi: 10.1016/j.jcsr.2008.05.003. International Stainless Steel Experts Seminar.